



TECHNISCHE  
UNIVERSITÄT  
WIEN  
Vienna University of Technology

# Generating correlations between photons via interaction with nanofiber-trapped atoms

DISSERTATION

zur Erlangung des akademischen Grades

**Doktor der Naturwissenschaften**

eingereicht von

**Adarsh Shankar Prasad**

Matrikelnummer 01429378

Simon-Denk-Gasse 2/21, 1090 Wien

an der  
Fakultät für Physik der Technischen Universität Wien

Betreuung: Prof. Dr. Arno Rauschenbeutel, E141 – Atominstitut

Diese Dissertation haben begutachtet:

---

(Prof. Dr. Arno  
Rauschenbeutel)

---

(Prof. Dr. Helmut Ritsch)

---

(Prof. Dr. Sebastian  
Hofferberth)

Wien, 13.08.2020

---

(Adarsh Shankar Prasad)



Die approbierte gedruckte Originalversion dieser Dissertation ist an der TU Wien Bibliothek verfügbar.  
The approved original version of this doctoral thesis is available in print at TU Wien Bibliothek.



TECHNISCHE  
UNIVERSITÄT  
WIEN  
Vienna University of Technology

# Generating correlations between photons via interaction with nanofiber-trapped atoms

DISSERTATION

submitted in partial fulfillment of the requirements for the degree of

**Doktor der Naturwissenschaften**

by

**Adarsh Shankar Prasad**

Registration Number 01429378

Simon-Denk-Gasse 2/21, 1090 Wien

to the Faculty of Physics  
at the Vienna University of Technology

Advisor: Prof. Dr. Arno Rauschenbeutel, E141 – Atominstitut

The dissertation has been reviewed by:

---

(Prof. Dr. Arno  
Rauschenbeutel)

---

(Prof. Dr. Helmut Ritsch)

---

(Prof. Dr. Sebastian  
Hofferberth)

Wien, 13.08.2020

---

(Adarsh Shankar Prasad)



Die approbierte gedruckte Originalversion dieser Dissertation ist an der TU Wien Bibliothek verfügbar.  
The approved original version of this doctoral thesis is available in print at TU Wien Bibliothek.

# Abstract

Generating correlated photons is an outstanding challenge of modern quantum optics owing to the inherently non-interacting nature of photons. Mediating interactions between uncorrelated photons to generate complex many-body states of photons has therefore been long sought for. Typically, such interactions require a high nonlinearity realized by quantum emitters strongly coupled to an optical mode. However, such approaches are often significantly impaired by unavoidable dissipation in the form of photon loss, which leads to a reduction of the correlations.

In this thesis, I will demonstrate an experimental approach where we use a strongly dissipative medium weakly coupled to a light field to generate strongly correlated states of light. Key to our system is a subwavelength diameter optical nanofiber, around which we trap neutral Cesium atoms in two linear arrays using a two-color optical dipole trap. The mutually non-interacting trapped atoms couple weakly to the guided mode of the nanofiber. Each atom can scatter a small fraction of the light out of the fiber which is the dissipative part of the atom-light interaction, thereby, reducing the number of uncorrelated photons. However, the fact that an atom can only absorb one photon at a time, generates correlations between photons that arrive at the atom at the same time. The scattered photons are spectrally detuned and, therefore, less absorbed. The large number of atoms in the system collectively enhances the dissipative and nonlinear effects, leading to highly correlated photons at the output of the nanofiber.

In the experiment, we launch a weak resonant light field through the nanofiber where it interacts with an ensemble of weakly-coupled atoms. We measure the second-order correlations induced in the transmitted light field via a Hanbury-Brown-Twiss setup. We observe that by changing the number of atoms in the ensemble, we are able to tune the interaction between the photons from non-interacting to repulsive to attractive, which we observe as a transition from no bunching to antibunching to bunching, respectively. This realization of a collectively enhanced nonlinearity opens new avenues for generating nonclassical states of light.



Die approbierte gedruckte Originalversion dieser Dissertation ist an der TU Wien Bibliothek verfügbar.  
The approved original version of this doctoral thesis is available in print at TU Wien Bibliothek.

# Kurzfassung

Die Erzeugung korrelierter Photonen ist eine besondere Herausforderung der modernen Quantenoptik, da Photonen intrinsisch nicht miteinander wechselwirken. Die Wechselwirkungen zwischen unkorrelierten Photonen, verbunden mit dem Ziel komplexe Vielteilchenzustände von Photonen zu erzeugen, wird daher seit Langem angestrebt. Typischerweise erfordern solche Wechselwirkungen eine hohe Nichtlinearität, die durch stark an eine optische Mode gekoppelte Quantenemitter realisiert werden kann. Solche Ansätze werden jedoch oft durch unvermeidliche Dissipation in Form von Photonenverlust erheblich beeinträchtigt, was zu einer Reduktion der Korrelationen führt.

In dieser Arbeit demonstriere ich einen experimentellen Ansatz, bei dem wir ein stark dissipatives Medium verwenden, welches schwach an ein Lichtfeld gekoppelt ist, um stark korrelierte Lichtzustände zu erzeugen. Das Herz unseres Systems ist eine optische Nanofaser, deren Durchmesser kleiner ist als die Lichtwellenlänge. An dieser Nanofaser fangen wir neutrale Cäsiumatome in zwei 1-dimensionalen Gittern, die durch eine optische Zweifarben-Dipolfalle erzeugt werden. Die nicht miteinander wechselwirkenden gefangenen Atome koppeln schwach an die in der Nanofaser geführte Mode. Jedes Atom kann einen kleinen Bruchteil des Lichts aus der Faser heraus streuen, was den dissipativen Teil der Atom-Licht-Wechselwirkung darstellt. Dadurch wird die Anzahl unkorrelierter Photonen reduziert. Die Tatsache, dass ein Atom immer nur ein Photon zur gleichen Zeit absorbieren kann, erzeugt jedoch Korrelationen zwischen Photonen, die zur gleichen Zeit am Atom ankommen. Die gestreuten Photonen sind spektral verstimmt und werden daher weniger absorbiert. Die große Anzahl von Atomen im System verstärkt die dissipativen und nichtlinearen Effekte, was zu stark korrelierten Photonen am Ausgang der Nanofaser führt.

Wir messen die im transmittierten Lichtfeld induzierten Korrelationen zweiter Ordnung mit Hilfe eines Hanbury-Brown-Twiss-Aufbaus. Dafür senden wir ein schwaches resonantes Lichtfeld durch die Nanofaser, wo es mit einem Ensemble schwach-gekoppelter Atome wechselwirkt. Wir beobachten, dass wir durch Änderung der Anzahl der Atome im Ensemble die Wechselwirkung zwischen den Photonen von "nicht-wechselwirkend" über "abstoßend" bis "attraktiv" einstellen können, was sich in den Messdaten durch den Übergang von "no bunching" zu "antibunching" zu "bunching" äußert. Diese Realisierung einer kollektiv erhöhten Nichtlinearität eröffnet neue Wege zur Erzeugung nicht-klassischer Lichtzustände.



Die approbierte gedruckte Originalversion dieser Dissertation ist an der TU Wien Bibliothek verfügbar.  
The approved original version of this doctoral thesis is available in print at TU Wien Bibliothek.



# List of Publications

In the process of working on this thesis, the following articles have been published in peer-reviewed journals or will be published soon:

- Adarsh S. Prasad, J. Hinney, Sahand Mahmoodian, Klemens Hammerer, Samuel Rind, Philipp Schneeweiss, Anders S. Sørensen, Jürgen Volz, and Arno Rauschenbeutel.  
*Correlating photons using the collective nonlinear response of atoms weakly coupled to an optical mode*, Nat. Photonics, (2020).
- J. Hinney, Adarsh S. Prasad, S. Mahmoodian, K. Hammerer, A. Rauschenbeutel, P. Schneeweiss, J. Volz, M. Schemmer  
*Unraveling two-photon entanglement via the squeezing spectrum of light traveling through nanofiber-coupled atoms*, arXiv:2010.09450, (2020).
- Cooling torsional oscillation mode of a nanofiber.  
(in preparation)



Die approbierte gedruckte Originalversion dieser Dissertation ist an der TU Wien Bibliothek verfügbar.  
The approved original version of this doctoral thesis is available in print at TU Wien Bibliothek.

# Contents

<b>1</b>	<b>Introduction</b>	<b>1</b>
<b>2</b>	<b>Trapping atoms around optical nanofibers</b>	<b>5</b>
2.1	Introduction . . . . .	5
2.2	Light propagation through nanofibers . . . . .	6
2.2.1	Nanofibers . . . . .	6
2.2.2	Guided modes of a Nanofiber . . . . .	6
2.2.3	Polarization of light fields . . . . .	10
2.3	Introduction to Cesium atom . . . . .	11
2.4	Light shifts . . . . .	12
2.5	Properties of our nanofiber based trap for neutral Cs atoms . . . . .	14
2.5.1	Radial confinement . . . . .	15
2.5.2	Axial confinement . . . . .	16
2.5.3	Azimuthal confinement . . . . .	16
2.5.4	Magic wavelengths: Vanishing differential scalar light shift . . . . .	17
2.5.5	Vanishing vector light shift . . . . .	18
2.5.6	Nonvanishing tensor light shifts . . . . .	19
2.5.7	Light shift from detuned probe laser . . . . .	19
<b>3</b>	<b>Implementation of Nanofiber-based light-matter interface</b>	<b>23</b>
3.1	Introduction . . . . .	23
3.2	Experimental setup . . . . .	24
3.2.1	Ultra high vacuum setup . . . . .	24
3.2.1.1	Chamber design . . . . .	24
3.2.1.2	Caesium source . . . . .	26
3.2.2	Nanofiber integration into the setup . . . . .	26
3.2.2.1	Nanofiber transmission measurement . . . . .	27
3.2.2.2	Coupling optics for input into nanofiber . . . . .	29
3.2.2.3	Polarization variation along long nanofiber waist . . . . .	30
3.2.2.4	Detection optics after nanofiber output . . . . .	32
3.2.3	Magneto-optical trap . . . . .	34
3.2.3.1	Magnetic coil design . . . . .	34
3.2.3.2	Optics for laser cooling . . . . .	36

3.2.3.3	Alignment of optical fields . . . . .	37
3.2.3.4	Absorption imaging . . . . .	37
3.2.3.5	B field calibration: Microwave spectroscopy . . . . .	40
3.2.4	Experiment control and data acquisition . . . . .	42
3.3	Trapping atoms . . . . .	44
3.3.1	Experimental sequence for trapping atoms . . . . .	44
3.3.2	Measurement of optical depth . . . . .	45
3.3.3	Estimation of the number of atoms . . . . .	47
3.3.4	Optimum trapping configuration . . . . .	48
3.3.5	Measuring filling factor . . . . .	49
3.3.6	Lifetime of trapped atoms . . . . .	50
<b>4</b>	<b>Theory: Correlated Photon transport in nanofibers</b>	<b>53</b>
4.1	Introduction . . . . .	53
4.2	Correlation functions . . . . .	54
4.2.1	First-order correlation function . . . . .	54
4.2.2	Second-order correlation function . . . . .	55
4.2.2.1	Classical light . . . . .	56
4.2.2.2	Single mode light field as non-classical light . . . . .	56
4.2.2.3	Antibunched and bunched light . . . . .	57
4.2.2.4	Measuring second-order intensity correlations . . . . .	58
4.3	Photon transport across coupled emitters . . . . .	60
4.3.1	One-photon scattering across a waveguide coupled to a single emitter . . . . .	60
4.3.2	Optical depth due to a single waveguide-coupled atom . . . . .	64
4.3.3	Two-photons scattering across single emitter: Scattering matrix formalism . . . . .	64
4.3.4	Scattering matrix with multiple emitters . . . . .	66
4.3.5	Total transmission . . . . .	67
4.3.6	Two-photon output in transmitted light . . . . .	69
4.3.7	Photon statistics in the output . . . . .	70
4.3.8	Quantitative prediction . . . . .	72
<b>5</b>	<b>Observation of correlated photon transport in nanofibers</b>	<b>75</b>
5.1	Experimental Methods . . . . .	75
5.1.1	Setup . . . . .	75
5.1.1.1	Detection . . . . .	75
5.1.2	Experimental Sequence . . . . .	77
5.1.2.1	Ensemble preparation . . . . .	78
5.1.2.2	Interleaved probing: . . . . .	78
5.1.2.3	After the interleaved probing . . . . .	81
5.1.3	Estimation of coupling strength ( $\beta$ ) . . . . .	82
5.2	Data processing . . . . .	84
5.2.1	Sorting runs based on OD from transmission . . . . .	84
5.2.2	Obtaining normalized second order correlations . . . . .	86
5.2.2.1	Obtaining the coincidence histogram, ( $C(\tau)$ ) . . . . .	86

5.2.2.2	Normalization . . . . .	87
5.2.3	Estimating $g^{(2)}(0)$ from coincidence histograms . . . . .	88
5.2.4	Theoretical prediction of $(g^{(2)}(0)$ vs OD) . . . . .	91
5.3	Results and Interpretation . . . . .	91
5.4	Conclusion and Outlook . . . . .	93
<b>6</b>	<b>Outlook and conclusion</b>	<b>97</b>
6.1	Summary . . . . .	97
6.2	Outlook . . . . .	98
	<b>Appendices</b>	<b>101</b>
<b>A</b>	<b>Bragg Scattering</b>	<b>103</b>
A.1	Simulation . . . . .	104
A.1.1	Analytical calculation of intensity distribution . . . . .	104
A.1.2	Array of dipole emitters . . . . .	105
A.1.3	Incorporating imperfections . . . . .	106
A.1.3.1	Non-uniformities in the fiber . . . . .	106
A.1.3.2	Rotation of trapping plane . . . . .	109
A.1.3.3	Position distribution of the atoms about the trapping minima . . . . .	109
A.1.3.4	Filling factor . . . . .	109
A.1.3.5	Uncertainty of loading . . . . .	109
A.1.3.6	Scattering losses from trapped atoms . . . . .	110
A.1.4	Realistic intensity distribution of the cone . . . . .	110
A.2	Detection . . . . .	112
A.3	Outlook . . . . .	113
<b>B</b>	<b>Supplementary information</b>	<b>115</b>
B.1	Correlations for all atom numbers . . . . .	115
	<b>Bibliography</b>	<b>121</b>



Die approbierte gedruckte Originalversion dieser Dissertation ist an der TU Wien Bibliothek verfügbar.  
The approved original version of this doctoral thesis is available in print at TU Wien Bibliothek.

# Introduction

the investigation of light-matter interaction has been crucial to the development of modern quantum optics. The conceptualization of photons as elementary particles of light was crucial in understanding the absorption and emission of radiation by matter. Planck and Einstein highlighted the discrete nature of light energy through their work on the derivation of the blackbody spectrum [1] and explanation of the photoelectric effect [2, 3] respectively. However, phenomena such as interference, diffraction or scattering of light still could not be explained without considering Maxwell's electromagnetic waves formulation of light [4]. In the following years, seminal works such as Neils Bohr's quantization of electronic energy levels of the Hydrogen atom [5], Louis De Broglie's wave-particle duality hypothesis combining wave and particle nature of matter [6], Heisenberg's uncertainty principle [7], and Schrödinger's equation [8] laid the framework of quantum physics which allowed one to explain phenomena which otherwise could not be physically understood. Following this, came one of the most important studies of quantum optics on light-matter interaction, where Paul Dirac in a series of papers, used semiclassical and fully quantum mechanical models [9, 10] to explain emission and absorption of radiation by atoms, and the spectrum of Hydrogen atoms. Due to a lack of a monochromatic light source, it was not until the second half of the 20<sup>th</sup> century that one could start doing experiments where a fully quantized approach to light-matter interaction was necessary.

The invention of the laser [11, 12] allowed probing matter with almost monochromatic radiation and with very well defined photon statistics [13]. Moreover, by letting the laser light interact with the matter, one could now produce exotic states of light such as a single photon wavepackets [14], entangled photon pairs [15, 16] and squeezed states of light [17]. This generated a lot of interest in investigating applications of such interactions in quantum information processing [18–21], precision measurements [22, 23], and quantum communication [24]. Therefore, the realization of an efficient interaction between light and matter via the development of novel light-matter interfaces [20, 25, 26] has become one of the major themes of the ongoing second quantum revolution [27].

The usefulness of a light-matter interface for photonic quantum technologies depends on efficient coupling of photons - the fundamental carriers of quantum information - with the quantum emitters. Usually the coupling strength depends on the product of the local electric field associated with the photon and the atomic dipole. Therefore, higher interaction strengths usually require a higher electric field. The most common approach to increase the coupling strength is to focus the light. However, the focussing is fundamentally limited by the diffraction limit [4]. Therefore, since the early days of quantum optical research, such an enhancement of electric field has been achieved by cavities leading to the field of cavity quantum electrodynamics (CQED) [28]. The increased coupling results from the enhancement of the light intensity at the position of the quantum emitter located inside the cavity. However, the experimental complexity, technical challenges, and bandwidth constraints associated with CQED experiments calls for other alternative approaches. Another way for enhancing the coupling is to use large ensembles of atoms. In such an approach, the collective superposition state of the atomic ensemble enhances the coupling strength by  $\sqrt{N}$ , where  $N$  is the number of atoms [29, 30]. However, the coupling strength still depends on the local field strength at the position of the atoms in the atomic ensemble, which is limited by the diffraction limited focusing of light. In addition, it is not trivial to achieve high optical depths for a light beam passing through such a cold atomic ensemble, which is usually a key parameter for a light-matter interface to be useful. However, with recent advances in technologies, optical waveguide-based light-matter interfaces have gained a lot of attention as a possible solution. In particular, optical nanofibers have established themselves as an efficient light-matter interface [31–34].

In an optical nanofiber based-light-matter interface, which is the key component of the research presented in this thesis, the high-coupling strength comes in two forms. First, due to the sub-wavelength confinement of light in the nanofiber waist [35] one can achieve high intensities over a larger distance which is usually not possible in a tightly focused light beam. Plus most of the light energy is present in the evanescent region of the optical nanofiber, where it can be easily interfaced with atoms in the vicinity of the nanofiber surface [35, 36]. The small extent of the transverse mode leads to greater overlap with the atomic absorption cross-section, thereby allowing for high atom-light coupling strength. The second enhancement comes due to the large number of atoms that can be trapped around a nanofiber with each trapped atom having a comparably high single atom-light coupling strength [37]. With the state-of-art developments [33, 34], that include large ground state coherence times [38], efficient cooling mechanisms resulting in longer trap lifetimes [39], and proposals that allow collective enhancement to exponentially increase the fidelity of information storage [40], nanofibers have established themselves as a versatile and robust light-matter interface. In addition, they allow for unique features such as spin-orbit coupling [41–43], multimode-strong coupling [44], Bragg reflection [45, 46] and sub- and super-radiance effects [40, 47], which make the nanofiber-based light-matter interface an attractive system for studying complex many-body physics of light-matter interaction, as well as, for demonstration of novel physics which is not just limited to optical domain, but can be extended also to other frequency regimes such as microwave.

One such exciting application of nanofiber-based atom-light interfaces is to mediate interactions between photons which by themselves are inherently non-interacting. The key to this are the nanofiber-coupled atoms. Because of the quantized nature of atomic energy levels, an



---

atom can absorb only a single photon at a given time [48]. This is the strongest nonlinearity possible where absorption of one photon modifies the reaction of the medium with respect to the next photon. Therefore, if one sends a stream of photons spaced randomly in time, the atom modifies the temporal statistics of photons at the output. Nanofibers facilitate the interaction of the photons with a large number of atoms, thereby enhancing the effects of light-matter interaction despite the moderate single atom-photon coupling strength [45]. There have been lots of proposals which predict exciting many-body physics with waveguide interfaced quantum emitters [49–51]. In this thesis, I will present the result of our experimental study on a complex many body interaction phenomenon between photons from a weak resonant light field and an ensemble of atoms trapped around an optical nanofiber based on the proposal from the reference [51]. We observe that by changing the number of atoms interfaced with the light field propagating inside the nanofiber, we are able to tune the effective interaction between the photons from none to repulsive to attractive, as a result of which, the probability of observing two-photons simultaneously at the output also changes. We observe antibunching for low atom numbers which provides clear evidence for the generation of non-classical light. In addition, for large atom numbers we observe a change from antibunching to bunching which means that the photons tend to come out of the nanofiber in bunches rather than separately. Larger number of atoms means higher dissipation which stems from the fact that more atoms can scatter more light out of the nanofiber which could potentially hamper the correlations. In our case, the interplay of nonlinearity and dissipation by the atoms allows for the tuning of the two-photon probability amplitude leading to the observed effect. Such an effect as demonstrated here, can be used for the generation of antibunched stream of photons with high flux. The results shown in this thesis pave a way for performing complex many body physics using atomic ensembles and light [51, 52].

The thesis is organized as follows. In chapter 2, I explain the physics of light propagation in nanofibers and how it can be used to trap neutral Caesium atoms. Following it, in chapter 3, I explain how I implemented a second generation of a nanofiber trap setup in my group. I explain the various tools and techniques that are used for designing, characterizing, and performing measurements in my setup. Next, I introduce in Chapter 4 some basic definitions from quantum optics which are required to understand the results from the demonstrated experiment. In particular, I also discuss some basic physics of photon scattering from coupled emitters and summarize the results from the theory proposal behind our experiment. Chapter 5 provides detailed explanations of the experimental setup, and outlines methods, and results from the performed experiment. Chapter 6 summarizes the work presented in this thesis and outlines the future directions of research.



Die approbierte gedruckte Originalversion dieser Dissertation ist an der TU Wien Bibliothek verfügbar.  
The approved original version of this doctoral thesis is available in print at TU Wien Bibliothek.

# Trapping atoms around optical nanofibers

## 2.1 Introduction

Optical fibers are cylindrical silica structures that are capable of guiding light over large distances with minimal losses. A typical cylindrical optical fiber consists of a central core with refractive index  $n_1$  surrounded by a cladding with a slightly lower refractive  $n_2$ . The acceptance angle at which the light enters into the fiber is given by the numerical aperture of the fiber  $NA = \sin^{-1}[1 - n_2^2/n_1^2]$ . This constrains the angle of incidence at the core-cladding interface to be greater than the critical angle ( $\theta_c = \sin^{-1}[n_2/n_1]$ ). Then the light is guided by total-internal reflection without any loss. When the refractive index difference is much less than the refractive index of the core, light is said to be weakly guided. The exact solution to the electromagnetic wave equation for light propagation inside an optical fiber yields the guided mode functions which give the spatiotemporal distribution of the associated electric and magnetic fields. Solving Maxwell's equations for the guided modes has been thoroughly studied in the past [53, 54].

In contrast to the optical fibers with diameter larger than the wavelength of the propagating light field, tapered optical fibers are structurally modified optical fibers that contain sections with a diameter less than the wavelength of the propagating light field. This allows confinement of light to sub-wavelength dimensions enabling a strong transverse confinement of the light field. Due to this, nanofibers offer large coupling over large distance because of the non-diverging guided mode. In this chapter, I will introduce the physics of light propagation inside such optical nanofibers. Then, I will introduce Caesium as the neutral atom species with which we interface the nanofiber guided light. I will then summarize analytical expressions related to creating the optical dipole trap potential in the evanescent field of the nanofiber to trap neutral Cs atoms. Following it, I will explain our choice of the far-off resonance light fields for creating the dipole trap. In the end, we shall look quantitatively at some of the important properties of our nanofiber-based trap.

## 2.2 Light propagation through nanofibers

### 2.2.1 Nanofibers

The term *nanofibers* used throughout this thesis refers to a cylindrical section of a glass optical fiber which is a few hundred nanometers in diameter and capable of guiding light fields such that a large part of the field energy lies in the evanescent component of the field. It is derived from a normal step index glass optical fiber in an optimized heat and pull process [55]. To start with, a section of the fiber with only the core and cladding layers is cleaned. The cleaned section is then heated uniformly in a clean hydrogen-oxygen flame and the two ends of the section simultaneously pulled. As a result, the optical fiber section in the centre becomes thin, with two tapered sections on the side connecting it to the unstretched part of the fiber as shown schematically in 2.1. The central section called the *nanofiber waist* has a vanishing core. The light is guided in the nanofiber waist by means of total internal reflection from the cladding-air junction. Due to a large difference of refractive index of silica and the surrounding air/vacuum, the light is said to be strongly guided. Depending on the radius of the fiber and wavelength of the propagating field, the extent of the evanescent field outside the fiber can be a several times the radius of the fiber. The properties of such guided modes have been studied in detail [32, 35]. I will introduce some of the key properties in the next section.

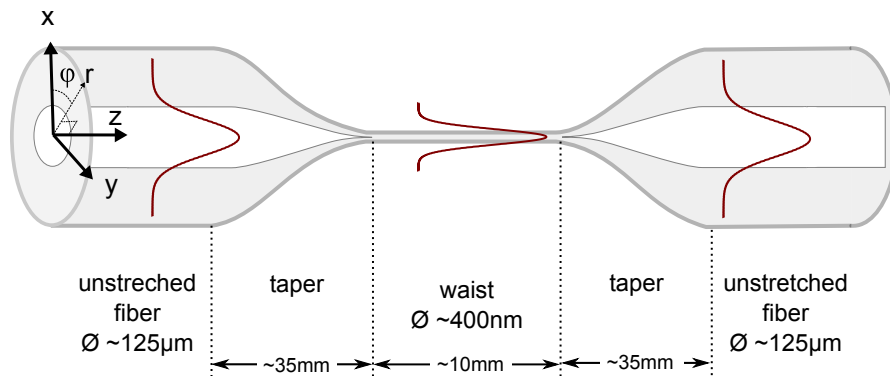


Figure 2.1: Sketch of a typical tapered optical fiber. The dimensions of the taper and the nanofiber waist correspond to what we used in our experiment. The brown color represents the extent of the field. In the waist region the field is extended outside the fiber which enables the propagating light field to couple to an atom in the vicinity of the nanofiber waist.

### 2.2.2 Guided modes of a Nanofiber

Light propagation in the nanofiber waist cannot be described by a transverse electric mode as is usually the case for weakly guided single mode fibers. This is because the tight confinement of the light field guided by the nanofiber waist leads to a strong longitudinal component of the

electric field<sup>1</sup>. The guided modes in a optical nanofiber are described by the fundamental Hybrid electric ( $HE_{11}$ ) mode. The light fields in this mode show non-vanishing longitudinal component inside the nanofiber waist. In this context, depending upon the transverse polarization, the light is said to be quasilinear or quasicircularly polarized if the transverse polarization is linear or circular. The propagation constant  $\beta$  for an optical field (frequency  $\omega$ , free-space wavelength  $\lambda$ ) in a nanofiber with waist refractive index  $n_1$ , radius  $a$  surrounded by a medium air/vacuum with refractive index  $n_2 = 1$  is given by solving the eigenvalue equation [53]:

$$\frac{J_0(ha)}{haJ_1(ha)} = -\frac{n_1^2 + n_2^2}{2n_1^2} \frac{K_1'(qa)}{qaK_1(qa)} + \frac{1}{h^2a^2} - \left[ \left( \frac{n_1^2 - n_2^2}{2n_1^2} \frac{K_1'(qa)}{qaK_1(qa)} \right)^2 + \frac{\beta^2}{n_1^2k^2} \left( \frac{1}{q^2a^2} + \frac{1}{h^2a^2} \right)^2 \right]^{1/2} \quad (2.1)$$

where  $h = (n_1^2k^2 - \beta^2)^{1/2}$  and  $q = (\beta^2 - n_2^2k^2)^{1/2}$  are constants that characterize the fields inside and outside the waist,  $J_n$  and  $K_n$  are Bessel function of the first kind and modified Bessel function of the second kind, respectively. Due to the cylindrical symmetry of nanofibers, one can express the components of the electric field conveniently in the cylindrical coordinates. In addition, it is most convenient to work with the normalized electric field mode functions with the normalization constant  $C$  which can be found by the normalization condition for the electric field defined later in equation 2.4. Keeping this in mind, for a counterclockwise quasicircularly polarized field propagating along  $+z$  direction, the normalized electric field mode functions for  $r < a$  can be written as [56]:

$$e_r = iC \frac{q}{h} \frac{K_1(qa)}{J_1(ha)} [(1-s)J_0(hr) - (1+s)J_2(hr)], \quad (2.2a)$$

$$e_\phi = -C \frac{q}{h} \frac{K_1(qa)}{J_1(ha)} [(1-s)J_0(hr) + (1+s)J_2(hr)], \quad (2.2b)$$

$$e_z = C \frac{2q}{\beta} \frac{K_1(qa)}{J_1(ha)} J_1(hr) \quad (2.2c)$$

For  $r > a$ :

$$e_r = iC [(1-s)K_0(qr) + (1+s)K_2(qr)], \quad (2.2d)$$

$$e_\phi = -C [(1-s)K_0(qr) - (1+s)K_2(qr)], \quad (2.2e)$$

$$e_z = C \frac{2q}{\beta} K_1(qr) \quad (2.2f)$$

In the above two sets of equations, the  $s$  parameter is defined as

$$s = \frac{1/h^2a^2 + 1/q^2a^2}{J_1'(ha)/haJ_1(ha) + K_1'(qa)/qaK_1(qa)}, \quad (2.3)$$

<sup>1</sup>One can prove this by applying Gauss law,  $\oint \vec{E} \cdot d\vec{S} = \rho_{\text{free}}/\epsilon_0$ , in a coaxial cylindrical volume within the electrically neutral ( $\rho_{\text{free}} = 0$ ) nanofiber waist. This gives,  $E_r \propto -r\partial E_z/\partial z$ , which implies that if there is some radial component of the electric field, the longitudinal component must be non-vanishing.

and the parameter  $C$  is a normalization constant which one can obtain from normalizing the mode field functions as

$$\int_0^{2\pi} d\phi \int_0^\infty n_{\text{medium}}^2 |\mathbf{e}|^2 r dr = 1 \quad (2.4)$$

where  $n_{\text{medium}} = n_1$  for  $r < a$ , and  $n_{\text{medium}} = n_2$  for  $r > a$ . The expressions presented here and the notations used are borrowed from various relevant literature [56, 57] dealing with this topic. The mode index is represented by  $\mu = (\omega, f, l)$ , where  $\omega$  is the mode frequency,  $f = +/ -$  indicates forward ( $+\vec{z}$ ) or backward ( $-\vec{z}$ ) propagation direction and  $l = +1, -1$  indicates right or left circularly polarized light field. Following this notation, the exact expression for the electric field for a quasicircularly polarized light field can now be written as

$$\begin{aligned} \vec{E}_{\text{circ}}^\mu &= A \vec{e}^\mu e^{if\beta z + il\phi} \\ &= A(\hat{r}e_r + l\hat{\phi}e_\phi + f\hat{z}e_z)e^{if\beta z + il\phi} \end{aligned} \quad (2.5)$$

where,  $e_r, e_\phi, e_z$  are the normalized electric field mode functions given by equation 2.2, and  $A$  is the amplitude of the electric field and is determined by the power ( $P_z$ ) of the propagating field as

$$P_z = \frac{\epsilon_0 \nu_g}{2} \int n_{\text{medium}}^2(r) |\mathbf{E}(\mathbf{r})|^2 dr \quad (2.6)$$

where,  $\nu_g = (d\beta/d\omega)^{-1}$  is the group velocity of the guided light and  $n_{\text{medium}} = n_1$  for  $r < a$ , and  $n_{\text{medium}} = n_2$  for  $r > a$ . The unit vectors used:  $\hat{r}, \hat{\phi}$ , and  $\hat{z}$  can be converted to the Cartesian coordinate unit vectors:  $\hat{x}, \hat{y}$ , and  $\hat{z}$  as:

$$\hat{r} = \hat{x} \cos \phi + \hat{y} \sin \phi, \quad (2.7)$$

$$\hat{\phi} = -\hat{x} \sin \phi + \hat{y} \cos \phi, \quad (2.7)$$

$$\hat{z} = \hat{z} \quad (2.8)$$

The cartesian coordinates are especially useful in expressing the electric field vector for quasilinearly polarized light fields where the electric field may be polarized in the transverse plane of the fiber at an angle  $\phi_0$ . Therefore, such a quasilinearly polarized mode is characterized by three main parameters  $(\omega, f, \phi_0)$ , which represent the frequency, propagation direction and the transverse polarization. Such a light field can be expressed as a superposition of two opposite quasi-circularly polarized guided modes as:

$$\vec{E}_{\text{lin}}^{(\omega f \phi_0)} = \frac{1}{\sqrt{2}} \left( \vec{E}_{\text{circ}}^{(\omega f +)} e^{-i\phi_0} + \vec{E}_{\text{circ}}^{(\omega f -)} e^{i\phi_0} \right) \quad (2.9)$$

Using equations 2.5 and 2.9, one can express the electric field for a quasi-linearly polarized mode in the cylindrical coordinates as:

$$\vec{E}_{\text{lin}}^{(\omega f \phi_0)} = \sqrt{2} A [\hat{r}e_r \cos(\phi - \phi_0) + \hat{\phi}e_\phi \sin(\phi - \phi_0) + f\hat{z}e_z \cos(\phi - \phi_0)] e^{if\beta z} \quad (2.10)$$

Using equation 2.7, one can then transform equation 2.10 to obtain the expression of the electric field in Cartesian coordinates. One can find plots of the electric field distribution in detail in reference [35] for a quasilinear and quasicircular polarized guided mode in an optical nanofiber.

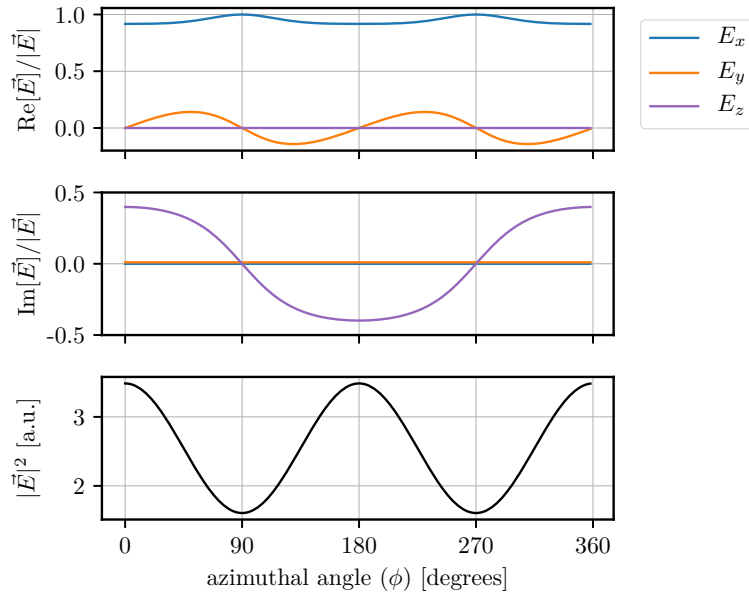


Figure 2.2: (a) Azimuthal electric field distribution for a quasilinearly polarized field (main polarization along  $x$ ) around a nanofiber at position  $r \approx 450$  nm in the  $z = 0$  plane. The top, centre and bottom plot shows the real, imaginary and total azimuthal intensity distribution. The fiber radius is 200 nm. The longitudinal component (here along  $z$ ) of the field is out of phase with the transverse ( $x$  and  $y$ ) components. In particular, at  $\phi = 0(\pi)$ , the longitudinal component,  $E_z$ , is  $\pi/2(-\pi/2)$  phase shifted from the transverse field component which is constituted only by  $E_x$ . Therefore, the light is circularly polarized,  $\sigma^+(\sigma^-)$ , with  $y$  as the quantization axis (see section 2.2.3 for more details).

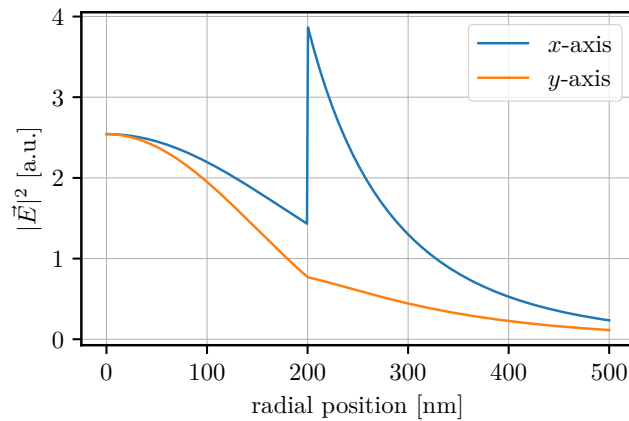


Figure 2.3: Radial distribution of intensity for a quasilinear light field (main polarization oriented along  $x$ ) as seen along the  $x$ -axis (blue) and along the  $y$ -axis (orange). The fiber radius is 200 nm

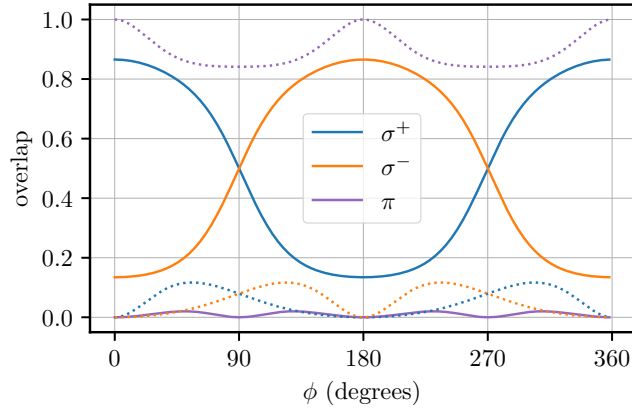


Figure 2.4: Polarization overlap of the electric field ( $\vec{E}$ ) of a quasilinearly polarized field with  $\{\sigma^\pm, \pi\}$  polarizations as a function of the azimuthal angle. The solid or dashed lines correspond quasilinearly polarized along  $x$  or  $y$  axis respectively. The overlap is given as  $\xi = |\hat{E} \cdot \hat{e}|^2$ . The radial distance is fixed at  $\sim 450$  nm in the  $z = 0$  plane, and the quantization axis is along  $y$ .

### 2.2.3 Polarization of light fields

To get a intuitive understanding of the polarization distribution, I compute the real and imaginary part of the electric field unit vector for a quasilinearly polarized mode (main polarization along  $x$ -axis) for parameters: radial position  $r = 450$  nm, fiber radius  $a = 200$  nm. This is plotted in Figure 2.2 as a function of the azimuthal angle  $\phi$ . From the top and centre panel one can see that the transverse component is real whereas the longitudinal component ( $E_z$ ) is imaginary i.e.,  $90^\circ$  phase shifted to the transverse, with positive shift for  $\phi \in \{-\pi/2, \pi/2\}$  and negatively shifted for  $\phi \in \{\pi/2, 3\pi/2\}$ . Such a phase shift between transverse and longitudinal electric field component gives rise to a rotating polarization of the local electric field. It turns out that the rotation sense of the elliptical polarization depends on the direction of propagation of the light field and the azimuthal position, which allows for non-reciprocal coupling of a quantum emitter with the fiber-guided mode [41–43, 58].

To see how the circularity of local polarization changes around the nanofiber surface, I calculate the overlap of the normalized field outside the fiber ( $\hat{E}$ ) with the polarization basis vector ( $\hat{e}$ ) according to Ref. [43], as  $\xi_{\hat{e}} = |\hat{E} \cdot \hat{e}|^2$  where  $\hat{e} \in \{\sigma^\pm = \pm(\hat{x} \mp i\hat{z})/\sqrt{2}, \pi = \hat{y}\}$ . I compute this as a function of the azimuthal position assuming a radial distance ( $r = 450$  nm) and assuming  $y$ -axis as the quantization axis. The solid and dashed lines in Figure 2.4 show the corresponding polarization overlap for a quasilinearly polarized field with main polarization along  $x$ - and ( $y$ -)axis respectively. For the  $x$ -polarized field, we see that for  $\phi = \{0, \pm\pi\}$ , the overlap with circular polarization  $\{\sigma^+, \sigma^-\}$  is more than 80%. In contrast, for a  $y$ -polarized field the field is almost always  $\pi$  polarized with the overlap going to 100% on the  $x$ -axis. In our experiments, we use quasilinear fields. The consequence of the polarization is explained with relevance to trapping (vector light shifts) in section 2.5.5.



## 2.3 Introduction to Cesium atom

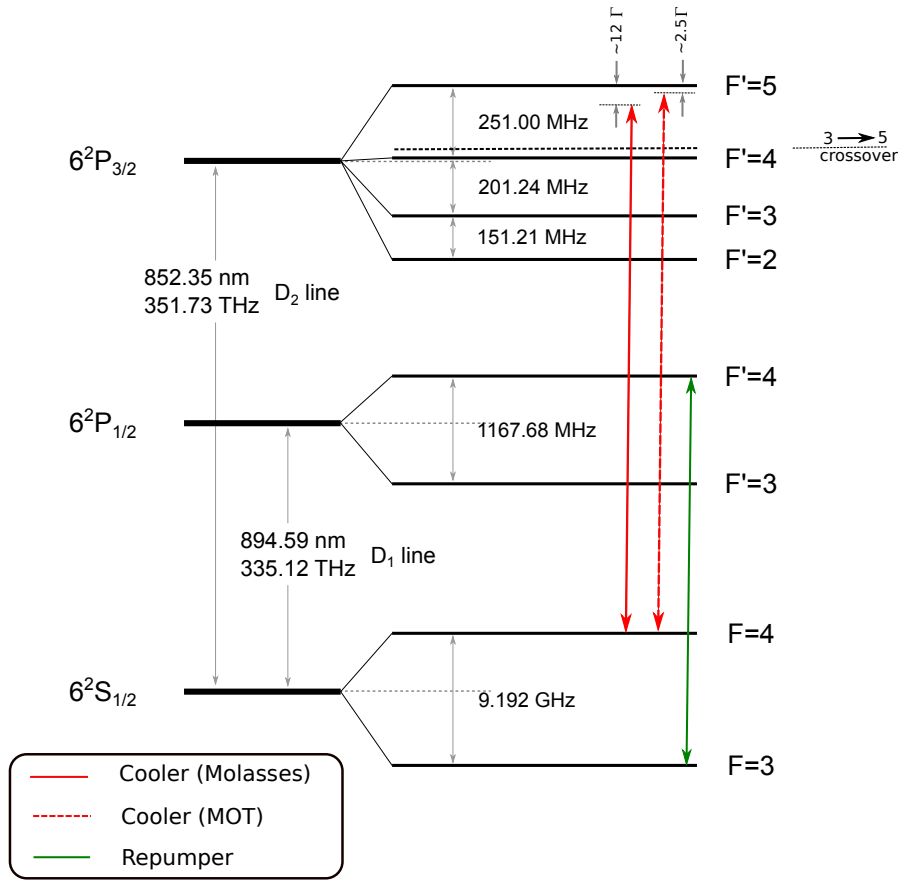


Figure 2.5: The optical transitions of the Cs atom used in our experiment. The cooler laser is locked to the crossover peak of  $F' = 3$  and  $F' = 5$  in the  $6P_{3/2}$  hyperfine manifold, whereas the repumper is locked to transition indicated by the green line.

We trap neutral Caesium atoms around the nanofiber. The outer electron in of Cs has principle quantum number,  $n = 6$ . The sublevels  $\{6S, 6P, 6D, \dots\}$  represented by the orbital angular momentum quantum number  $L = \{0, 1, 2, \dots, n - 1\}$  have different energies depending on the  $n$  and  $L$  values. Depending upon the electron orbital angular momentum ( $\mathbf{L}$ ) and spin angular momentum  $\mathbf{S}$ , the total electron angular momentum  $\mathbf{J}$  further splits the electronic sublevels according to  $|L - S| \leq J \leq |L + S|$ , where  $S = 1/2$  represents the spin angular momentum of the electron. This gives us the fine structure of Cs. We are mostly interested in the ground state ( $6^2S_{1/2}$ ) and excited states ( $6^2P_{1/2}, 6^2P_{3/2}$ ) of Cs where the states have been written in the form  $n^2J+1L_J$ . The level-scheme is shown in Figure 2.5. The spectral lines corresponding to the transition  $6^2S_{1/2} \rightarrow 6^2P_{1/2}$  are called the D1-line (roughly around 894 nm), and  $6^2S_{1/2} \rightarrow 6^2P_{3/2}$  are called D2-line (roughly around 852 nm). Cs has a total nuclear angular momentum (represented by quantum number  $\mathbf{I}$ ) of  $7/2$  which interacts with the total electron angular momentum

resulting in further splitting of the atomic energies in the form of hyperfine structure. The total atomic angular momentum is represented by the operator  $\mathbf{F}$ . The hyperfine levels are referred to by the quantum number  $F$  where  $|J - I| \leq F \leq |J + I|$ . The ground state  $6^2S_{1/2}$  thus splits into hyperfine levels corresponding to  $F = \{3, 4\}$ . The excited state  $6^2P_{1/2}$  also splits into two corresponding to  $F' = \{3, 4\}$  whereas the other excited state  $6^2P_{3/2}$  splits into four hyperfine levels  $F' = \{2, 3, 4, 5\}$ . The corresponding ground to excited state transitions are allowed according to selection rules are  $\Delta F = 0, \pm 1$ . In the presence of an external magnetic field (Zeeman interaction), each hyperfine level denoted by  $F$  can be further split into  $2F + 1$  levels represented by the magnetic quantum number  $M$  with integral values  $m_F$  such that  $-F \leq m_F \leq F$ . The selection rules modifies now to  $\Delta F = \{0, \pm 1\}$ ,  $\Delta m_F = \{0, \pm 1\}$  except  $\Delta m_F = 0$ , if  $F = F'$  which is forbidden. The optical transitions of Cs that we use are shown in Figure 2.5. Almost all other relevant information about Cs useful for quantum optics community can be found in References [59, 60].

## 2.4 Light shifts

Having discussed Cs atoms and the important quantum numbers, we can now investigate the effect of subjecting a Cs atom to an electromagnetic field. In this section, I will summarize some important results for calculating the optically-induced state-dependent light shift for an atom when placed in a far off-resonance light field. Starting with an electric field which can be written as

$$\mathbf{E} = \frac{\mathcal{E}\mathbf{u}e^{i\omega t}}{2} + c.c. \quad (2.11)$$

where  $\mathcal{E}$  is the complex-valued electric field amplitude and  $\mathbf{u}$  is the polarization vector<sup>2</sup> One can express the electric fields from equation 2.10 or 2.5 in the above form. The light field induced Stark shift of the energy of the state is the time-averaged expectation value of the interaction operator given as

$$U_{\text{opt}} = -\langle \mathbf{d} \cdot \mathbf{E} \rangle \quad (2.12)$$

The induced dipole is dependent on the electric field inducing it through a factor called the polarizability [61] as

$$\langle \mathbf{d} \rangle = \alpha(\omega)\mathbf{E} \quad (2.13)$$

Substituting equation 2.13 into 2.12 one can obtain the Stark shift for an atomic state described by the quantum numbers  $|n, J, F, M\rangle$ <sup>3</sup> The energy shift in the presence of far off-resonance

<sup>2</sup>Here the vector  $\mathbf{u}$  is expressed in the form of the so called spherical tensor component. The transformation of a cartesian coordinate vector,  $\{v_x, v_y, v_z\}$ , to spherical tensor component goes as  $\{v_{-1}, v_0, v_1\} = \{(v_x - iv_y)/\sqrt{2}, v_z, -(v_x + iv_y)/\sqrt{2}\}$ , for  $y$  being the quantization axis.

<sup>3</sup>We use the assumption that splitting of Zeeman levels  $\ll$  hyperfine level splitting  $\ll$  fine-structure level splitting such that state intermixing does not happen and also that the light-induced shifts are small compared to hyperfine and fine splitting.

optical fields can be written as [62, 63]

$$\begin{aligned}
 U_{opt} &= -\frac{1}{4}|\mathcal{E}|^2 \left[ \alpha_{nJF}^s - i\alpha_{nJF}^v \frac{[\mathbf{u}^* \times \mathbf{u}] \cdot \mathbf{F}}{2F} \right. \\
 &\quad \left. + \alpha_{nJF}^T \frac{3[(\mathbf{u}^* \cdot \mathbf{F})(\mathbf{u} \cdot \mathbf{F}) + (\mathbf{u} \cdot \mathbf{F})(\mathbf{u}^* \cdot \mathbf{F})] - 2\mathbf{F}^2}{2F(2F-1)} \right] \\
 &= U_{\text{scalar}} + U_{\text{vector}} + U_{\text{tensor}}
 \end{aligned} \tag{2.14}$$

where the shift has been expressed as a sum of three different types of light shifts - scalar, vector and tensor with the corresponding polarizabilities denoted by superscript  $\{s, v, T\}$ . The scalar, vector and tensor polarizabilities are given by the following expressions [62] as

$$\alpha_{nJF}^s = \frac{1}{\sqrt{3(2J+1)}} \alpha_{nJ}^{(0)} \tag{2.15a}$$

$$\alpha_{nJF}^v = (-1)^{J+I+F} \sqrt{\frac{2F(2F+1)}{F+1}} \begin{Bmatrix} F & 1 & F \\ J & I & J \end{Bmatrix} \alpha_{nJ}^{(1)} \tag{2.15b}$$

$$\alpha_{nJF}^T = -(-1)^{J+I+F} \sqrt{\frac{2F(2F-1)(2F+1)}{3(F+1)(2F+3)}} \begin{Bmatrix} F & 2 & F \\ J & I & J \end{Bmatrix} \alpha_{nJ}^{(2)} \tag{2.15c}$$

where the reduced dynamical scalar polarizabilities  $\alpha_{nJ}^{(K)}$  for  $K = \{0, 1, 2\}$  corresponding to scalar, vector and tensor shifts of fine-structure level  $|nJ\rangle$ , and are given by

$$\begin{aligned}
 \alpha_{nJ}^{(K)} &= (-1)^{K+J+1} \sqrt{2K+1} \sum_{n'J'} (-1)^{J'} \begin{Bmatrix} 1 & K & 1 \\ J & J' & J \end{Bmatrix} |\langle n'J' || \mathbf{d} || nJ \rangle|^2 \\
 &\quad \times \frac{1}{\hbar} \left( \frac{1}{\omega_{n'J'nJ} - \omega - i\gamma_{n'J'nJ}/2} + \frac{(-1)^K}{\omega_{n'J'nJ} + \omega + i\gamma_{n'J'nJ}/2} \right)
 \end{aligned} \tag{2.16}$$

Here the notation are  $\omega_{n'J'nJ} = \omega_{n'J'} - \omega_{nJ}$  for angular frequency and  $\gamma_{n'J'nJ} = \gamma_{n'J'} + \gamma_{nJ}$  for angular linewidth, for transition between fine-structure levels  $|nJ\rangle$  and  $|n'J'\rangle$ . The term in the curly brace of the form  $\begin{Bmatrix} j_1 & j_2 & j_3 \\ j_4 & j_5 & j_6 \end{Bmatrix}$  represents the Wigner 6-J symbol.  $\langle n'J' || \mathbf{d} || nJ \rangle$  is the reduced electric dipole matrix element. We shall next discuss the three terms from equation 2.14.

### Scalar light shift term

The first term is the scalar light shift which depends on the quantum numbers  $\{n, J\}$  of the atomic state  $|nJFM\rangle$ , and the intensity and wavelength of the light field interacting with the atom. To understand intuitively the implication of scalar light shift in optical dipole trapping, lets consider a simple 2-level atom with levels  $|nJ\rangle$  and  $|n'J'\rangle$ . It can be shown using equation 2.14, 2.15(a), 2.16 that the scalar light shift for the ground state of an atom due to a far off-resonance optical field is approximately given as [32]

$$U_{\text{scalar}} \propto -\frac{|\mathcal{E}(\mathbf{r})|^2}{\Delta} \begin{Bmatrix} 1 & 0 & 1 \\ J & J' & J \end{Bmatrix} \tag{2.17}$$

where  $\Delta = \omega - \omega_{n'J'nJ}$  is the detuning of the light field from the frequency for the transition  $|nJ\rangle \leftrightarrow |n'J'\rangle$ . Assuming the D2 line of Cs with  $n = 6$  and  $\{J, J'\} = \{1/2, 3/2\}$ , one can express the scalar light shift of the ground state to be  $U_{\text{scalar}} \propto I(\mathbf{r})/\Delta$ , where  $I(\mathbf{r}) \propto |\mathcal{E}(\mathbf{r})|^2$ . This change in potential energy causes a force on the atom proportional to  $-\vec{\nabla}U_{\text{scalar}} \propto -\vec{\nabla}I(\mathbf{r})/\Delta$ . This means for given intensity profile a positive (negative) detuned light field exerts a force which tries to move the atom in the direction of decreasing (increasing) intensity. This means that for a red (blue) detuned light field,  $\Delta$ , is less (greater) than zero, the atom tries to minimize its energy by seeking the maxima (minima) of the field intensity. Based on this principle we use a combination of red and blue-detuned light fields to trap Cs atoms. More details on the consequence of scalar light shift in our optical dipole trap implementation is discussed in section 2.5.1 and 2.5.4.

### Vector light shift term

The second term of the equation 2.14 gives the so called vector light shifts for a given state.  $F$  is the quantum number for the total angular momentum of the atom,  $\mathbf{F}$  and  $M$  is the quantum number for the projection  $F_q$  of  $\mathbf{F}$  onto the quantization axis  $q$  such that  $M = m_F$ , such that  $-F \leq m_F \leq F, \forall m_F \in \text{integer}$ . One can see that the vector light shift term is therefore dependent on the quantum number  $M$  of the Zeeman manifold corresponding to  $F$ . Vector light shift of the Zeeman manifold is analogous to the Zeeman splitting with an actual magnetic field. They are hence, also referred to as being caused by the presence of a fictitious magnetic field [63] which depends on the quantum numbers  $n, J$  and  $F$  and on the local field polarization vector  $\mathbf{u}$  as  $i[\mathbf{u}^* \times \mathbf{u}]$ . More specifically, the latter is proportional to the ellipticity of the local electric field polarization. Hence, for a linearly polarized electric field the vector light shift is zero. We try to use a trapping configuration where the vector light shift is minimized at the mean position of the atoms in the trap. More details on the exact trap implementation and its consequence is discussed in section 2.5.5.

### Tensor light shift term

The tensor light shift is given by the third term of equation 2.14 where the tensor polarizability is given by equation 2.15(c). The reduced dynamical tensor polarizability given by 2.16 for  $K = 2$  is zero when  $J = 1/2$  owing to the Wigner 6- $j$  symbol. This means that the tensor light shifts for neutral Cs atoms in their ground state is zero. However, for the excited state the tensor light shift is non-zero which we shall explore more in section 2.5.6. In the following section, we analyse quantitatively some of the features of our nanofiber based trap.

## 2.5 Properties of our nanofiber based trap for neutral Cs atoms

In this section, I will use the concepts developed in the previous section to analyse quantitatively the properties of the nanofiber-based two-color optical dipole trap that we use to trap atoms in our lab. Figure 2.6 shows the usual polarization configuration of the trapping lasers with respect to the nanofiber (in grey) and atoms (yellow).

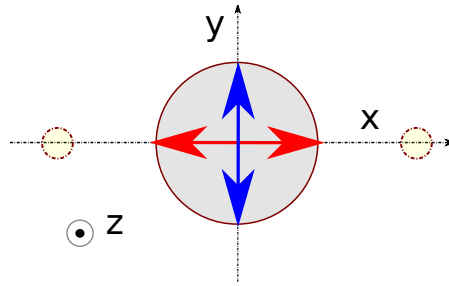


Figure 2.6: A schematic showing the main polarization axis of the blue-detuned (blue arrow,  $y$ - $z$  plane) and red-detuned (red arrow,  $x$ - $z$  plane) trapping light fields in the transverse plane of the nanofiber waist (grey). The atoms (yellow) are trapped in the  $x$ - $z$  plane defined by the polarization of the red-detuned trap laser. The near-resonance probing field (not shown here) is also usually quasilinearly polarized similar to the red-detuned trap laser.

### 2.5.1 Radial confinement

We use a two color optical dipole trap in the evanescent field of the nanofiber to trap neutral Cs atoms. For this, we send two quasilinearly polarized far off-resonant red- and blue-detuned optical fields at 935 nm and 685 nm, respectively, through the nanofiber to create a dipole trap in the evanescent field of the nanofiber (solid black line in Figure 2.7). The intensity of the trapping field decays exponentially in the evanescent field of the fiber but does so more slowly for red- than for the blue-detuned optical trap field. Since the red-detuned field provides an attractive potential (red solid line) which lowers the energy of the atoms as the intensity of the field increases, therefore it tries to pull the atoms closer towards the nanofiber surface. The blue-detuned trapping field prevents the atoms from colliding with the surface of the nanofiber. It provides a repulsive potential (solid blue line) that increases the energy of the atoms as it approaches the nanofiber surface thereby making it energetically less favorable for atoms to approach the nanofiber surface. By suitably choosing the powers of red- and blue-detuned optical fields one can achieve a local minimum such that moving closer to or further from the surface increases the energy of the atom owing to the dominating repulsive or attractive force, thereby confining the atoms radially. A typical trapping potential ( $U_{\text{total}}$ ) is shown by the solid black line in the Figure 2.7. The red and blue lines show the attractive ( $U_{\text{red}}$ ) and repulsive potential ( $U_{\text{blue}}$ ) respectively whereas the dashed green line shows the Van der Waals potential<sup>4</sup> ( $U_{\text{VDW}}$ ). A near resonance probe field can also shift the potential energy shown by the dotted blue and red lines for positive and negative detuned probe field, respectively. This shift is discussed more in section 2.5.7.

<sup>4</sup>The Van der Waals potential can be approximately given as  $U_{\text{VDW}}(r) = -C/(r-a)^3$  where  $r$  is the position and  $a$  is the fiber radius and  $C$  is some constant which is well defined for a Cs atom near a cylindrical silica surface [32]. The potential is large for small distances and can perturb the atomic energy levels significantly. However, for our trap distances the effect is negligible.

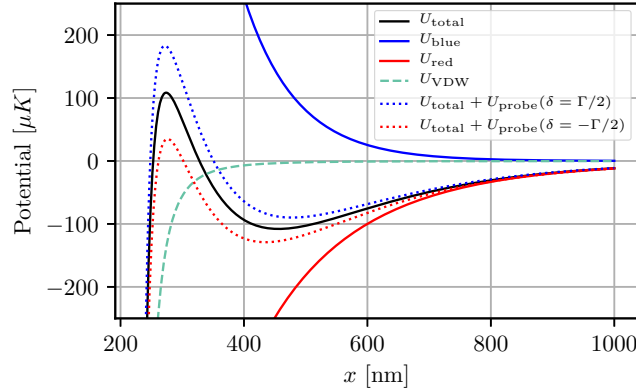


Figure 2.7: Radial trapping potential (black solid line) along  $x$ -axis. The red and blue solid lines showing the attractive and repulsive potential generated from red- and blue-detuned trap lasers at 935 nm and 935 nm respectively. The Van der Waals potential is shown with the dashed green line. The dashed red (blue) line show the perturbation of the radial trapping potential due to addition of a probe field which is red-detuned (blue-detuned) from the  $D_2$ -cycling transition by  $0.5\Gamma_{D_2}$  with power of  $0.1P_{\text{sat}}$  (see section 2.5.7 for more details on this). The other parameters used are fiber radius: 200 nm,  $P_{\text{bluetrap}} = 14$  mW,  $P_{\text{redtrap}} = 2 \times 184$  uW. The polarization configuration is shown in Figure 2.6.

### 2.5.2 Axial confinement

The axial confinement of the atoms is obtained due to the periodicity imposed by the standing wave of red-detuned trap field in the evanescent field of the nanofiber. This is achieved by sending the red-detuned laser from both sides of the nanofiber. The resulting periodic attractive potential confines the atoms along the antinode of the standing wave where the intensity of the red-trap is the maximum and hence the lowest potential energy for the trapped atoms. Figure 2.8(left) shows the periodic trapping potential along the nanofiber in the plane defined by the transverse polarization of the quasilinearly polarized red-detuned trap field. The red and blue colors represent the regions of higher and lower potential energy, respectively.

### 2.5.3 Azimuthal confinement

As was shown in Figure 2.2(bottom), a quasilinearly polarized optical field propagating in the nanofiber waist leads to an azimuthally varying intensity distribution outside the nanofiber waist. The intensity of the quasi-linearly polarized red trap is azimuthally maximum along the main polarization axis. This asymmetry in the intensity distribution of the red-detuned trapping field leads to azimuthal confinement of the atoms such that their mean position is along the polarization axis of the red-detuned trap field. The blue-detuned field further contributes to the azimuthal confinement due to its strong repulsive potential around the fiber at an angle orthogonal to the main polarization of the red-detuned trap laser. Figure 2.8(right) shows the trapping potential in the transverse plane at  $z = 0$ . The red trap and blue trap have transverse polarization along  $x$

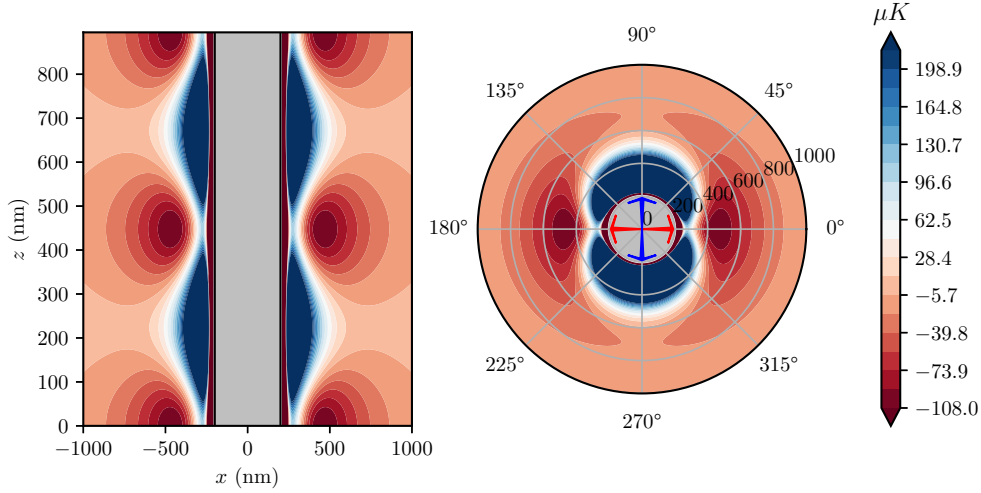


Figure 2.8: Axial (left) and azimuthal (right) trapping potentials. In the left figure, the nanofiber is represented by the grey region and the atoms are trapped in the  $x-z$  plane. The right figure, shows a transverse section view of the plane at  $z = 0$ . The red (blue) arrows at polar angle  $0^\circ$  ( $90^\circ$ ) show the quasilinearly polarized redtrap (bluetrap). Other parameters used are: waist radius = 200 nm,  $P_{\text{redtrap}} = 2 \times 0.184$  mW,  $P_{\text{bluetrap}} = 14$  mW.

and  $y$  axis respectively such that the atoms are trapped in the  $x-z$  plane.

#### 2.5.4 Magic wavelengths: Vanishing differential scalar light shift

The system of nanofiber trapped atoms may exhibit undesired inhomogeneous broadening of the absorption spectrum of the atomic ensemble for a given configuration of the trapping light fields [64]. This may have several contributing factors. At a given time, the trapped atoms oscillating about the minimum of the local trapping potential, will not have the same relative position to their respective trapping minimum. Therefore, due to the asymmetric distribution of trapping light field intensity around the fiber, they may each experience different scalar light shifts of the transition frequency depending upon their instantaneous positions which in turns leads to inhomogeneous broadening of the absorption spectrum of the nanofiber-trapped atomic ensemble. For a single atom, a probing duration longer than the trap oscillation period has a similar broadening effect on the absorption spectrum of the atom. To prevent such trapping laser power dependent broadening, we use the trap lasers at the magic wavelength of Cs where the scalar light shifts of the ground and excited state of a transition are the same thereby giving a differential scalar light shift of zero [65,66]. The scalar light shifts for each state is dependent on the respective scalar polarizability, as can be seen from equation 2.15(a). Therefore, calculation of magic wavelength reduces down to finding the wavelength for which the pair of states have the same scalar polarizabilities.

Figure 2.9 shows the calculated scalar polarizabilities versus wavelength for ground (blue solid line) and excited (orange line) state in the transition :  $6S_{1/2}, F = 4 \rightarrow 6P_{3/2}, F' = 5$  in a

Cs atom. Since we probe the Cs atoms at this transition, therefore, we want the same scalar light shift for both the involved states which is indicated in the figure by the crossing of the orange and blue lines. The left and right figure shows the points where the differential scalar light shifts for the blue- and red-detuned far off-resonant fields is zero. This is roughly  $\sim 935$  and  $\sim 686$  nm,<sup>5</sup> respectively.

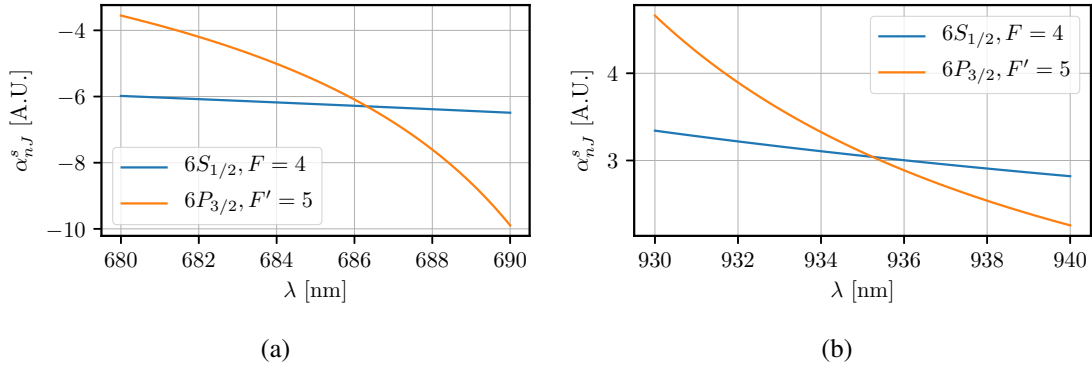


Figure 2.9: The scalar polarizabilities of the excited state (orange) and ground state (blue) for wavelengths blue-detuned (left) and red-detuned (right) to the D2-line. The point where they are equal, leading to vanishing differential scalar light shift for the D2 cycling transition, is called the blue- or red-detuned magic wavelength. In our case, this happens roughly at  $\sim 686$  nm and  $\sim 935$  nm.

### 2.5.5 Vanishing vector light shift

The vector light shifts requires elliptical polarization of the light field (see section 2.4). The red-trap field is quasilinearly polarized and counterpropagating. When the power of the counterpropagating pair of red-detuned trap fields are equal, the longitudinal electric field ( $z$ -component) from the two arms are equal but out of phase. This leads to an effective linear polarization at the position of the atoms, and hence vanishing vector light shifts due to the red-trapping fields.

The blue-detuned trap field is quasilinearly polarized, but its transverse polarization plane is orthogonal to the trapping plane as shown in Figure 2.6 It exhibits no ellipticity in polarization at the position of the trapping minimum. However, around the trapping minimum it exhibits a gradient of ellipticity which leads to a spatially varying Zeeman state dependent light shift. This is similar to applying a gradient of magnetic field [67] that is zero at the azimuthal trapping minimum and increases in magnitude on either side. By reducing the extent of the spatial spread of the atomic centre-of-mass motion around the trapping minimum, for example by using

<sup>5</sup>The tensor light shift for the excited  $6P_{3/2}, F=4$  Hyperfine state manifold is small compared to the scalar light shift but non-negligible for the typical trapping fields power and polarization configuration used by us. Accounting for the range of total light shift (scalar and tensor), Reference [65] quotes a theoretically more accurate value ( $\sim 685.5$  nm) than what considering merely the scalar light shift predicts here .



degenerate Raman cooling [39], one can reduce the Zeeman manifold splitting and hence counter any inhomogeneous broadening effects. An alternative solution would be to get rid of the local ellipticity of the polarization by using a running standing wave for the blue-detuned trap laser [66].

### 2.5.6 Nonvanishing tensor light shifts

The tensor light shift ( $U_{\text{tensor}}$ ) for the ground state  $6S_{1/2}$  is zero but non-vanishing for the  $6P_{3/2}$  excited state hyperfine manifold. To quantify it for our nanofiber trapped atoms, we use the simplified expression [62]:

$$\Delta E_{\text{tensor}}(\mathbf{r}) = \frac{1}{4} |\mathcal{E}(\mathbf{r})|^2 (1 - 3|e_0|^2) \alpha_{nJF}^T \frac{3M^2 - F(F+1)}{2F(2F-1)} \quad (2.18)$$

where,  $e_0 = e_z$  is the normalized  $z$ -component of the electric field unit vector  $\vec{E}(\mathbf{r})/|\vec{E}(\mathbf{r})|$ , and  $\alpha_{nJF}^T$  is the dynamical tensor polarizability given by equation 2.15(c), and  $M = m_F$ , where  $\{-F \leq m_F \leq F\}$  represents the Zeeman manifold corresponding to the quantum number  $F$ . Note that the expression is an even function of the quantum number  $m_F$ . The tensor light shifts calculated for the excited state Zeeman manifold  $6P_{3/2}$ ,  $F = 5$  is shown in Figure 2.10. The left plot shows the light shift for a standing wave corresponding to different powers of the redtrap quasilinearly polarized along  $x$ -axis. The centre plot shows the same but for the blue trap quasilinearly polarized along the  $y$ -axis. Note that due to opposite detuning, the tensor light shifts for a given Zeeman level have opposite signs for the red- and blue-detuned trap laser respectively. Figure 2.10(right) shows the tensor light shift for our specific trap powers used in our experimental configuration (specified by the dashed line in the left and centre figures). The red, blue and green colors in the Figure 2.10(right) represent the tensor light shift due to the red-detuned trap laser only, blue-detuned trap laser only, and both of them combined, respectively, for each Zeeman sublevel. We notice that the tensor light shifts are almost negligible for us when compared to the excited state linewidth ( $\Gamma_{D2}$ ).

### 2.5.7 Light shift from detuned probe laser

As we saw in section 2.4, the change in the potential energy of an atom (due to scalar light shift) is inversely proportional to the detuning for a far off-resonance fields. However, when probed with a near-resonance probing field where the detuning is of the order of the excited state linewidth  $\Gamma$ , the energy eigenstates of the unperturbed atom is no longer an eigenstate of the system, as can be seen from a dressed-state formalism. In other words, the expression 2.12, and hence 2.14 cannot be used to find the optical light shifts as the unperturbed states are no longer good eigenstates for the system. However, one can solve this by using another approach. Using the Bloch equations [68], the steady state dipole interaction term for a probe field (electric field and detuning :  $\{\vec{E}, \delta\}$ ) can be written as:

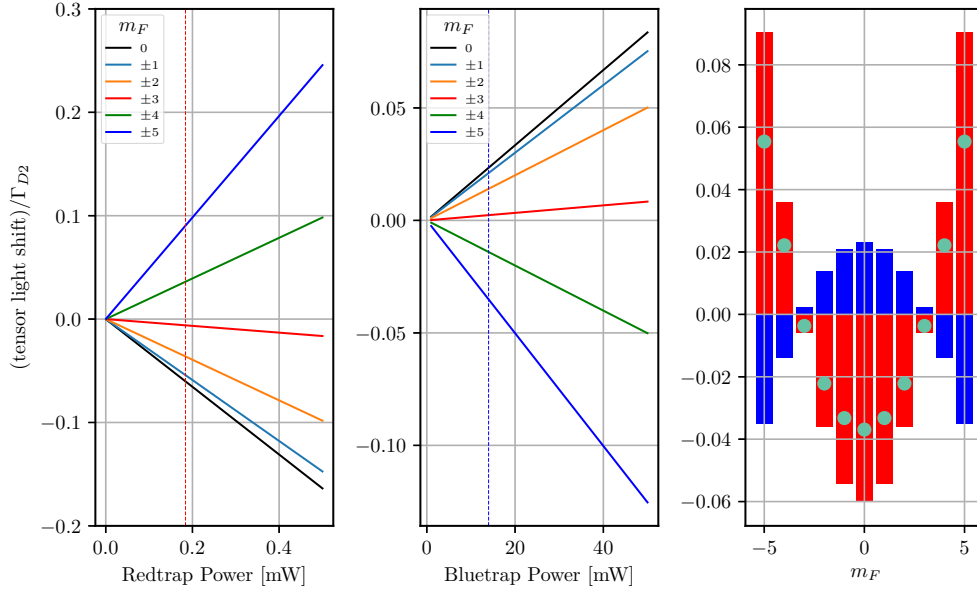


Figure 2.10: Tensor light shifts for the excited state  $6P_{3/2}$ ,  $F = 4$  hyperfine manifold for different powers of redtrap field (left) and bluetrap field (centre) and for our specific experimental configuration used (right). The  $y$ -axis has tensor light shifts normalized to linewidth of the Cs D2 cycling transition ( $\Gamma_{D2} = 2\pi \cdot 5.22\text{MHz}$ ). The experimental configuration used corresponds to the dashed lines in the left and centre plots.

$$\begin{aligned}
 \Delta E &= \langle \vec{d} \rangle \cdot \vec{E} \\
 &= \langle \vec{d} | 1 \rangle \langle 2 | + \vec{d}^* | 2 \rangle \langle 1 | \rangle \cdot \vec{E} \\
 &= \vec{d} \cdot \vec{E} \langle \rho_{12} + \rho_{21} \rangle \quad (\text{assuming } \vec{d} \text{ is real}) \\
 &= \hbar \Omega \times \frac{\Omega \delta}{\delta^2 + \Omega^2/2 + \Gamma^2/4}
 \end{aligned} \tag{2.19}$$

The Rabi-frequency  $\Omega$  can be obtained as [56]

$$\Omega = \Omega_{21} = \Omega_{12}^* = \frac{1}{\hbar} (\vec{d}_{21} \cdot \vec{\mathcal{E}}) = \frac{1}{\hbar} \sum_{q=0,\pm 1} (-1)^q d_{21}^{(q)} \mathcal{E}_{-q} \tag{2.20}$$

where,  $\mathcal{E}_{-q}$  represents the spherical tensor components of the electric field  $\vec{E}$  defined as  $\mathcal{E}_0 = E_z$ ,  $\mathcal{E}_{\pm 1} = (\mp E_x - i E_y)/\sqrt{2}$ , and the dipole matrix element for state  $|1\rangle = |FM\rangle$  and  $|2\rangle = |F'M'\rangle$  is given by [56]:

$$d_{M'M}^{(q)} = (-1)^{I+J'-M'} \langle J' \| D \| J \rangle \sqrt{(2F+1)(2F'+1)} \begin{Bmatrix} J' & F' & I \\ F & J & 1 \end{Bmatrix} \begin{pmatrix} F & 1 & F' \\ M & q & -M' \end{pmatrix} \tag{2.21}$$

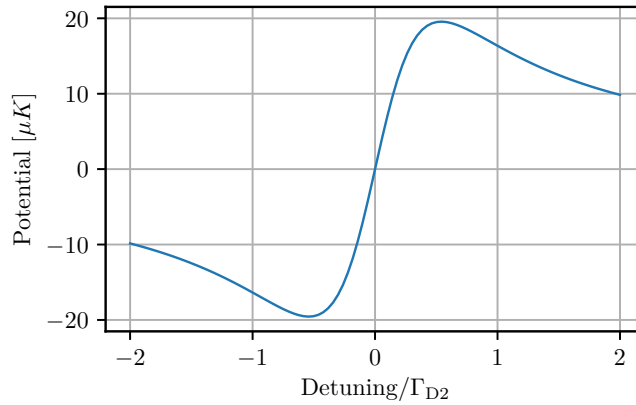


Figure 2.11: Light shift due to a detuned probe with power  $0.1P_{sat}$  at a distance corresponding to the trapping minima in Figure 2.7.

Figure 2.11(a) shows the resulting light shift assuming probe power to be  $0.1P_{sat}$ <sup>6</sup>, transition  $6S_{1/2} \rightarrow 6P_{3/2}$ , with  $\langle J' || D || J \rangle = 5.38 \times 10^{-29} \text{ C m}$ . Such a light shift is usually not important as the atoms are probed with lower powers as we shall see in the next chapter. However, there might be situations where one would like to probe the atoms with a strong resonant light field. In such a situation, the potential energy shift and the resulting acceleration of the atoms must be considered in addition to the problem of heating due to scattering probe photons.

<sup>6</sup> $P_{sat}$  is defined as the on-resonance optical power sent through a waveguide which saturates an atom trapped around it for a given atom-fiber distance of 250 nm.



Die approbierte gedruckte Originalversion dieser Dissertation ist an der TU Wien Bibliothek verfügbar.  
The approved original version of this doctoral thesis is available in print at TU Wien Bibliothek.

# Implementation of Nanofiber-based light-matter interface

## 3.1 Introduction

The nanofiber based platform for trapping neutral atoms was first proposed by Fam Le Kien et. al [32]. The trapping scheme involved sending two far-off resonant light fields through the nanofiber to realize an optical dipole trap potential for the neutral atoms in the evanescent field mode of the fiber. Its first realization was done by our group [64]. Since then it has attracted a lot of interest from other research groups [66, 69–71] owing to its salient features such as the ability to obtain high optical depth with fewer atoms [64, 72], large ground state coherence times [38], chiral interaction with matter [41], high trapping lifetime [39] and inherent optical fiber coupling. A nanofiber-based optical dipole trap for neutral Caesium atoms is well suited for the implementation of quantum hybrid systems [73]. The intrinsic coupling of a nanofiber-based system to an optical fiber makes them ideal for application in quantum information processing and communication (QIPC) protocols enabling future quantum technologies [24, 74]. Therefore, a lot of effort has gone into realizing such a system with even better characteristics [39, 46, 66, 67, 72].

In this chapter, I will first present the second generation experimental setup from our group for realizing nanofiber-based trapping of neutral atoms. I started my PhD work by contributing to the design and construction of the setup from scratch. In the first half of the chapter, I will describe the critical features of the setup and reasons for having them. The second half of the chapter is dedicated to explaining the various characterization methods used for measuring the defining parameters of our system such as optical depth, atom number, filling factor etc.

## 3.2 Experimental setup

In this section, I will present the details of the various components of the experimental setup. In the first subsection, I will present the vacuum setup where the tapered optical fiber (TOF) is hosted. I will describe methods to characterize the transmission and polarization properties of the nanofiber once it is inside vacuum. In the next section, the optics setup that is needed to realize the two-color dipole trap is presented. Then, I will describe the magneto-optical trap (MOT) that is used to precool the cesium atoms before they are trapped in the two-color optical dipole trap. In this context, I will describe the construction of magnetic coils, the MOT setup and alignment procedure. I will also touch upon the experimental control hardware and the python-based control program designed by us. In the last part of this section, I will describe the detection setup for measuring the transmission at the output of the nanofiber setup. Lastly, I will describe some of the results from the characterization measurements done for our system. An understanding of the characterization methods will be useful in chapter 5.

### 3.2.1 Ultra high vacuum setup

#### 3.2.1.1 Chamber design

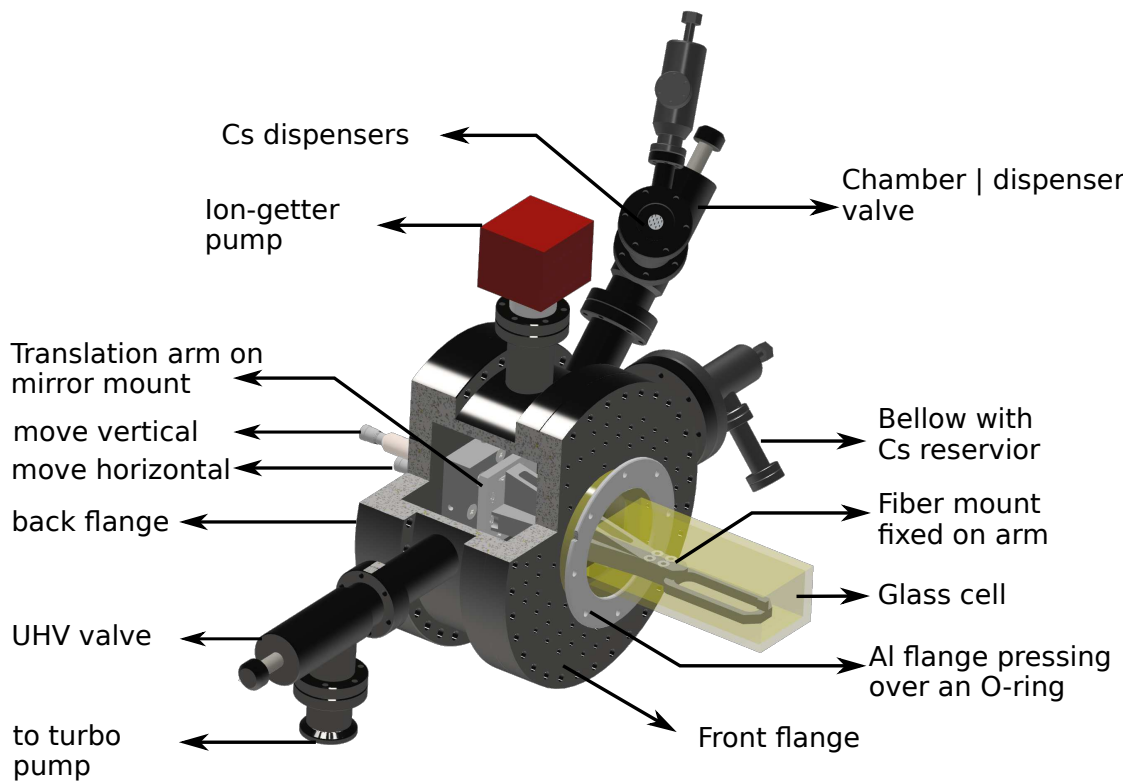


Figure 3.1: The main chamber with the glass cell. The cut-out in the chamber steel body shows a 2D-translation mechanism for moving the fiber waist in horizontal and vertical directions.

The designed chamber and the glass cell is shown in Figure 3.1. The experiment is performed in the glass cell (actual glass cell depicted in Figure 3.2(right)) which contains the nanofiber-waist section on an aluminium mount. The glass chamber is attached to a non-magnetic steel chamber on one of the big flanges which has a circular hole cutout to allow the fiber mount to extend into the glass chamber. The metal glass junction is sealed by pressing a fairly malleable indium metal wire in between the glass cell base. To avoid cracking the cell the pressure is applied via a soft Viton o-ring onto the base plate of the glass cell using a circular aluminium plate from the top. The steps involved in making the Indium seal and the final setup with the glass cell is shown in Figure 3.2. The steel chamber (shown in Figure 3.1) is a cylinder with front flange having a circular cutout on which the glass cell is attached. The back flange has the fiber inlets and feed-throughs for translating the fiber mounts. The circular side of the steel chamber has five different tube outlets with CF flange connection through which we attach additional components like turbo-pump, pressure gauge, ion-getter pump, Cs dispensers and a elemental Cs reservoir. For more details on the design of the chamber, the feed-throughs and the fiber translation stage, please refer to my colleague's thesis [75].

The first tube (front view, right) in the figure is connected to a Cs reservoir in a flexible bellow separated from the main chamber by an angle valve (see Figure 3.1). The second tube

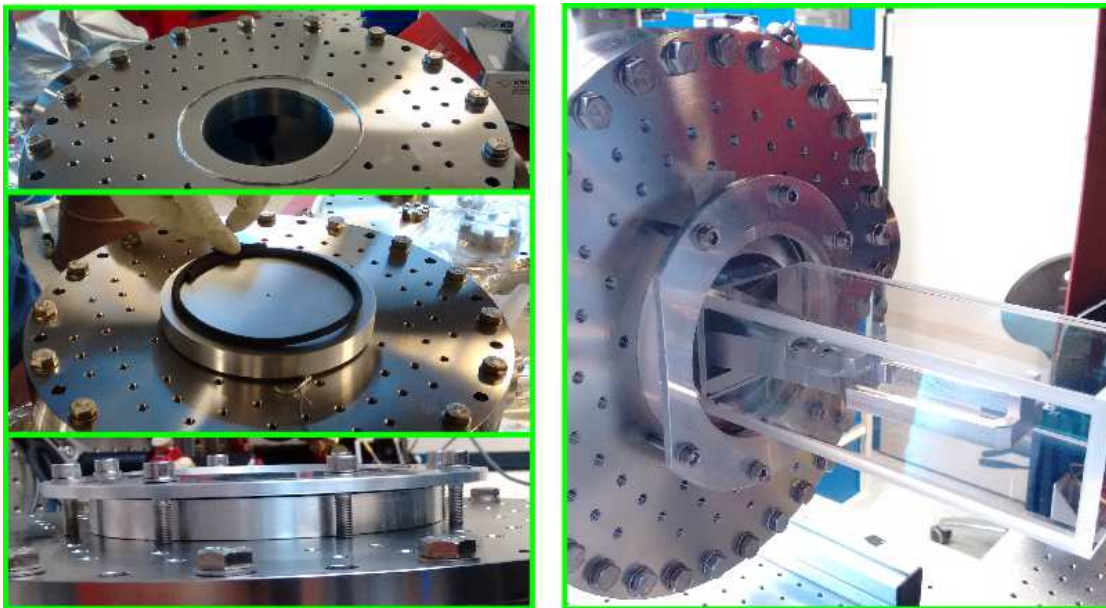


Figure 3.2: Photo showing steps involved in making an indium seal between glass and metal. (left: top to bottom) First an Indium metal wire is joined end-to-end in a circle. The wire is then pressed with the metal plate (emulating the base of the glass cell). An O ring is placed on the plate and an aluminium ring is tightened from the top pressing the O-ring which presses the base plate (glass cell base in the right figure) which in turn flattens the Indium wire which fills the empty spaces or irregularities at the microscopic level. The wire, which is flattened as a result of the force, separates the atmosphere from vacuum inside the chamber.

is connected to a sub-assembly of valves and tubes which is separated from the main chamber by an angle valve. The sub-assembly consists of a T shaped metal tube, one end of which has an angle valve which allows one to access the tube from outside via a flange. The other end of the T-shaped tube hosts 6 Cs dispensers. The sub-assembly with the valve allows us to replace the Cs dispensers if needed without affecting the vacuum in the main chamber. The third tube of the main chamber is connected to a NEX Torr UHV pump which has a passive getter pump in combination with a small ion pump that pumps the noble gases. The fourth tube is connected to a ATMion pressure gauge which is capable of measuring pressure from  $10^3$  mbar down to  $10^{-8}$  mbar. Therefore, combining the pressure-gauge and the NEX Torr ion-getter pump, we are able to monitor the pressure inside the chamber at all times. The fifth tube is connected to a turbo pump with an UHV angle valve separating the turbo-pump from the vacuum chamber. The turbo pump uses a scroll pump as pre-pump.

#### 3.2.1.2 Caesium source

As indicated in the previous section, the Cs inside the chamber comes mostly from the Cs dispensers and partly the Cs reservoir (elemental Cs). The Cs dispenser wire from SAES Getters are supplied with around 6 A of current on a regular basis to dispense out Cs atoms while the Cs reservoir is maintained at room temperature. In our observation, the dispensers are a reliable source of Cs atoms. The elemental Cs was incorporated following an incident <sup>1</sup> where the previously used nanofiber contained crystals of Cs oxide on the surface. We speculated that Cs dispensers could be a source of oxygen based impurities as they contain alkali-metal chromate plus a reducing agent [76] necessary for dispensing the alkali metal. Therefore, to avoid any possible contamination, we also decided to incorporate the elemental Cs reservoir.

#### 3.2.2 Nanofiber integration into the setup

The nanofiber section is part of a 2 m long single mode fiber. We use SM800 fiber from fibercore with a  $\sim 660$  nm cutoff and specified operating wavelength 800 – 980 nm. This fiber is well suited for an experiment with Cs atoms as the specified optical operating range covers both D1- and D2-lines of the Cs atom. We choose a non-polarization maintaining fiber because otherwise, it will not be suitable for aligning the polarization at the nanofiber waist. The two ends of the fiber are attach to a single mode pigtailed fiber connector (thorlabs) which allows the light to be coupled into the fiber. While pulling the nanofiber, we characterize the transmission of the fiber at 852 nm. In our case, the transmission of the fiber was  $> 99\%$  for this wavelength. However, once the fiber is put into the chamber, the losses through the fiber increase due to bending or stress at various points of the fiber or due to Cs adsorption <sup>2</sup>. Therefore, it is important to

---

<sup>1</sup>An scanning electron microscopy (SEM) was performed on one fiber sample that had to be discarded due to gradual loss of transmission. We found that the fiber was covered by unknown crystalline structure of sub-wavelength dimensions, which after EDXRD (Energy dispersive X-Ray Diffraction) was determined to be a complex oxide of Cs. In light of the new developments, we decided to install a Cs reservoir in addition to Cs dispensers as a source of Cs atoms.

<sup>2</sup>At times, when the nanofiber section is cold it can temporarily accumulate Cs deposit on the surface owing to surface adsorption which can lead to significant losses for weak near-resonance optical fields. To prevent this, we make sure that we always send a few milliwatts of a blue-detuned laser beam through the fiber-waist.



characterize the transmission of the fiber after it has been put into the chamber. Measuring the losses allows one to estimate the power of the trapping fields needed to be coupled into the fiber to obtain a reasonable trapping potential for the atoms. These estimated powers usually serve as the starting point for further optimization of the trap.

### 3.2.2.1 Nanofiber transmission measurement

To measure the transmission properties of the nanofiber we use the method published recently by our group [77]. The setup is shown in Fig. 3.3.

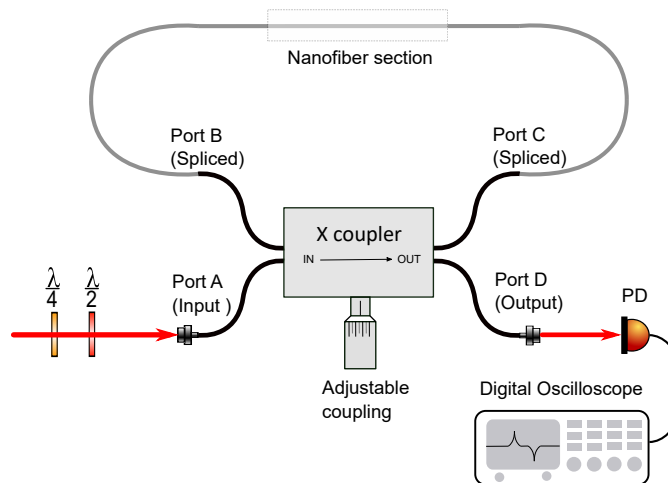


Figure 3.3: Experimental setup to measure the nanofiber transmission. The light is sent into one of the input ports of an X-coupler and the transmission is monitored on one of the output ports, while the nanofiber is spliced to the other input and output port. The transmission is monitored using a photodiode connected to an oscilloscope.

The two ends of the TOF including the nanofiber are spliced to input port A and output port B of an X-coupler<sup>3</sup>, thereby forming a ring resonator cavity. By swapping the ends of the 2 m fiber, one can measure transmission in the other direction. The frequency of the input light field which is sent into the system by input port A of the X-coupler is scanned using the piezo element in the external cavity of a diode laser. We use light with a wavelength of 852 nm light field derived from a Toptica TA amplifier for this purpose. One must ensure that the power sent into the nanofiber is not more than a mW because the amplification of the light field owing to the cavity can overheat and break the nanofiber. The transmitted output light field from port D is monitored on an oscilloscope using a photodiode. The input light field polarization is adjusted via the  $\lambda/4$  and  $\lambda/2$  waveplates such that the light couples to only one of the two orthogonal polarization modes supported by the ring-resonator cavity. To avoid any polarization drifts due to temperature fluctuations all the fiber segments are taped to the surface of the optical table. Using

<sup>3</sup>An X-coupler is a tunable fiber optic beam splitter. The light sent through the two input fiber ports can couple evanescently to each other and the coupling can be regulated from undercoupled to overcoupled regime via the knob. The model used was F-CPL-830-N-FA from Newport.

### 3. IMPLEMENTATION OF NANOFIBER-BASED LIGHT-MATTER INTERFACE

the adjustable coupling knob of the X-coupler, and the polarization optics of the input field as the tuning parameters, we align the system at critical coupling where the losses from port A→D equal the round trip losses in the ring-resonator. By recording the transmission spectrum of the nanofiber cavity at critical coupling, one can extract the Finesse ( $F$ ) of the cavity by estimating the free-spectral range ( $\nu_{FSR}$ ) and the field-decay rate ( $\kappa_0$ ), and then calculate the losses as [4]:

$$F = \frac{\nu_{FSR}}{\kappa_0} \approx \frac{2\pi}{1 - \rho} \quad (3.1)$$

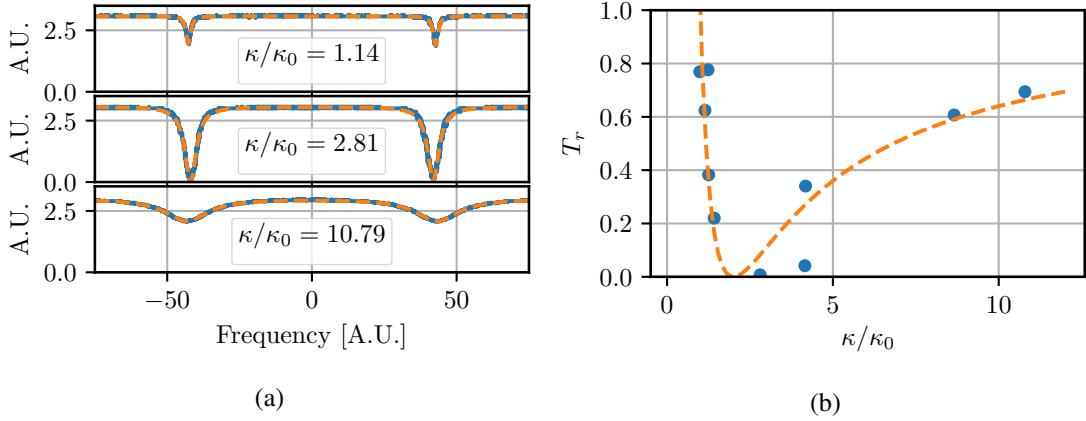


Figure 3.4: (a) Three example transmission spectra of the nanofiber resonator cavity at different coupling strengths with top, middle and bottom plots showing undercoupled, critical coupling and overcoupling. (b) For different coupling to the ring resonator the total decay rate ( $\kappa$ ) and transmission at resonance ( $T_r$ ) are plotted. From the fit (dashed line) one can extract the unloaded decay rate ( $\kappa_0$ ) which is then used to normalize the  $x$ -axis.

The above approximation is valid for small losses ( $< 10\%$ ). An important feature of this measurement of Finesse is that one does not really need a frequency calibration as it is a ratio of two frequencies in equation 3.1. The absorption linewidth ( $2\kappa$ ) is proportional to the total power losses in the system (from A to D) for different values of couplings. At critical coupling, the losses in the ring resonator (B-C-B, see Fig 3.3) equals to the coupling from the transmission fiber (A-D, see Fig 3.3) to the ring resonator. At this value, the on resonance transmission goes to zero. Three sample transmission spectra recorded at different coupling strengths are shown in Figure 3.4a. From the spectra one can calculate the set of field decay rate ( $\kappa$ ) and on-resonance transmission ( $\{\kappa, T_r\}$ ) where the subscript  $r$  denotes on-resonance. We then fit this data to the theoretical transmission  $T_r = |t|^2$  where  $t = (2\kappa_0 - \kappa)/\kappa$ , [77] for different losses ( $\kappa$ ) to obtain the ( $\kappa_0$ ), which is the unloaded field decay rate. From that one can extract the Finesse and hence the total losses per round trip ( $\rho$ ). The transmission losses in the fiber is  $\rho/2$  as the decay rate of the nanofiber ring resonator is half the total losses at critical coupling as also shown by Fig 3.4b where the transmission goes to zero at  $2\kappa_0$ . From  $\kappa_0$ , one gets the transmission loss through the nanofiber assuming that in- and out-coupling to/from the X-coupler are lossless. From this

analysis, we infer a cavity finesse of  $208 \pm 6$  which translates to losses of  $1.49 \pm 0.04\%$  for one pass through the TOF for an optical field at 852 nm.

### 3.2.2.2 Coupling optics for input into nanofiber

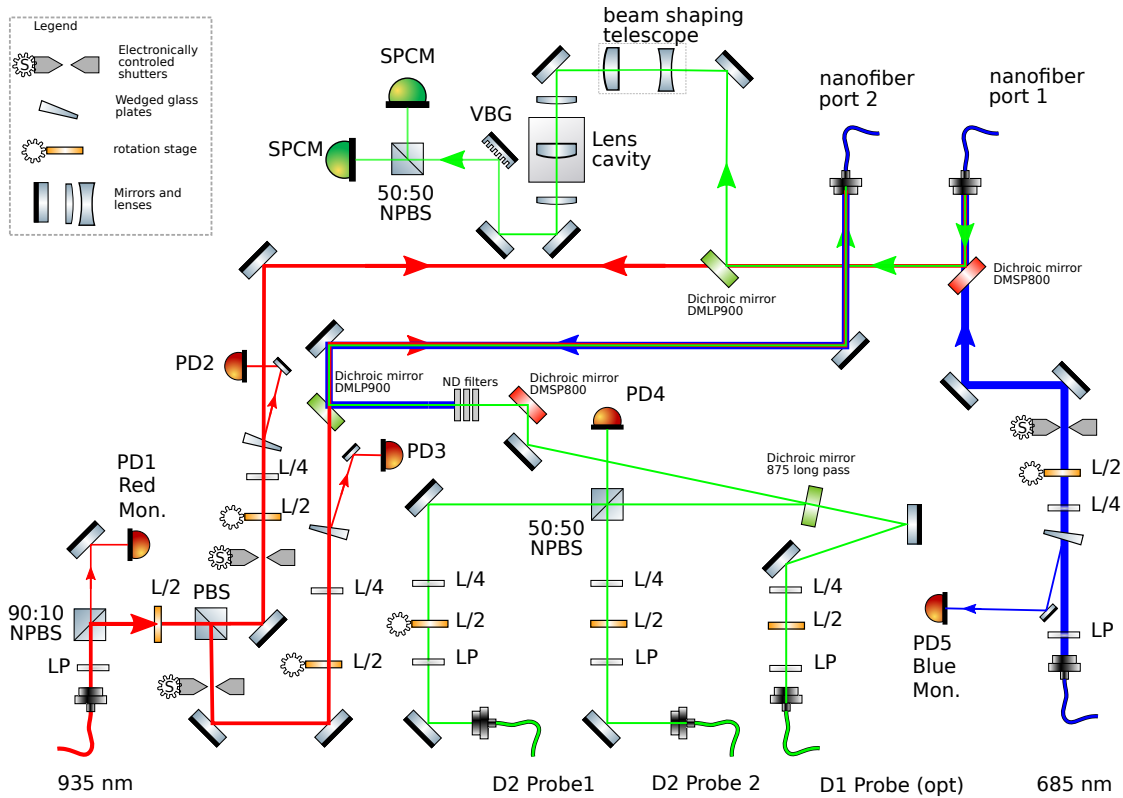


Figure 3.5: The input setup comprises of 5 possible light fields coupled into the fiber. The red-detuned trap, blue-detuned trap laser and probe fields are represented by red, blue and green paths respectively. In the top centre is the probe filtering and detection setup. The labels LP, L/2 and L/4 correspond to linear polarizer, half- and quarter-waveplate.

The trapping light fields at 685 nm and 935 nm along with 852 nm probe fields are combined as shown in Figure 3.5. All the lasers are present on a separate optical table. The light from each laser is coupled into 10m long polarization maintaining fibers and brought to the experimental table. Before the optical fields are combined, as shown in Figure 3.5, each field is sent through an acousto-optic modulator (AOM) in a single-pass (685 nm, 935 nm) or double-pass (852 nm, 894 nm) configuration which allow us to modulate the intensity of each beam as well as to stabilize the intensity via appropriate feedback to the RF power supplied to the AOMs. The double-pass configuration allows for a larger frequency tunability of the 852 nm (cooler / probe laser) and 894 nm (repumping / probe) laser. The purpose of the cooling and repumping laser (See figure 2.5) is to laser cool the atoms, and will be discussed more in the section 3.2.3. Here, we will briefly outline the setup used for coupling the trapping and probing optical fields

into the nanofiber.

In figure 3.5, there are 5 input ports shown on the bottom, which supply light fields which, after further manipulation are coupled into the nanofiber (left to right: red-detuned trap laser at 935 nm, two probe beams at 852 nm, one probe beam at 894 nm, and blue-detuned trap laser at 685 nm).

A few key details of our setup are as follows. All single mode fibers (except the nanofiber arms) used in our setup are single mode and polarization maintaining such that the light field propagates with its polarization matched to one of its eigenaxis. To compensate for any remaining drifts in polarization and to further increase the polarization purity, we place linear polarizers (denoted by LP) after the fiber outcoupler in all the five paths. These polarizers may convert any remaining polarization fluctuation into intensity changes. To compensate for the fluctuations, we intercept a small but fixed fraction of light via photodiodes PD1 (for red-detuned trap laser), PD4 (for probe beam), PD5 (for blue-detuned trap laser) and stabilize it via feedback on the AOMs as discussed before. Once the polarization and intensity are stabilized, we align the polarization of each light field at the nanofiber waist. In our configuration, the red-detuned trap laser and probe fields have transverse polarization set in the same plane inside the nanofiber waist while the blue-detuned trap laser is set to be orthogonal. The polarization at the nanofiber waist is set for each arm by means of a half- and quarter-wave plate (denoted by  $L/2$  and  $L/4$ ). The polarization alignment procedure is discussed in detail in next section. There are wedged glass plates in each red-detuned trap laser arm which intercept a fraction of the transmitted light field and direct it to photodiodes PD2 and PD3. We are also able to stabilize the transmitted optical power of the trap light fields through the nanofiber. However, the transmitted fields contain signatures of mechanical motion of the nanofiber in the form of polarization fluctuations. Therefore, we avoid using feedback based on the transmitted power of trapping fields due to the risk of amplifying any mechanical motion via periodic feedback. The shutters and some of the setting of the half-waveplates are electronically controlled via the PC. The red-detuned laser beam is split into two beam paths at a PBS to balance the power at the nanofiber waist arriving from each path. These two arms of the red-detuned laser are counterpropagating and form a standing wave in the evanescent field of the nanofiber as discussed in section 2.5.2. We use dichroic mirrors to combine or separate two light fields which are at different wavelengths. For the transmitted probe field the detection optics is discussed in section 3.2.2.4.

#### 3.2.2.3 Polarization variation along long nanofiber waist

In our experiment, the length of our nanofiber waist is more than a centimeter so as to allow trapping a large number of atoms. Therefore, achieving a uniform polarization along the entire nanofiber waist is crucial for reducing the inhomogeneities in trapping and for observing possible collective effects in light scattering by the atomic ensemble [40] (see appendix A). To this end, we are able to align and analyze the polarization for any section of the nanofiber waist (see Figure 3.6).

For aligning the polarization we use a similar setup as shown schematically in the reference [72]. The basic idea of such a setup is as follows. The light field propagating inside the fiber excites the point-like impurities present in the nanofiber waist or on the surface of the nanofiber. These impurities scatter light, maintaining the polarization and phase of the light. We observe the total of the Rayleigh scattering from the impurities on the fiber waist along two orthogonal viewing axis ( $x$  and  $y$  in Figure 2.6) using two CCD cameras. The camera placement, also used for absorption imaging, can be seen in Figs. 3.7 or 3.10). We place a polarizer in front of the camera such that the light polarized longitudinally (along the fiber axis) is blocked, and the camera receives the light polarized in a plane perpendicular to the fiber axis. For a linear dipole polarized along  $\hat{e}$ , the radiative emission power per unit solid angle along  $\hat{r}$  goes as  $\sin^2 \theta$ , where  $\theta = \cos^{-1}(\hat{e} \cdot \hat{r})$ . The impurities in the waist are polarization maintaining dipole scatterers. Therefore, the maximum and minimum brightness of the waist, as observed by the camera, will be dependent on the orientation of the transverse polarization in the nanofiber waist. For polarization perpendicular or along the direction of observation ( $\hat{e} \cdot \hat{r} = 0$  or  $1$ ), the observed emission is maximum or minimum, respectively. To quantify the deviation from perfect linear polarization, we do a visibility measurement where we rotate the transverse polarization of the field inside the nanofiber by using the L/2 and L/4 waveplates, and then measure the difference between the maximum and minimum intensities at the nanofiber waist as seen using the camera. The detailed procedure is described below.

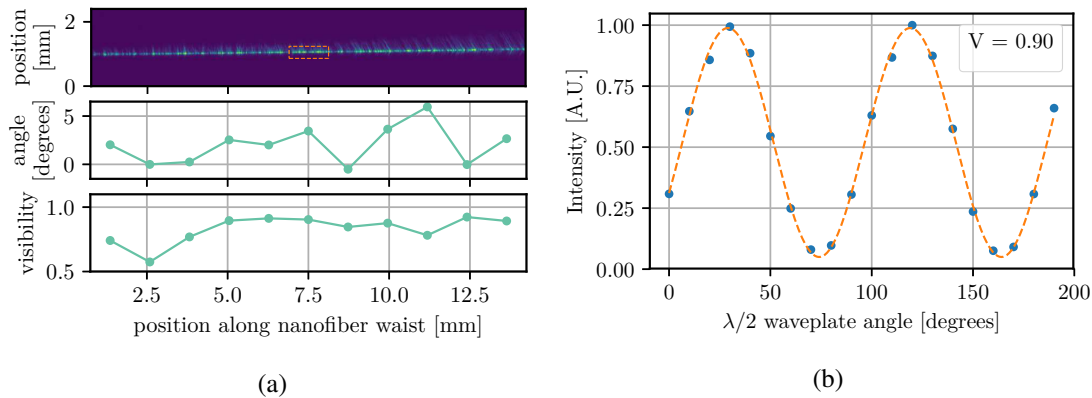


Figure 3.6: Investigating polarization variations along a nanofiber waist longer than 10 mm. (a) (*top*) Light scattered (transverse component) from the nanofiber waist as seen through a camera placed on the side (see horizontal imaging camera placement in Figure 3.7, 3.10); (*centre*) angles indicating the relative orientation of the transverse polarization for different sections of the waist; (*bottom*) visibility measured for each  $\sim 1\text{mm}$  section along the fiber (b) Intensity as a function of the angle of the HWP for the waist region enclosed inside orange rectangle in fig (a)(top). The visibility  $V$  is 90%.

Our imaging system allows us to look at roughly 18 millimeters of the nanofiber waist, allowing us to maximize the visibility (contrast of the fringes) in any desired section of the nanofiber. I automated the polarization alignment of all the fields going through the nanofiber. A

computer script turns a HWP on a motorized precision rotation mount (Thorlabs, K10CR1/M) and records the corresponding scattered light intensity in the region of interest that the user selects (red rectangle in figure 3.6 (left,top)). It then fits a sinusoid  $f(\theta, \theta_0) = C + A \sin^2[2(\theta - \theta_0)]$  to the recorded intensity as a function of HWP rotation angle ( $\theta$ ) and calculates the visibility. For a given angle of the HWP (usually corresponding to minimum of the fringe), we adjust the QWP in the path of the input light field so as to increase the visibility. The visibility measurement and QWP adjustment is done iteratively such that we get the best visibility. We then set the angle of the HWP to set the polarization in the waist to one of the configurations corresponding to maximum or minimum intensity. This corresponds to the best linear polarization configuration achieved by our setup.

Figure 3.6 shows the outcome of such a visibility measurement. In the top panel a fiber waist section roughly  $\sim 14$  mm long is shown. We divide it into 11 sub-regions and calculated the visibility shown in figure (a), bottom panel and the relative transverse polarization angle (a), center, for each of these sections. We infer from these measurement that the visibility is around 80% for most of the fiber section while the transverse polarization fluctuates within  $\sim 8^\circ$  along the entire section of the nanofiber. In Fig. (b), the visibility measurement is shown corresponding to the fiber section in the dashed rectangle in (a), top panel.

#### 3.2.2.4 Detection optics after nanofiber output

Figure 3.5 shows, at the top, the optical setup used to analyze the probe light transmitted through the nanofiber. The probe light field is sent into the nanofiber via port2 and comes out at port1. The transmitted probe light is in the same spatial mode as transmitted red-detuned trap laser @935 nm and (spurious) backreflection of blue-detuned trap laser @685 nm. In addition to trapping fields, it also contains photons arising from Raman Scattering of the trapping light fields in the fiber material. To separate out the transmitted probe field photons, we adopt the following procedure. First, we send the blue-detuned trap laser from the direction opposite to the one from which we send in the probe. This way we avoid having to separate the strongest light field (blue-detuned trap laser) from the weakest field (probe) in the system which would require many more optical filters. Next, we use a pair of dichroic mirrors to separate the probe field coming out of the nanofiber from the trapping fields with an effective suppression of roughly 20 dB of the trapping fields. Next, we send the probe beam through a lens filter cavity with a linewidth of  $\sim 200$  MHz, which filters the probe field from the remaining trapping fields and the Raman-scattered photons spread across tens of Terahertz. This leads to a further suppression of the background count rate on the SPCM by roughly 25 dB. After that we also reflect the output from a holographic volume bragg grating (VBG) (opti grate) with a reflection window of roughly 40 GHz around the Cs D2 line which removes the remaining impurities, offering a further suppression of the contaminating photons by roughly 50 dB. The VBG is placed after the cavity because the lens filter cavity is the most sensitive optical component with respect to its alignment. Therefore, we prefer not to frequently realign the path from nanofiber to the lens-cavity. The remaining light field is coupled into single photon counting modules (Excellitas, dark count  $<50$  Hz) using 50  $\mu\text{m}$  core shielded multimode fibers. Before the multimode fibers, we put a 852 nm laser line filter (Semrock Maxline LL01-852) (suppression roughly 40 dB for background fields) to prevent optical crosstalk between the two SPCMs which can happen

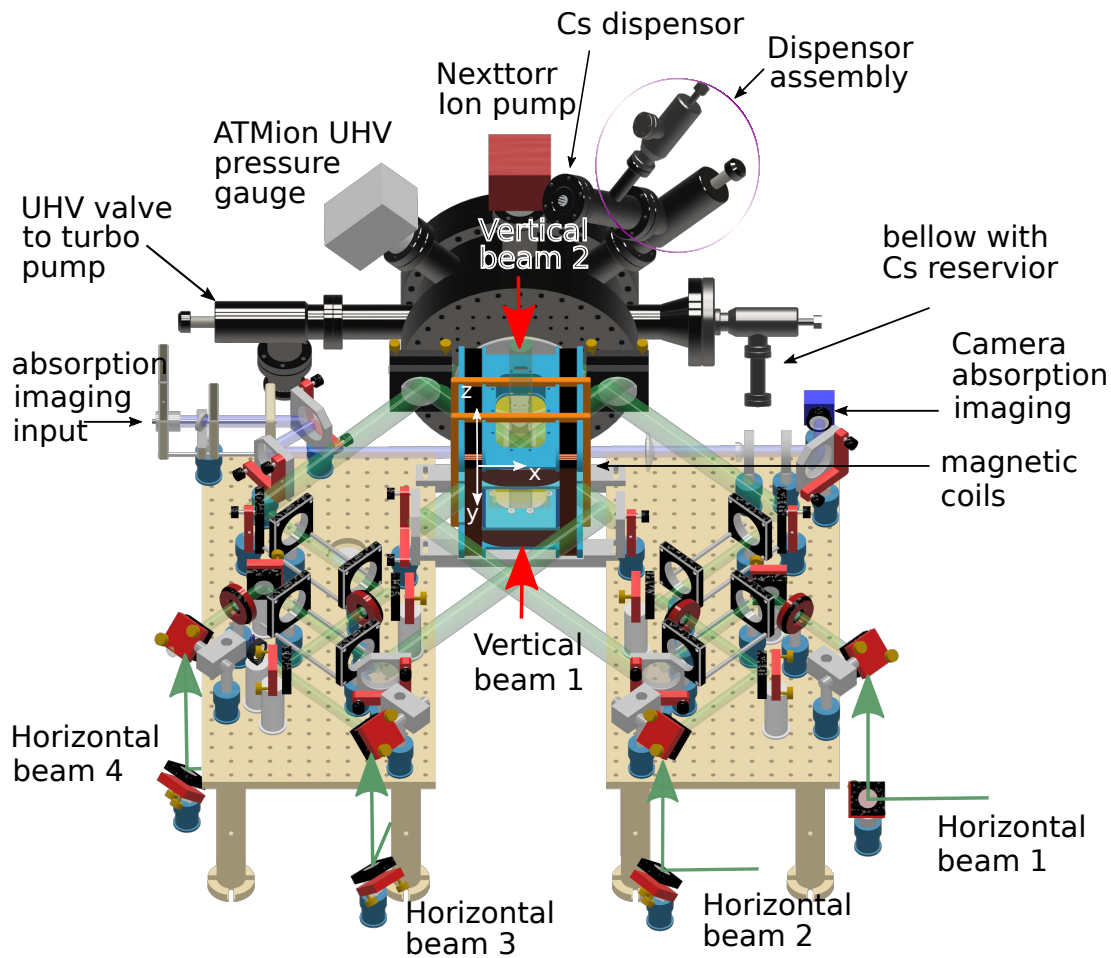


Figure 3.7: 3D view of the MOT setup. The green color beams in the horizontal plane ( $x$ - $z$ ) plus the two vertical beams above and below the glass cell constitute the MOT cooling beams. Components such as vacuum chamber, UHV gauge and pump, magnetic coil assembly, optical field distribution, and absorption imaging setup are shown as well. The nanofiber is at the centre of the magnetic coils with its axis parallel to  $z$ -axis.

when the photons emitted during the detection process in the avalanche photodiode from one of the SPCMs manages to reach the other SPCM. We get a base background SPCM count rate of  $< 200$  Hz per detector and a total detection efficiency of  $\sim 22\%$  with two SPCMs including the quantum efficiency of the SPCMs at this wavelength ( $\sim 55\%$  for each).

### 3.2.3 Magneto-optical trap

For our long term goal of having an efficient quantum memory, an important requirement for us is to trap a large number of nanofiber-coupled atoms. In particular, we trap atoms along a 1D optical lattice potential. Loading this trap with a 3D MOT which is isotropic in three directions may not be the optimum way. In addition, we would like to have a high filling factor and uniform occupancy of the trapping sites along the nanofiber waist. It turns out that appropriately designed magnetic coils can help greatly for our requirements. The details of the magnetic coil setup is described in the following section. After that I describe the optical setup for performing laser cooling. In the end, I also outline briefly the absorption-imaging setup used for characterizing the MOT cloud.

#### 3.2.3.1 Magnetic coil design

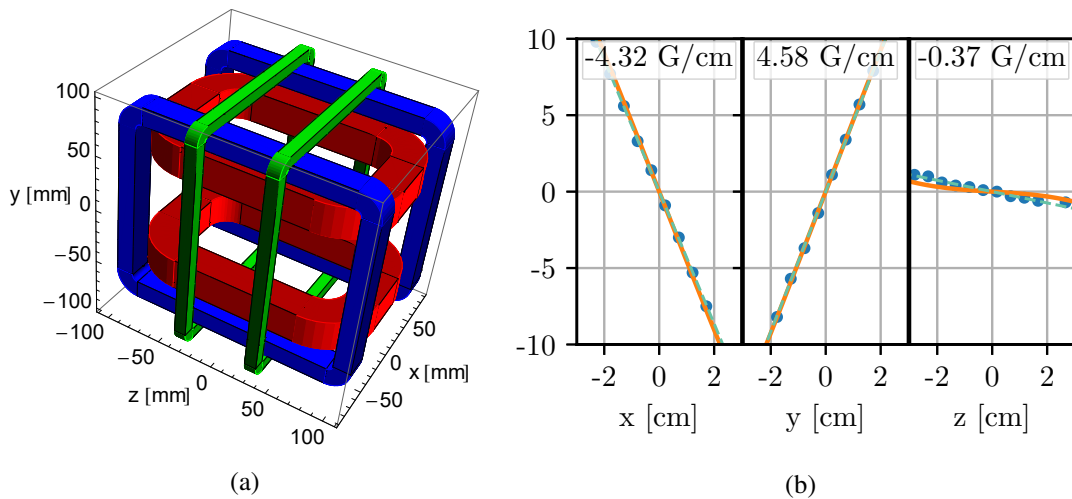


Figure 3.8: Magnetic coil assembly for a “cigar-shaped” MOT. (a) Three pairs of racetrack shaped magnetic coils for implementing magnetic confinement in a MOT. The red coil shows the main quadrupole field coil, whereas the blue and green coils are used for creating additional gradients. The nanofiber axis coincides with  $z$ -axis with  $x = y = 0$ . (b) The total magnetic field in Gauss as measured at different positions along the  $x$ -,  $y$ - and  $z$ -axis at the centre of the coil assembly. The blue dots represent measured data, orange is the RADIA simulation and dashed green line is a straight line fit in the region  $[-2.5, 2.5]$  cm from which we infer the measured magnetic field gradient.

To obtain a high OD from the 1D array of Cs atoms trapped around the nanofiber, one requires efficient loading of the trap sites and large overlap of the cold atom cloud from the MOT and the waist of the nanofiber. As mentioned before, a good choice for the shape of the MOT cloud in this case is that of a “cigar”. It has been shown [78] that magnetic coils are important for implementing such anisotropic (in two dimensions) cloud shapes. To understand



intuitively how such a coil assembly helps, we need to look at the expression for the force on the atoms (say along  $x$ ) in a MOT cloud, which is given as [79]

$$F_{MOT}(x) = -\alpha v_x - \beta x \quad (3.2)$$

where  $\alpha$  is a constant dependent on the atomic mass and transition frequency of the two-level scheme which is used for Doppler cooling and  $\beta \propto \partial|\vec{B}|/\partial x$  is the restoring spring coefficient which arises from the magnetic field gradient. The higher the gradient in a given direction, the tighter is the confinement. Therefore, for a cigar shape confinement, we want a larger gradient in the transverse direction (perpendicular to the nanofiber axis) and smaller gradient in the longitudinal direction (along the nanofiber waist). Other requirements for the magnetic coils is a wide tunability of the generated magnetic fields and field gradient, flexibility of using a pair of coils in Helmholtz or anti-Helmholtz configuration, and a fast switching time.

To meet our requirements, I designed a compact, widely tunable magnetic coils that can be placed close to the trapped atoms. The simulations were done in Mathematica using an open source finite element computation package called RADIA<sup>4</sup> where one can calculate numerically the magnetic fields and gradient distribution corresponding to any arbitrary coil configuration. The parameters for design are specified below in Table 3.1. The assembly contained 3 pairs of racetrack-shaped coils (see Fig 3.8(a)), each of which could be operated in either Helmholtz/anti-Helmholtz configuration. Together, the coils can generate uniform magnetic fields of up to 100 G and magnetic field gradients of up to 20 G/cm at the position of the nanofiber. The high magnetic fields allows us to reach the non-linear regime of Zeeman splitting ( $B \gtrsim 10$  G), if needed. The gradients from the simulated coil assembly was verified with measurements from the actual coil assembly as shown in Fig 3.8(b). One can see that the magnetic field gradient in the  $x$ - $y$  plane is around a factor 12 larger than that along the  $z$ -axis, which gives the cold atomic cloud a cigar-like shape (see Figure 3.10 for the shape and extent). The current used for comparing the simulation and measurement was 1 A in each coil. The wires in the coils are capable of carrying several Amperes which allows for a wide tunability of the magnetic field. The current in each coil can be flipped, allows for reversing the direction of the magnetic field. This in combination with series connection between coils of a pair can generate uniform or quadrupole magnetic field at the nanofiber. The compactness of the coils allowed for smaller inductive load and, hence faster fall and rise times. In our case, the  $1/e$  time for decay of the magnetic field due to the main quadrupole coil pair (red) was observed to be  $\sim 10$  ms. The supporting frame for the coil was designed by a co-student. The current supply used for driving the coils was from Delta-elektronika, model number ES030-10 (0 – 30 V, 0 – 10 A) or ES015-10 (0 – 15 V, 0 – 10 A). The output current from the coil drivers were controlled via analog input voltages.

For making finer adjustments to the magnetic field we added an additional pair of compensation coils for each pair of main coils. They were made by winding a few turns of a thick insulated wire around the parent coils. Each such pair of compensation coils was calibrated according to the procedure discussed in section 3.2.3.5.

<sup>4</sup><http://www.esrf.eu/Accelerators/Groups/InsertionDevices/Software/Radia>

### 3. IMPLEMENTATION OF NANOFIBER-BASED LIGHT-MATTER INTERFACE

Coil pair from Fig. 3.8(a)	centre separation	#wires in the cross-section	wire diameter	resistance/length $\times$ length	typical operating current
Red	107 mm	$15 \times 15$	1.8 mm	$8.2\Omega \text{ km}^{-1} \times 350 \text{ m} = 2.69 \Omega$	2 A
Blue	121 mm	$10 \times 14$	1.5 mm	$10.5\Omega \text{ km}^{-1} \times 170 \text{ m} = 1.8 \Omega$	1 A
Green	65 mm	$10 \times 10$	1.0 mm	$24\Omega \text{ km}^{-1} \times 160 \text{ m} = 3.8 \Omega$	$\sim 100 \text{ mA}$

Table 3.1: Parameters of the three racetrack shaped coil pairs simulated using Radia. The width and thickness of the racetrack shaped coil can be obtained by knowing the diameter and number of turns of the wires along each direction. The wires used were made of copper and insulated.

#### 3.2.3.2 Optics for laser cooling

The optical setup for distributing the cooler beams in the MOT setup is shown in Figure 3.7 and Figure 3.9. The cooler beam is distributed into six beams each having equal power. Four of these beams are in a horizontal plane, intersecting the nanofiber waist at roughly 45 degrees. The remaining two are vertical counterpropagating beams. All beams intersect each other at a point coinciding with the centre of the nanofiber waist. All counterpropagating beams have circular polarization such that the atoms experience orthogonally polarized optical fields from the beams constituting the counterpropagating pair. The intensity of the beams is chosen to be close to the saturation intensity for the Cesium atoms at rest in free space. The beams are expanded and collimated in two stages using appropriate telescopes to have a final beam diameter of around one inch. In this way we increase the volume in which the atoms are laser cooled.

We first laser cool the Cs atoms via Doppler cooling in a magneto-optical trap. For this we use a cooler beam which is roughly 15 MHz red-detuned from the  $6S_{1/2}, F = 4$  to  $6P_{3/2}, F' = 5$  cycling transition. The intensity of the beams corresponds roughly to an on-resonance saturation parameter of one. At times, with a very low probability, the cooling beams excite a detuned transition  $6S_{1/2}, F = 4$  to  $6P_{3/2}, F' = 4$ , and pumps the atom into the ground state  $6S_{1/2}, F = 3$ , which is a dark state for the cooler beam. To sustain further laser cooling of the atoms in the dark state, we need to bring them back to the other ground state. For this we require an additional field, which repumps the atoms in dark state back to the  $6S_{1/2}, F = 4$  ground state. To this end, we use a *repumper* field which excites transition  $6S_{1/2}, F = 3$  to  $6P_{1/2}, F' = 4$  on the D1 line of Cs, thereby shifting the population back to the  $6S_{1/2}, F = 4$  ground state. The excitation into the dark state is unlikely because the cooler is far-detuned from  $F' = 4$  hyperfine manifold. This means that the transfer into the dark state is much slower than the scattering from the cycling transition. Therefore, the power required for the repumper is not as high as that of the cooler beam. We use has a few milliwatts of power for the repumper. The repumper is spatially mode-matched with the cooler beams.

The MOT cooling is followed by a Molasses cooling. The repumper field intensity remains the same as in the MOT phase. The cooler is further red-detuned from the cycling transition

yielding the total detuning around  $60 \text{ MHz} \approx 12\Gamma$ . Both the lasers are derived from Toptica tapered amplifiers (TA pro). The optical power of the cooler and repumper is controlled using an acousto optic modulator (AOM) in a double pass configuration [80]. The power (of the RF signal, up to 2 W) sent to the AOMs is controlled by a programmable RF synthesizer from Moglabs which, in turn, is controlled by the ADwin based experiment control.

### 3.2.3.3 Alignment of optical fields

The first step of MOT alignment is the mode-matching of the counter propagating beam pair. Using irises after the beam expanding telescopes shown in Figure 3.9, we clip the beams into smaller-diameter beams. As a second step, we raise the dispenser current so as to have a high Cs vapor pressure inside the chamber and set the cooler beam to be on resonance for the duration of alignment. After this step, the path of the cooler beams inside the optical chamber fluoresces due to scattering of light from the background Cs atoms. This allows one to align the beams with respect to the nanofiber waist using the CCD camera in the vertical and horizontal direction (top left and right insets in Figure 3.9)).

First, we make sure that the counterpropagating beams in the horizontal plane are mode-matched such that the intersection is roughly overlapping with the nanofiber axis. The top left inset in Figure 3.9 shows the view from the vertical direction after alignment. Next, we make sure that one of the vertical beams passes perfectly well through this crossing. This appears as the bright circular spot in the left inset. To make sure that the fiber is centred with respect to this beam, we maximize the light scattered from the fiber surface using the horizontal camera (top right inset). Once this is done, we modematch the second vertical beam to the first one. At the end of the procedure, we get a MOT.

The next step is to balance the radiation pressure from counterpropagating beams. There could be two reasons for uneven radiation pressure - unequal power or residual non-orthogonality in polarization of the counterpropagating beam pair [79]. To solve this, we run a Molasses optimization procedure as follows. First, we must ensure that the opposite beams have roughly orthogonal polarizations and similar intensities. We use a free space polarimeter for adjusting the polarization. To balance the power, we measure the powers of each beam in a pair and make sure that they are equal. After this is done, we check for any residual mismatch of polarizations. We run a sequence, where we ramp the quadrupole gradient from a high to low value with a frequency of 2 Hz. If the radiation pressure is not balanced, the position of the MOT cloud changes (observed via a camera) as the quadrupole field is ramped down. At low magnetic field gradient, the position is dominated by radiation pressure. To balance it, we adjust the polarization of the counterpropagating beams such that the shift is minimized and the cloud is almost stationary when going from high to low quadrupole field.

### 3.2.3.4 Absorption imaging

Absorption imaging is a well-known technique [81] for obtaining the temperature of the atomic cloud based on expansion rate of the cloud. The schematics of our optical setup for absorption imaging is shown in Figure 3.10(left). A resonant light beam is sent through a cold cloud of Cs atoms. The atoms absorb the resonant light field and scatter it out of the cloud in all direc-

### 3. IMPLEMENTATION OF NANOFIBER-BASED LIGHT-MATTER INTERFACE

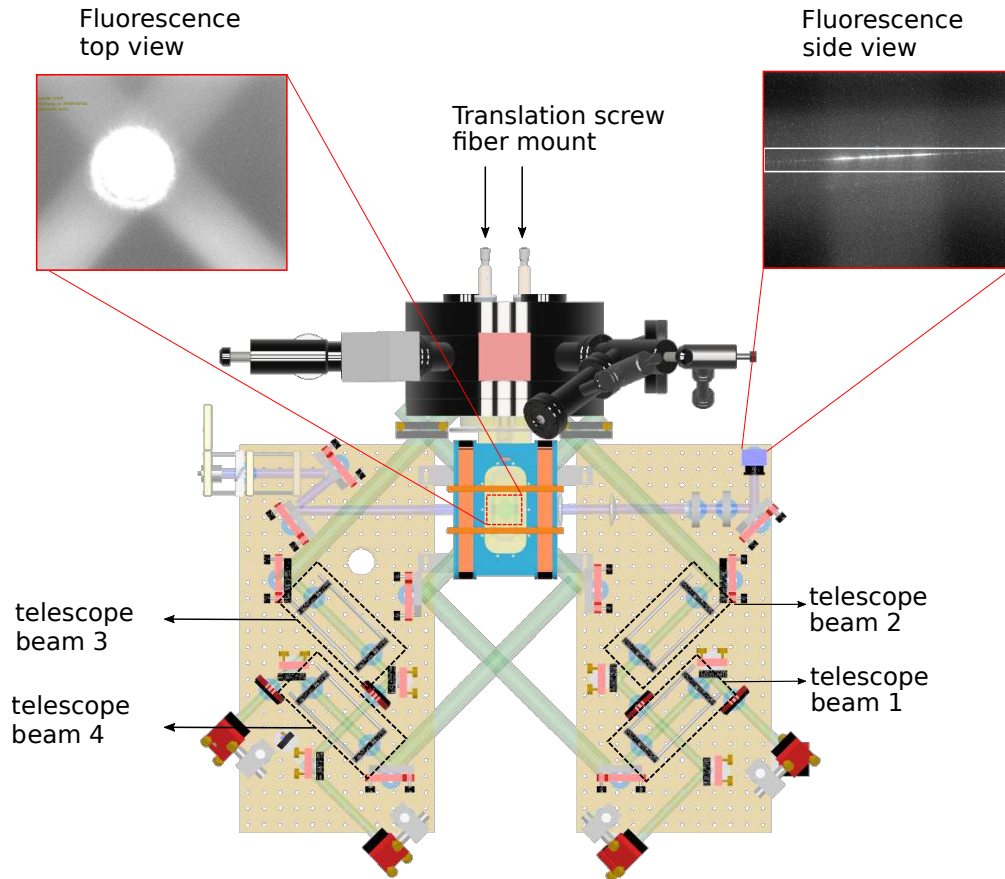


Figure 3.9: (bottom) MOT setup as seen from the top. The green paths indicate the beam path for four horizontal beams. The blue beam indicates the path of the resonant probing beam for absorption imaging (see section 3.2.3.4 for more details). The four beam expanding telescopes are marked. (inset, top left) Fluorescence induced by the MOT beams from the background Cs atoms as seen from the top. The horizontal beams intersect at a point overlapping with the vertical beam. The bright spot in the centre is from one of the vertical beam. (inset, top right) Fluorescence due to resonant cooling light scattering from the background Cs atoms as seen from the side camera (the absorption imaging beam is off). The nanofiber waist (between the two white lines) is illuminated more where it overlaps with the vertical MOT beams. This view allows us to centre the vertical beam with respect to the nanofiber waist.

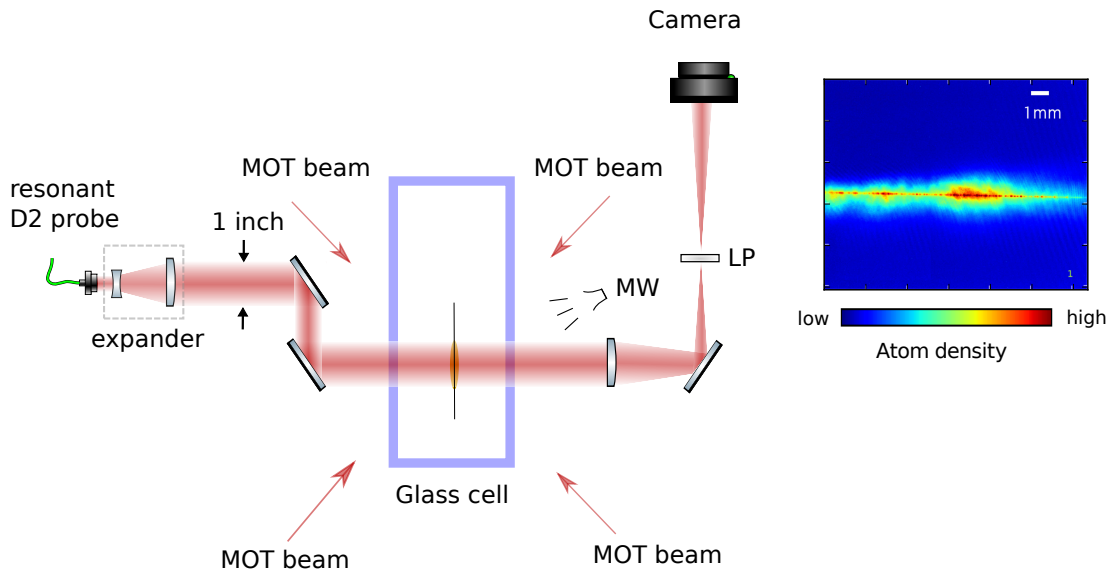


Figure 3.10: (left) Setup for absorption imaging, (right) an absorption image of the cold atomic cloud after the molasses cooling. Blue region corresponds to no atoms and red corresponds to maximum atomic density. The fiber image which was taken separately is superimposed with the image of the cloud.

tions. The transmitted light field is attenuated proportional to the number of atoms along the direction of propagation. This attenuation can be measured as the optical depth which is defined as:  $-\ln[T]$ , where  $T$  is the transmission. Since the transmitted light is imaged on a camera, we are able to convert transmission per pixel into effective OD per pixel. The array of pixels in the camera sensor resolve the image spatially. One pixel corresponds to light propagating through a column with cross-section of dimension  $15 \mu\text{m} \times 15 \mu\text{m}$ . The transmission in every pixel is related to the number of atoms ( $n_i$ ), in the spatial mode of the light defined by the  $i^{\text{th}}$  pixel [82] as:  $T = e^{-n_i\sigma_0}$ , where  $\sigma_0$  is the on-resonance scattering cross-section. Therefore, dividing the OD for each pixel via the on-resonance scattering cross-section ( $\sigma_0$ ) for a single Cs atom yields the number of atoms that were present in column. Integrating this value over pixels gives us the total number of atoms that the beam encountered. More details about the implementation of absorption imaging and temperature measurement using it can be found in Reference [75,83].

Figure 3.10(right) shows one such an absorption image for an optimized MOT cloud. The nanofiber waist image was acquired separately and superimposed with the absorption image for the sake of illustrating the fiber position with respect to the cloud of cold Cs atoms. We have two absorption imaging setups through which we are able to see the cloud from two perpendicular directions, normal to the fiber axis. Using absorption images from the two cameras, we can also align the atomic cloud with respect to the the nanofiber waist. The design and construction of the absorption imaging setup was done in conjunction with a master student [83].

## 3.2.3.5 B field calibration: Microwave spectroscopy

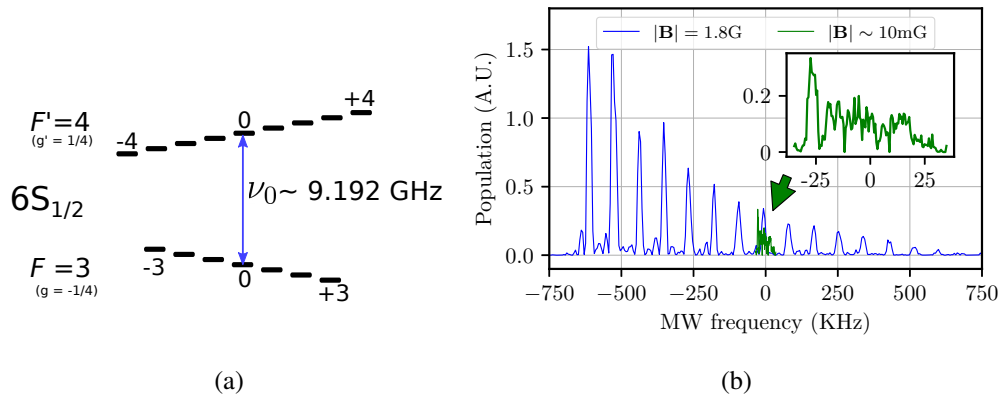


Figure 3.11: (a) Level scheme of Cs  $6S_{1/2}$  hyperfine manifold in the presence of a magnetic field.  $\nu_0$  denotes the so called clock transition in Cs [59] (b) The blue curve corresponds to a MW spectrum for a free space cold Cs atom cloud in a magnetic field of roughly 1.8 G. Each peak corresponds to a transition between the Zeeman manifolds of the hyperfine ground states. The zero on the  $x$ -axis corresponds to the clock transition indicated by  $\nu_0$  [59] in (a). The green curve in the inset of (b) corresponds to a MW spectrum with background limited magnetic field  $\sim 10$  mG achieved after zeroing the magnetic field using the calibrated magnetic field coils. (see the text for details)

**Principle of MW spectroscopy:** The hyperfine levels corresponding to the  $6S_{1/2}$ ,  $F = \{3, 4\}$  ground state of Cs show a Zeeman splitting in the presence of a magnetic field as shown in Figure 3.11(a). Using a MW source, one can transfer atoms from one Zeeman level  $m_F$  in the  $F = 3$  state to  $m'_F$  in the  $F' = 4$  ground state. Large coherence times of the ground state [38] allow one to use MW to perform quantum state generation or manipulation in the ground state Zeeman manifolds of Cs atoms. To be able to perform this, one needs a MW source which can address the Cs atoms near the energy separation of the hyperfine levels in the ground state which is  $\nu_0 \sim 9.2$  GHz. In addition, one needs to calibrate the magnetic fields to be able to achieve a control over the Zeeman-splitting. In particular, a separate calibration of magnetic field for each coil is necessary, to have full control over the field direction and strength. In this section, I will describe our MW setup, the procedure for calibration of the magnetic field and show some sample MW spectra for non-zero and background limited magnetic field.

**Source:** We developed a microwave (MW) setup in conjunction with a bachelor student who assembled and tested the electronics. It involves generating a 2.3 GHz signal by a vector signal generator (Keysight technologies), frequency doubling it twice and then sending it, after amplification, to a MW antenna placed close to the trapped atoms. This frequency is chosen to match the ground state splitting of Cesium atoms in zero magnetic field which is  $\sim 9.2$  GHz. Such a MW source offers a convenient tool to probe and manipulate Cs atoms in the electronic ground state,  $6S_{1/2}$ . We used this tool to zero down the magnetic field at the centre of the MOT cloud

and in-situ calibrate the magnetic field coils discussed in section 3.2.3.1.

**Experimental sequence for measuring a MW spectrum:** We laser cool the Cs atoms with a MOT and molasses phase. Next, we optically pump all the atoms from  $6S_{1/2}, F = 4$  to  $6S_{1/2}, F = 3$  which is achieved by turning the repumper off while leaving the cooler beam on. After the optical pumping step, the magnetic field coils are then turned on and allowed to stabilize ( $\sim 10$  ms). Then we send a short ( $\sim \mu\text{s}$ ) weak MW pulse at a frequency  $\nu$  such that when resonant with any of the allowed transitions, some of the atomic population is transferred from the relevant Zeeman levels from the  $6S_{1/2}, F = 3$  to the  $6S_{1/2}, F = 4$  state. We then measure the population of the atoms in the  $6S_{1/2}, F = 4$  state by means of absorption imaging of the cold atoms. By scanning the MW frequency and measuring the population via absorption imaging, one can obtain a MW spectrum as shown as a blue line in Figure 3.11(b).

**Calibrating magnetic fields:** The frequency for a transition between  $\{F = 3, m_F\}$  to  $\{F' = 4, m_{F'}\}$  in presence of magnetic field  $\vec{B}$  is linearly<sup>5</sup> proportional to the strength of the field as :

$$\nu_{m_F \rightarrow m_{F'}} = \nu_0 + \mu_B |\vec{B}| (g_{F'} m_{F'} - g_F m_F) / h \quad (3.3)$$

where  $\mu_B$  is a constant (Bohr-magneton),  $g_F$  and  $g_{F'}$  are the Landé-g factor for the two hyperfine levels constituting the transition and  $m_F - m_{F'} = \{0, \pm 1\}$ . For the transitions considered here,  $g_F = -g_{F'} = 1/4$ . Therefore, there are 15 distinct values of  $\nu$ , hence, 15 different peaks in the MW spectrum for the transitions allowed by the selection rules. The frequency separation between peaks in the MW spectrum thus gives us the value of the magnetic field. We choose the duration of the pulses appropriately such that we are able to resolve all the peaks independently. The width of the peak corresponding to each transition is ideally Fourier limited due to the finite pulse duration of the MW field. There could be dephasing/decay of the transition or spurious magnetic field gradients that can further broaden the peak [84]. To obtain the calibration curve for a given coil, we vary the voltage applied to it. This translates to changing the current flowing through the coil. For each voltage setting, we obtain the MW spectrum and find the splitting between two peaks (say the pair of transitions with two lowest frequency,  $\nu_1$  and  $\nu_2$ ). This peak separation ( $\Delta\nu = \nu_1 - \nu_2$ ) as a function of the  $|\vec{B}|$  voltage applied to the coil gives us the required calibration.

**Zeroing magnetic fields:** The higher the magnetic field, the greater is the distance between the individual peaks and the wider is the resulting MW spectrum. To reduce the net magnetic field to zero at the position of the atoms, we therefore supply the coils with voltage corresponding to the minimum splitting, as was obtained from the calibration. We make this separation extremely small such that the separation between the outermost peaks is limited by the background magnetic field fluctuations (see green plot see Figure 3.11(inset)). In our case, the total MW spectrum spread at lowest magnetic field is  $< 75$  kHz as can be seen from the inset. From equation 3.3 and values from reference [59], one can find that the separation between the outermost peaks per Gauss of B-field is  $(\nu_{3 \rightarrow 4} - \nu_{-3 \rightarrow -4}) \sim 4.9$  MHz. Therefore, 75 kHz correspond to a residual

<sup>5</sup>for small  $|\vec{B}|$ , the dependence is linear

magnetic field of tens of milligauss which is at least as good as what has also been achieved in other groups [85]. Since we perform this procedure using a free space MOT as opposed to nanofiber trapped atoms, we do not have to be concerned additionally about any fictitious magnetic fields (see section 2.4) that could be present around the nanofiber surface due to the trapping light fields.

#### 3.2.4 Experiment control and data acquisition

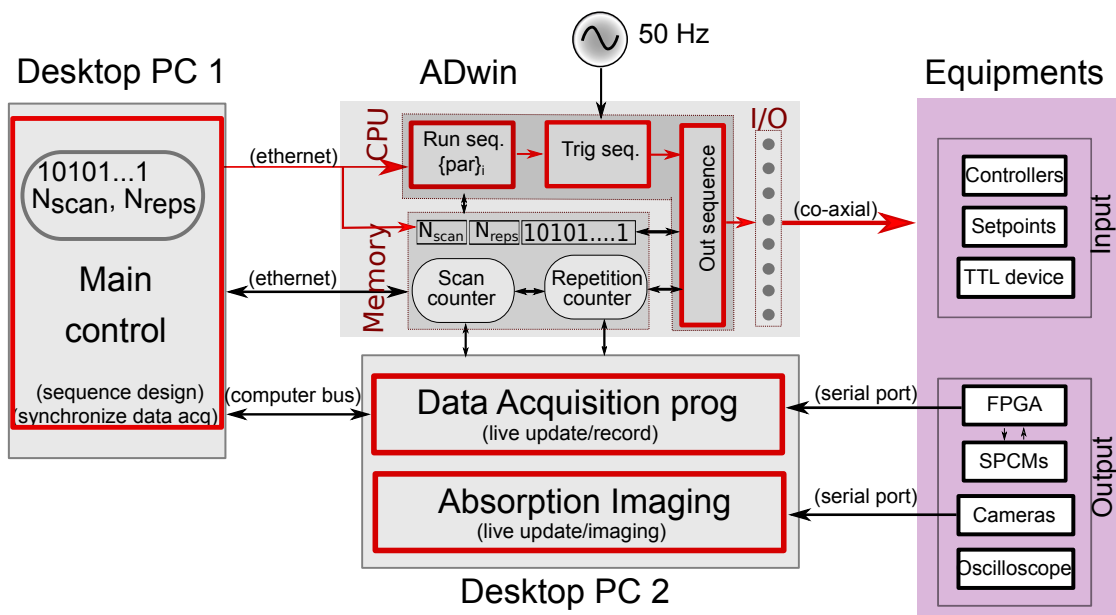


Figure 3.12: Schematic of experimental flow-control where the flow is denoted by red colored one-sided arrow. The red color rectangles represent scripts that run either on the PC, namely, Main control, Data acquisition and absorption imaging or on the ADwin, namely, Run seq., Trig seq., and Out sequence. The ADwin computer is divided into CPU, memory and input-output (I/O) sections. The CPU runs the pre-compiled ADbasic programs. The memory stores the voltage output sequence and other fixed variables used by the CPU programs to track the number of repetitions. The I/O modules send out the analog and digital outputs (32 digital, 24 analog) to the various equipments required for carrying out an experiment with co-axial cables. The scan counter and repetition counter corresponds to accessible memory locations in ADwin CPU which the scripts running on the PCs use for data-synchronization or for the generation of a new output sequence. (more details in section 3.2.4.

#### Adwin-Pro II controller:

To perform our experiments we use various analog and digital devices which rely on analog/digital inputs as their control signals. We generate these signals using an ADwin pro II



computer<sup>6</sup>. The ADwin device consists of three main blocks - central processing unit (CPU) (300 MHz clock rate, 768 kB local memory), read/write memory (256 MB), and input/output (I/O) modules that govern the output of 24 analog outputs, 32 digital channels input/outputs, and 8 analog input channels (we do not use them). The CPU is responsible for interfacing all the components and executing tasks such as controlling the output of the I/O modules. The memory locations store values which can be accessed and edited internally via ADwin or externally by a computer. We use these memory locations to store the output voltages for each channel for the duration of an experimental run, i.e., the experimental sequence, as well as to keep track of how many times a sequence must be executed.

The processes running inside the CPU that execute the experiment sequence is programmed in a high-level programming language called ADBasic. A dedicated compiler converts the AD-basic code to machine level instructions. This pre-compiled object code (a binary file) is loaded onto the ADwin CPU through the PC via an ethernet connection. Each code has three main attributes: a priority number, process delay and an event section. The event section contains the I/O instructions and is executed periodically with the period defined by the variable 'processdelay'. A program terminates only when the event section meets an exit condition. The priority number helps ADwin distribute times to different tasks running in a time-sharing mode. Since we do tasks sequentially, we assign all processes the highest priority. Network communications is assigned a lower priority by default.

#### **Flow of control:**

The experimental control flowchart is shown in Figure 3.12 with the red single sided arrows showing the flow of control. A typical experiment involves scanning a parameter and performing certain number of repetitions for each value of the scan parameter. The PC generates the sequence corresponding to one value of the scan parameter and uploads it along with other parameters such as number of repetitions on to the ADwin memory. Inside the ADwin CPU there are three inter-dependent processes that executes the sequence a desired number of times. The first out of three processes running on the ADwin tracks the number of experimental repetitions. If the desired number of repetitions has not been achieved yet, it triggers the second program which waits for the rising edge of the AC power supply of the lab at 50 Hz). The TTL trigger signal corresponding to the AC supply is generated from a homebuilt device and is supplied to the event-in port of the main processor. Triggering the execution of a single run on the AC power line ensures that the electronic setup is identical for all runs of the experiment. Upon the receipt of the trigger signal, the second program starts the third program which carries out an experimental sequence. The latter involves iterating the event section such that each run sets all output ports to their programmed voltages for that run. Once the event section has gone through all the time steps of the experimental sequence, it increments the internal variable which tracks the number of repetitions and the control goes back to the first program. The process is repeated until a given sequence is run a desired number of times. After that the first program exits. For a given scan parameter (such as an analog output voltage), the PC (main control program) then

<sup>6</sup><https://www.adwin.de/us/produkte/proII.html>

generates a new sequence with a new value of the scan parameter and uploads this sequence to the ADwin memory. This repeats until all the values of the scan parameter are entirely scanned.

#### **Sequence generation and data acquisition:**

The experimental sequence is an array of voltages corresponding to discrete time steps. I wrote a python program where we define the voltage versus time steps for each channel. We then pack the values in a single array which can be transferred onto the ADwin. The array is read sequentially inside ADwin. So we pack the output levels of all 24 analog channels in a row for every timestep and then concatenate all the rows such that the adwin can load 24 values at a time and output it via the I/O modules and then move to the adjacent block in the array. All the voltage values are 12 bit binary numbers corresponding to the 12 bit resolution of the digital-to-analog converters that output the signal. The digital values are packed as a single array where each element is a 32 bit binary number containing the status (0 or 1) of each digital channel.

The minimum duration of a time bin is defined by the settling time of the A/D converters for the analog outputs of ADwin which, in our case, is slightly more than  $1 \mu\text{s}$ . The rise time of the digital signals was measured to be 22 ns. The output from the ADwin I/O modules are sent to the various controllers and devices that change the experiment conditions depending upon the analog or digital signals provided. The output from the experiment is recorded by means of devices such as SPCMs, oscilloscopes, spectrum analyzers, FPGAs and cameras. All of these devices are programmed to store the raw data within them or in the PC. For processing the photon timetags and storing it, we have a tool (python frontend and Visual C++ backend) developed by one of our postdocs. Once we have the time-tags we are able to perform analyses. Devices such as the cameras receive TTL signals from ADwin as a trigger to take images, while our self-developed python scripts acquire and process the image at each shot. The oscilloscopes or digital spectrum analyzers can be programmed manually to save the data in a desired format in a desired location.

### **3.3 Trapping atoms**

In the previous sections, I have described our methods to install a clean nanofiber into an ultra-high vacuum chamber. In addition, I described the procedure to cool Cs atoms using a magneto-optical trap followed by a molasses cooling. I will now discuss how we load cold atoms from the MOT cloud into the optical dipole trap lattice in the evanescent field of the nanofiber as was discussed theoretically in the previous chapter.

#### **3.3.1 Experimental sequence for trapping atoms**

A typical experimental sequence that we use for characterizing the optical depth of the trapped atomic ensemble is shown in Figure 3.13. The different phases of such an experiment is indicated at the top, namely, MOT, molasses, waiting time, probing with atoms, push out and probing without atoms. The values 'set' and '0' on the  $y$ -axis correspond to the optimum set point and off position of the channel. In the MOT phase, the cooler and quadrupole magnetic fields are

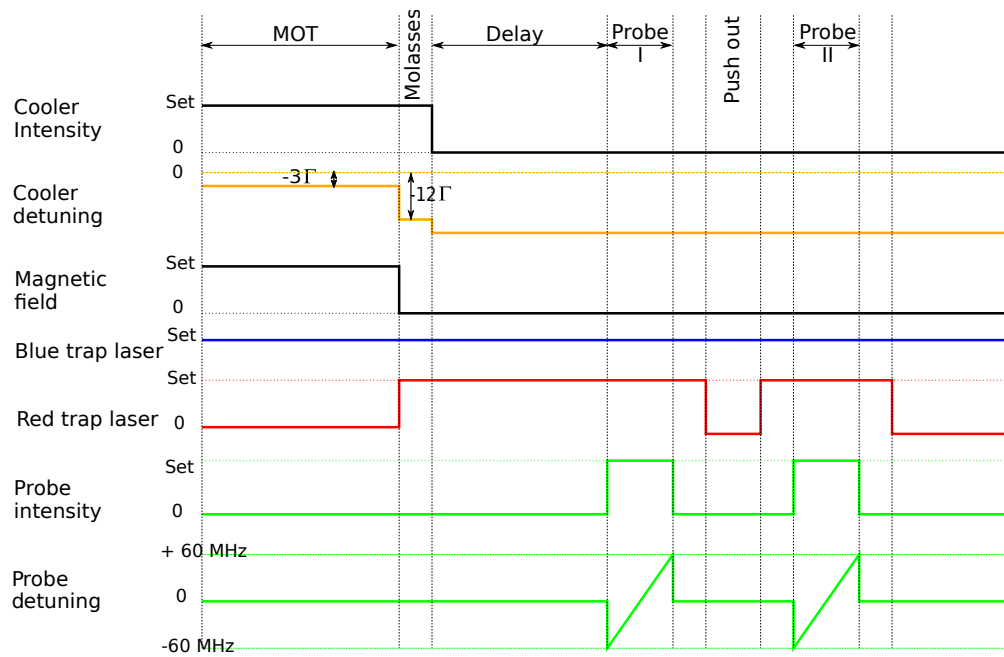


Figure 3.13: A typical experimental sequence to measure the optical depth of the trapped atomic ensemble. 0 and Set on the  $y$ -axis correspond to the channels being off and set to a certain level. Other details are self-explanatory. More description in section 3.3.1

on, which leads to Doppler cooling of the atoms. In the molasses phase, the magnetic fields are switched off, and the red-detuning of the cooling beam is increased. At the same time, the red-detuned trap laser field is turned on. We keep the blue-detuned trap laser always on. Due to the sisyphus cooling in the molasses phase the atoms lose kinetic energy. As some of these atoms move through the optical dipole trapping potential created due to the trapping fields, it gets trapped due to lack of sufficient kinetic energy to escape the potential barrier created by the trapping fields. Due to the collision blockade effect, every trapping site can have at most one trapped atom. After the trapping sites are loaded with atoms, the molasses cooling is turned off. One can probe the trapped atoms that remain after a certain delay. Usually, it is of interest to quantify the number of atoms by measuring the optical depth which we discuss in the following section.

### 3.3.2 Measurement of optical depth

The on-resonance optical depth is a measurement of the attenuation of a resonant light-field when propagating through an ensemble of emitters. The emitters tend to scattered light out from the propagating mode thereby effectively attenuating the light field. Due to the linear nature of this dissipation, the optical depth is related to the transmission at resonance as  $OD = -\ln T$ . To measure the optical depth from a trapped atomic ensemble, we first trap the atoms using the sequence described above and shown in Figure 3.13. The OD measurement procedure is de-

scribed below.

We send an optical probing pulse at wavelength of 852 nm. We use a probe field with a small on-resonance saturation parameter,  $s_0 \ll 1$ , for a duration of around a millisecond. During the pulse duration, we scan uniformly the detuning  $\delta$  of the probe beam with respect to the Cs D2 transition ( $F = 4 \rightarrow F' = 5$ ) by using an acousto-optic modulator and record output photon counts in the presence of atoms ( $C_{\text{atoms}}$ ) (orange solid line in Figure 3.14). After the scan is completed, the red-detuned trap laser is switched off such that the atoms are lost from the trapping sites. After some amount of waiting, we turn on the red-detuned trap laser again, and record the transmitted photon count ( $C_{\text{without atoms}}$ ) without atoms (blue solid line in Figure 3.14). After that, the red-detuned trap laser is turned off and the background-counts ( $C_{\text{bkg}}$ ) is recorded. These counts comprise room light contamination and the SPCM dark counts. We repeat the whole measurement  $N$  times to get  $1/\sqrt{N}$  reduction in the photon number noise assuming no technical noise. From the average value of these three counts, we are able to extract the on-resonance optical depth (OD) as:

$$T(\delta) = \frac{\bar{C}_{\text{atoms}}(\delta) - \bar{C}_{\text{bkg}}}{\bar{C}_{\text{without atoms}}(\delta) - \bar{C}_{\text{bkg}}} = e^{-\text{OD}/(1+4(\delta-\delta_0)^2/\Gamma^2)} \quad (3.4)$$

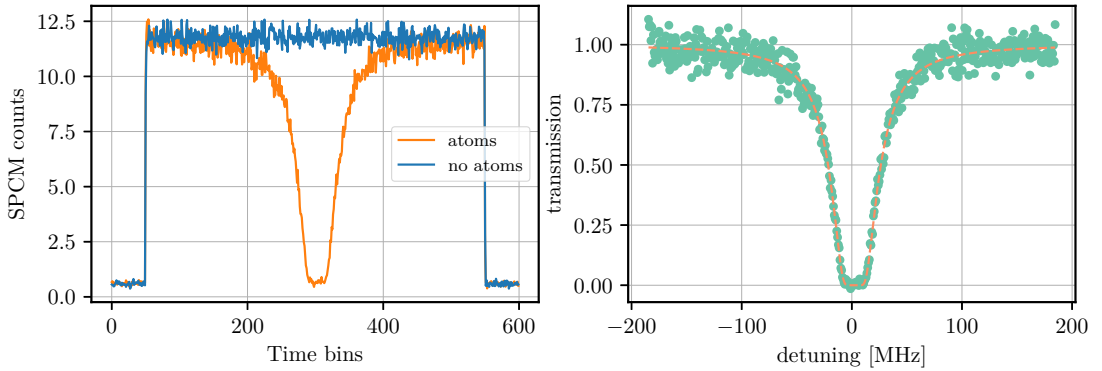


Figure 3.14: Example optical depth measurement using an absorption trace with (left) and without atoms (right). The transmission obtained from left figure is shown in green and the fit using equation 3.4 is shown in dashed orange. The bin size used is  $10 \mu\text{s}$ . The measured OD determined from the fit is  $59 \pm 1$  and the light-shift of the resonance is  $\delta_0 = 2.4 \pm 0.16 \text{ MHz}$ .

where the bar over the counts represents averaging over  $N$  runs of the experiment,  $\Gamma$  is the atomic linewidth, OD represents the on-resonance optical depth where resonance is defined with respect to a light-shifted transition, shift being  $\delta_0$ . The expression in the exponential takes into account the Lorentzian lineshape of a transmission profile [79]. The above expression is also called the Beer-lambert's law. Figure 3.14 dashed orange line shows the fit to a transmission profile corresponding to the above expression.

So far, we have ignored any heating of the atoms and the fact that the probe field can apply a force on the atom when it is detuned. For probe scan durations comparable to the lifetime of the trapped ensemble, the OD can change over the duration of probing due to the heating of the atoms, therefore potentially, giving an erroneous estimate of the optical depth. To overcome this, we measure the average transmission of the ensemble for a probe pulse with fixed detuning, and duration much smaller than the lifetime of the trapped atoms. We measure the average transmission for each value of the the detuning to obtain the full transmission profile for the atomic ensemble.

Measurement of OD from the transmission spectrum can be difficult for large atomic ensembles. At very high ODs, the transmission around resonance gets limited by the background photon counts. Therefore, one needs to scan a very large frequency range, and the resulting curve incorporates multiple optical transitions. Alternatively, one can measure transmission curves after longer waiting times (delay phase) of atom storage in the nanofiber based trap and then extrapolate the OD for shorter waiting times as shown in section 3.3.6).

### 3.3.3 Estimation of the number of atoms

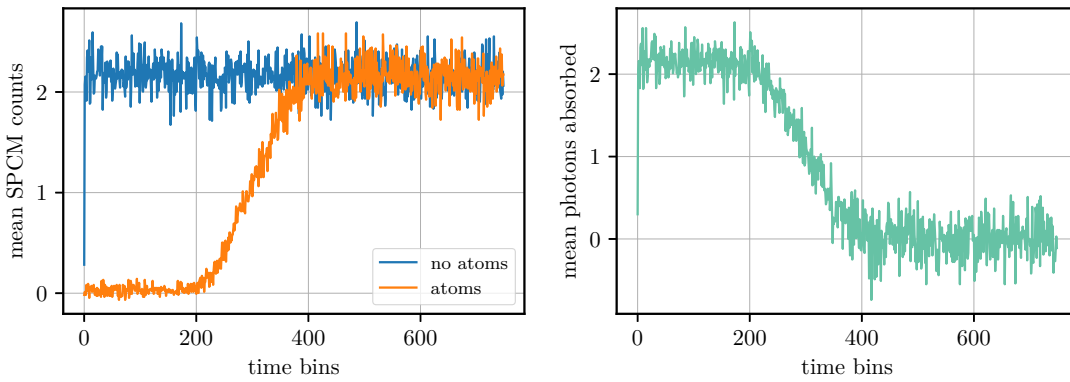


Figure 3.15: Atom number measurement by means of optical depumping with the probing field on the Cs D2 transition  $F = 4 \rightarrow F' = 4$ . (left) The transmitted photon count trace with and without atoms. (right) The absorption trace for the trapped atoms. The bin size is  $2 \mu\text{s}$ . In this case, the number of trapped atoms was estimated to be  $885 \pm 8$  atoms (more details see section 3.3.3).

We use the technique of optical depumping suggested in Reference [86] where we infer the atom number from the number of photons required to pump the entire ensemble to a dark state. We send a pumping light field at the transition  $6S_{1/2}, F = 4$  to  $6P_{3/2}, F' = 4$ . Upon absorbing a photon, the excited state has the possibility of decaying to either the ground state  $6S_{1/2}, F = 4$  or  $6S_{1/2}, F = 3$ . The spontaneous emission branching ratio for these two transitions is  $\Gamma_{F'=4 \rightarrow F=4} / \Gamma_{F'=4 \rightarrow F=3} = 7/5$ , which means that, on an average, an atom will scatter 2.4 photons before it decays to the  $F = 3$  dark state. Therefore, by counting the number

of photons needed to pump all the trapped atoms to the dark state, one can estimate the number of atoms. Figure 3.15 (right) shows a typical absorption trace (averaged over 100 runs) as a function of probing time for an ensemble of trapped atoms. This trace is calculated from the difference of the transmitted trace with (orange) and without atoms (blue) as shown in the Figure 3.15 (left). One limitation of the technique arises when the lifetime of the trapped atoms is low. In this case, the depumping probe pulse (with atoms) is very shortly after the molasses phase (see experimental sequence template in section 3.3.1 where the frequency scanned probing pulse will be replaced with a fixed frequency depumping pulse). This leads to absorption of the fiber-guided probe beam by the MOT atoms which could still be around the fiber. If unaccounted, this leads to over estimation of the number of trapped atoms. A workaround is to record a reference trace for absorption from MOT atoms and remove this background absorption to obtain a better estimate for the number of nanofiber trapped atoms. Another option is to perform an atom number measurement via saturating the trapped atoms with a resonant probe and infer the number of atoms from the probe power needed to saturate the ensemble [64] (see also section 5.1.3).

### 3.3.4 Optimum trapping configuration

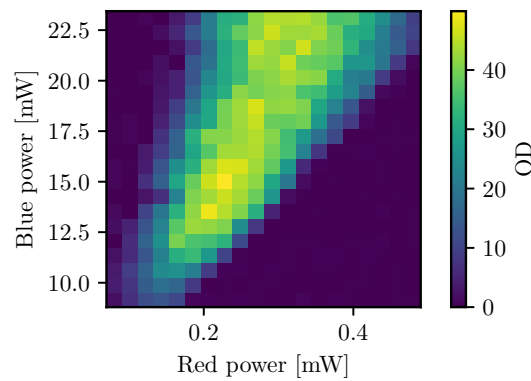


Figure 3.16: An example OD distribution, recorded 30 ms after the molasses phase, for different powers of the blue-detuned and single beam of red-detuned trap lasers. Such a measurement is crucial to finding the optimum trapping configuration for achieving the best optical depth.

This method is important to find out the values of optimum trapping laser powers. This step is usually performed after the step where the fiber overlap with the cold atomic cloud (resulting from MOT and molasses cooling phase) is optimized. At this point, one is usually able to see absorption from the MOT atoms around the fiber even without turning on the trapping fields. To start trapping the atoms, we turn on all the trapping fields during the molasses cooling. To optimize the trapping configuration with respect to a parameter like OD or atom-number, we scan the power of the red-detuned trap laser and blue-detuned trap laser and then measure the value of the parameter at a fixed delay after molasses phase. We then choose a configuration which gives the best value of the parameter being optimized. Figure 3.16 shows an outcome of such an

experiment which optimizes the OD at a time delay of 30 ms from the end of molasses cooling. On the  $x$ - and  $y$ -axis one can see the powers of the red and blue-detuned trap laser, respectively. The color scale indicates the OD of the trapped atomic ensemble. The best configuration here, corresponds not to the maximum blue and red-detuned trap laser powers, but to some intermediate value. One reason for this is that at higher trap laser powers, the fiber gets heated more, leading to larger heating-induced mechanical vibrations in the nanofiber which in turn deforms trap potential such that the atoms can escape from the trap. This effectively reduces the optical depth at high trap-powers.

### 3.3.5 Measuring filling factor

To measure the filling factor we employ a fluorescence measurement as done in [64, 72]. We employ the Andor IXon-897 EMCCD (electron-multiplying charged coupled device) camera from Oxford instruments to collect the fluorescence from the atoms. For measuring the position along the fiber waist, we need a calibrated imaging system. For this purpose, we use the absorption imaging setup (see section 3.2.3.4) and replace the CCD camera with the EMCCD camera, thereby using the calibration (magnification factor) from before. For acquiring the fluorescence image we send a short intense resonant pulse (on-resonance saturation parameter  $\sim 100$  for the first atom) through the fiber and expose the camera for the same duration which is roughly a few  $\mu s$ . After all the atoms are lost because of heating from resonance-fluorescence, we wait for some time and then acquire the background image. We average the signal over 5000 background subtracted fluorescence images to obtain the average signal which is shown in Figure 3.17 (top). We can estimate the number of trapping sites from the fact that we use  $\lambda_{\text{red}} = 1064$  nm laser (for this particular measurement) as the red-detuned trap laser and that we trap atoms in two one-dimensional arrays with a spatial periodicity of  $\lambda_{\text{red}}/2n_{\text{eff}}$ . Knowing the actual spatial distance along the nanofiber waist corresponding to a single pixel size on the camera, we calculate the number of trapping sites per pixel and hence the total number of trapping sites along the waist section imaged by the camera. We measure the atom number via the method outlined in section 3.3.3. For Figure 3.17 this was calculated to be 2500 atoms. We distribute the measured atom number corresponding to each pixel (here  $\sim 2500$ ) according to the normalized fluorescence per pixel along the direction of the fiber axis (the line density, see bottom panel left  $y$ -axis). The ratio of the total number of atoms in a pixel to the number of trapping sites in that pixel gives us the filling factor.

We plot the filling factor along the length of the fiber (Figure 3.17 (bottom, right  $y$ -axis)). In this case, the maximum filling factor achieved was around  $\sim 0.1$ . The line density of atoms is not a flat top profile but is higher on the left. One reason is that the probe field, when propagating from left to right side, has a non-uniform intensity distribution owing to the scattering from the atoms. The intensity decays exponentially with the number of atoms. Therefore, on the right, the atoms scatter less than that on the left. Another reason is overlap of the MOT cloud with the fiber [72]. In the example shown in Figure 3.17, the cloud was compressed by using strong quadrupole magnetic field gradients during the MOT phase. The overlap of the resulting ellipsoidal shaped MOT cloud of atoms with the fiber waist results in a non-uniform loading along the fiber axis.

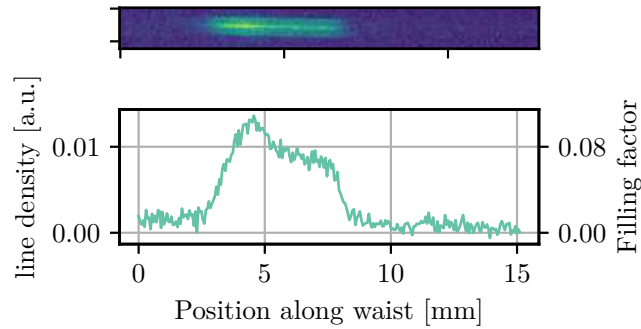


Figure 3.17: Data from a measurement of the filling factor along the fiber. The top plot shows an average of 5000 background subtracted fluorescence images of the fiber-trapped atoms. The bottom panel shows the line density of fluorescence (left) and filling factor per unit length (right) for different positions of the fiber waist.

### 3.3.6 Lifetime of trapped atoms

The atoms trapped around the nanofiber get heated due to several mechanisms [87] and are eventually lost from the trap. It is therefore interesting to measure the total number of atoms trapped, or the corresponding optical depth of the ensemble, at a certain time after the trapping sites were loaded. Since the loss rate is proportional to the number of atoms, the optical depth or atom number decays exponentially with time. We call the  $1/e$  decay time the lifetime of the trapped atomic ensemble. Higher lifetime indicates more stable trapping conditions. Hence, lifetime is one of the most important diagnostic measurements. In addition, for optically dense ensembles, lifetime measurement serve as an alternate way to infer high ODs through extrapolation of the OD decay curve. Fig. 3.18(a) shows OD measured at different time delays ( $\tau$ ) after the trap loading. This particular measurement corresponds to an OD of roughly 1000 at 4 milliseconds after loading the trapping sites. The fit shown by the orange dashed line gives us a trapping lifetime of  $77 \pm 3.6$  ms. I must mention that this is on the of the best OD that we achieved with our system.

We also measured the lifetime of the total number of trapped atoms (for the same conditions of trapping as for figure a) via the optical depumping technique discussed in section 3.3.3. The result is shown in Figure 3.18(b). The  $1/e$  decay lifetime for the number of atoms trapped was  $104 \pm 4$  ms. One important observation which one can make is that the OD decays faster than the atom number. This is because the mean energy of the atoms increases with increasing time delays due to heating. This implies that with increasing time delays, the trapped atoms are on average further away from the fiber surface due to anharmonicity of the radial trapping profile, which leads lower atom-light coupling strength. Since the optical depth is directly proportional (see section 4.3.2) to the atom-light coupling strength and the number of atoms, therefore, it decays faster than atom number.

Achieving such high OD, as shown in Figure 3.18, was realized in several steps. First the optimum trapping configuration was achieved via scanning the trapping powers of the red- and



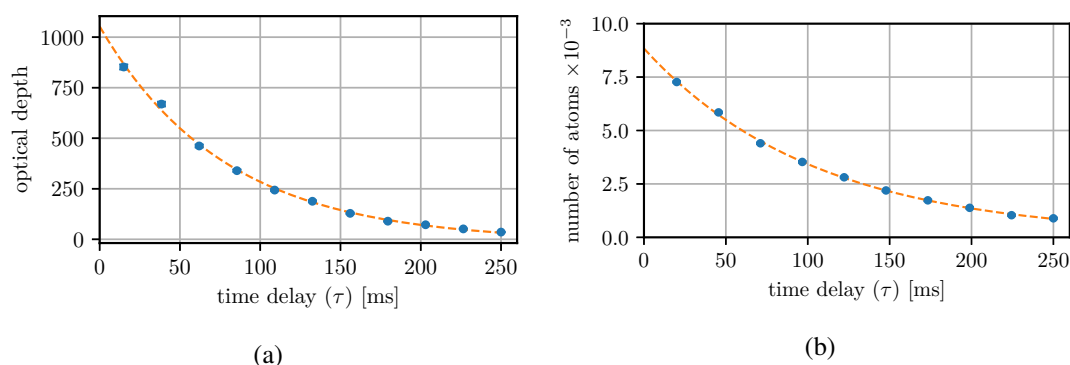


Figure 3.18: (a) On resonance optical depth, (b) total number of trapped atoms, as a function of time delay after loading the trap. The OD is measured from a transmission scan across the Cs D2 line ( $F = 4$  to  $F' = 5$  transition) according to the procedure discussed in section 3.3.2. The atom number is measured by the method discussed in section 3.3.3. Each point corresponds to averaging over 10 shots of the experiment.

blue-detuned dipole trap lasers as discussed in section 3.3.4. Then, we stretched the cloud evenly along the entire nanofiber waist by increasing the ratio of transverse to longitudinal magnetic field gradient. Next, we aligned the fiber waist with the cloud such that the overlap between the two was maximized. The MOT reshaping and nanofiber alignment to the reshaped cloud was done iteratively. The optimization was done by using atom number as the benchmark. In addition, we used a MOT loading time of  $\sim 2$  s to maximize the loading of the trapping sites. As a side note, the above measurement setting lasted for a few days but with gradual decrease in the stability of the system. We speculate the reason for this degradation to be Cs deposition on the fiber surface. However, concrete reasons for the change are unknown.



Die approbierte gedruckte Originalversion dieser Dissertation ist an der TU Wien Bibliothek verfügbar.  
The approved original version of this doctoral thesis is available in print at TU Wien Bibliothek.

# Theory: Correlated Photon transport in nanofibers

## 4.1 Introduction

Photons are inherently noninteracting in nature. However, in the field of quantum information where the information is encoded in photons [24], it is essential that photons interact with each other in order to implement quantum gates [88–90]. An effective photon-photon interaction can be realized by interacting photons with matter such that presence of one photon changes how the medium reacts to the other photon. In recent years, significant advances have been made towards achieving strong interactions between optical photons by employing strong coupling between light and quantum emitters and exploiting the latter's inherent nonlinear response to mediate the interaction [91, 92]. There have been a number of approaches towards this goal using high finesse optical cavities [93–97], strongly interacting Rydberg atoms [98–105] or atoms strongly coupled to waveguides [106–108]. Much effort has gone into enhancing the control and fidelity of photon-photon interactions by increasing light-matter coupling or by reducing dissipation in the system. However, the implementation of strong, low-loss interaction between individual photons remains an elusive goal for many-body systems at optical frequencies.

It turns out that optical nanofiber-based atom-light interfaces are well suited for implementing strong optical nonlinearities using the neutral atoms trapped around the nanofibers. A resonant light field propagating through the nanofiber is confined to dimensions smaller than the wavelength of the light. Most of the energy propagates in the evanescent field of the nanofiber which leads to a better overlap between light and atomic scattering cross-section than achievable in free-space. The atoms trapped in the evanescent field of the nanofiber are able to absorb and scatter out a significant fraction of the propagating light field leading to a large on-resonance optical depth. An atom can absorb only one photon at a time. Due to this nonlinear nature of the atoms, nanofibers-based atom-light interfaces can help facilitate complex many-body interactions between photons. This that can generate correlated states of light that exhibit non-classical

photon statistics. It opens up avenues to study complex quantum many-body physics of photons in out-of-equilibrium systems [109].

In this chapter, I will summarize the relevant theory on photon transport through optical waveguides coupled to one or more quantum emitters. I will start with discussing some of the basic concepts underlying the study of photon statistics in quantum optics. In particular, I will explain when the light field is said to exhibit nonclassical properties, and what is defined as bunched or anti-bunched light based on the time-intensity correlations. After presenting the basic definitions, I will review the basic physics of single photon scattering across quantum emitters coupled to waveguide and calculate the expressions for optical depth exhibited by a single atom coupled to a nanofiber waveguide. Then, I will briefly introduce the scattering matrix formalism which is useful for extending the scattering theory to multiple emitters coupled to a waveguide. Along these lines, I will summarize the recent work [51] of photon transport in waveguides which applies exactly to our experimental system. This theory work done by our collaborators will lay down the basis for the next chapter where I will describe how the corresponding experiment was performed in our lab and discuss how well does the results obtained compare with the theoretical predictions from the current chapter.

## 4.2 Correlation functions

In this section I will introduce basic concepts and definitions from quantum optics theory crucial for the rest of the thesis. Correlation functions are used to study the fluctuations of a stochastic process. In general they are not limited to a single spatial or temporal point and can be used to study the temporal or spatial dependence of the fluctuations. In the following sections we shall restrict the discussion of correlation function to the time-domain.

### 4.2.1 First-order correlation function

The first-order correlation function for a light beam measures the correlations between the electric field at a given position for different points in time. For a time separation of  $\tau$ , the first-order correlation function of a light field is defined as

$$g^{(1)}(\tau) = \frac{\langle E^*(t)E(t+\tau) \rangle}{[\langle |E(t)|^2 \rangle \langle |E(t+\tau)|^2 \rangle]^{1/2}} \quad (4.1)$$

where  $\langle X \rangle = \frac{1}{T} \int_{-T/2}^{T/2} X dt$  represents the time average over a time duration  $T$ . Radiated field from chaotic light source such as a discharge lamp or a thermal cavity consists of contributions from excited atoms decaying independently at different times. Consequently, the electric field for time delays,  $\tau \gg \tau_c$ ,<sup>1</sup> are completely uncorrelated. One can show [110] that in such a case, the average of the product of the electric fields (the numerator of 4.1) at two distant times is zero. Therefore, they exhibit a  $g^{(1)}(|\tau| \gg \tau_c)$  of zero where  $\tau_c$  is the coherence time. For smaller times  $g^{(1)}(t)$  lies in between 0 and 1 which defines partial coherence.

<sup>1</sup>For time delays of much smaller than the coherence time,  $\tau_c \propto 1/(\text{spectral linewidth})$ , even chaotic light sources can show non-zero first order correlations.

The coherence time defines the coherence length which is the path length traversed by the propagating light field during the coherence time. For path difference much longer than the coherence length, the electric fields derived from the same light source lose phase correlation and hence the ability to interfere. Since the coherence time,  $\tau_c \propto 1/\Delta\nu$  where  $\Delta\nu$  is the spectral width of the source, light from spectrally broadened light sources is often not suited for observing interference. On the other hand, a laser light is spectrally quite narrow, exhibits interference for very large values of  $\tau$ . An ideal laser source has  $g^{(1)}(\tau) = 1$  for all  $\tau$ .

### 4.2.2 Second-order correlation function

A second order correlation function in quantum optics quantifies the temporal dependence of intensity correlations of an electromagnetic field. It can be defined as

$$g^{(2)}(t, t + \tau) = \frac{\langle I(t)I(t + \tau) \rangle}{\langle I(t) \rangle \langle I(t + \tau) \rangle} \quad (4.2)$$

where  $\langle X \rangle = \frac{1}{T} \int_{-T/2}^{T/2} X dt$  for a classical function  $X$  and the time-averaged quantum mechanical expectation value,  $\langle \hat{X} \rangle = \lim_{T \rightarrow \infty} \frac{1}{T} \int_{-T/2}^{T/2} \langle \hat{X} \rangle dt$ , for a quantum operator  $\hat{X}$  and  $I(t)$  represents the intensity of the light field. For a narrow linewidth quantized laser light, one can express the electric field at a given point in time as a sum of negative and positive frequency components as:

$$\hat{E}(t) = \hat{E}^+(t) + \hat{E}^-(t) \propto \left( \frac{\hbar\omega_0}{2\epsilon_0 V} \right)^{1/2} [\hat{a}(t) + \hat{a}^\dagger(t)] \quad (4.3)$$

where, + and – indicate the positive and negative frequency components respectively and  $\hat{a}(t)$  is the annihilation operator at time  $t$  and  $\omega_0$  is the central frequency of the light spectrum. It turns out <sup>2</sup> that the intensity can be written as:

$$I(t) \propto \langle \hat{E}^-(t) \hat{E}^+(t) \rangle \quad (4.4)$$

, where  $\langle \dots \rangle$  now represents the time-averaged expectation value of the quantum operator inside the angle bracket. Using, equation 4.4, 4.3, and 4.2, one can obtain to obtain the definition of second-order coherence function as a function of the temporal delay  $\tau$  as [110]:

$$g^{(2)}(\tau) = \frac{\langle \hat{E}^-(t) \hat{E}^-(t + \tau) \hat{E}^+(t + \tau) \hat{E}^+(t) \rangle}{\langle \hat{E}^-(t) \hat{E}^+(t) \rangle \langle \hat{E}^-(t + \tau) \hat{E}^+(t + \tau) \rangle} = \frac{\langle \hat{a}^\dagger(t) \hat{a}^\dagger(t + \tau) \hat{a}(t + \tau) \hat{a}(t) \rangle}{\langle \hat{a}^\dagger(t) \hat{a}(t) \rangle \langle \hat{a}^\dagger(t + \tau) \hat{a}(t + \tau) \rangle} \quad (4.5)$$

where  $\langle \dots \rangle$  is the time-averaged quantum mechanical expectation value of the operator inside the angle brackets for a given quantized light field. Assuming the light field to be in a stationary state (for averaging over large times), we get:

$$g^{(2)}(\tau) = \frac{\langle \hat{a}^\dagger(t) \hat{a}^\dagger(t + \tau) \hat{a}(t + \tau) \hat{a}(t) \rangle}{\langle \hat{a}^\dagger(t) \hat{a}(t) \rangle^2} \quad (4.6)$$

<sup>2</sup>The intensity can be obtained from the definition of the Poynting vector for the quantized electromagnetic field as  $I = \epsilon_0 c^2 (\hat{E}^- \times \hat{B}^+ + \hat{B}^- \times \hat{E}^+)$ . For more details see ref [110]

Note that the normal ordering of operators, i.e., the creation (annihilation) operators are on the left (right), comes as a result of photon detection being modeled as an absorptive process [110,111].

#### 4.2.2.1 Classical light

Imagine a classical light field such as a light bulb the intensity of which is kept constant subject to random fluctuations about the mean value. This can be expressed as

$$I_{\text{classical}}(t) = i_0 + \delta i(t) \quad (4.7)$$

Substituting the above expression into equation 4.2, one obtains:

$$g_{\text{classical}}^{(2)}(\tau) = \frac{\langle i_0^2 + i_0(\delta i(t) + \delta i(t + \tau)) + \delta i(t) \delta i(t + \tau) \rangle}{(\langle i_0 + \delta i(t) \rangle)(\langle i_0 + \delta i(t + \tau) \rangle)}$$

The intensity fluctuations are random and average to zero, therefore the second and third term in the numerator disappears. Since the mean intensity is constant, the denominator is equivalent to squared of the mean intensity. This leads to

$$g_{\text{classical}}^{(2)}(\tau) = 1 + \frac{\langle \delta i(t) \delta i(t + \tau) \rangle}{i_0^2}$$

For large time scales the fluctuations are uncorrelated, therefore the numerator of the second term,  $\langle \delta i(t) \delta i(t + \tau) \rangle_{\tau \gg \tau_c} \rightarrow 0$ . This gives  $g_{\text{classical}}^{(2)}(\tau)$  the lower limit of 1. For time delays much smaller than the coherence time of the classical light source, the fluctuations can be correlated. In the limit of zero-time delay,  $\langle \delta i(t) \delta i(t + \tau) \rangle_{\tau=0} \langle (\delta i(t))^2 \rangle \geq 0$ . In general, one can write that correlation function for a classical field obeys the following inequalities [110]:

$$g_{\text{classical}}^{(2)}(0) \geq g_{\text{classical}}^{(2)}(\tau) \quad (4.8a)$$

$$g_{\text{classical}}^{(2)}(0) \geq 1 \quad (4.8b)$$

A light field whose second-order correlation measurement does not fulfill the above criteria is said to be non-classical.

#### 4.2.2.2 Single mode light field as non-classical light

Often a single mode plane wave light field with a well defined frequency and polarization is used as an example of nonclassical light. For a single frequency mode at  $\omega$ , the electric field at a given point in space evolves with time as:

$$\begin{aligned} \hat{E}(t) &= \hat{E}^+(t) + \hat{E}^-(t) \\ &= \left( \frac{\hbar\omega}{2\epsilon_0 V} \right)^{1/2} [\hat{a}e^{-i\theta} + \hat{a}^\dagger e^{i\theta}] \end{aligned} \quad (4.9)$$

where,  $\theta = \omega t$ , and  $\hat{a}$ ,  $\hat{a}^\dagger$  are the annihilation and creation operator for that mode at time  $t = 0$ . Using this in equation 4.5, we obtain:

$$g^{(2)}(\tau) = g^{(2)}(0) = \frac{\langle \hat{a}^\dagger \hat{a}^\dagger \hat{a} \hat{a} \rangle}{\langle \hat{a}^\dagger \hat{a} \rangle^2} \quad (4.10)$$

It must be noted that the right hand side of the above equation is independent of  $\tau$  only for a single mode state. The basis states of a quantized single mode light field - the so called *Fock states* exhibit non-classical  $g^{(2)}$ . To show that, we re-arrange equation 4.10 using commutation relation  $[\hat{a}, \hat{a}^\dagger] = 1$  to get:

$$\begin{aligned} g^{(2)}(0) &= \frac{\langle \hat{a}^\dagger (\hat{a} \hat{a}^\dagger - 1) \hat{a} \rangle}{\langle \hat{a}^\dagger \hat{a} \rangle^2} \quad (\hat{n} = \hat{a}^\dagger \hat{a}) \quad \frac{\langle \hat{n}^2 - \hat{n} \rangle}{\langle \hat{n} \rangle^2} \\ &= 1 + \frac{\langle (\Delta \hat{n})^2 \rangle - \langle \hat{n} \rangle}{\langle \hat{n} \rangle^2} \end{aligned} \quad (4.11)$$

where we used the definition of variance  $\langle (\Delta \hat{n})^2 \rangle = \langle \hat{n}^2 \rangle - \langle \hat{n} \rangle^2$  in the last step. Using the fact that Fock states are eigenstates of the number operator  $\hat{n}$  with eigenvalue  $n$  and variance of zero<sup>3</sup>, the  $g^{(2)}(\tau)$  for a Fock state  $|n\rangle$  corresponding to a single mode field is:

$$g^{(2)}(0) = 1 - \frac{1}{n} \quad (4.12)$$

where  $n \geq 1$ . For  $n > 1$ , it violates the inequality in equation 4.8 in section 4.2.2.1. The photon statistics observed for Fock state of light can therefore not be explained by classical description of propagating light field. The classical light fields show either Poissonian (laser light) or thermal distribution (incandescent light, thermal cavity etc) of photons when subject to photon counting [13]. On the other hand, Fock states show zero variance in photon number unlike the thermal states or Poission distributed states where the photon number variance is greater than or equal to mean. In general, equation 4.11 makes it clear that when  $\langle (\Delta \hat{n})^2 \rangle < \langle \hat{n} \rangle$ , the inequality observed by classical fields is violated. This is encapsulated in the *Mandel Q-parameter* [113] which is defined as

$$Q = \frac{\langle (\Delta \hat{n})^2 \rangle - \langle \hat{n} \rangle}{\langle \hat{n} \rangle^2} \quad (4.13)$$

Here,  $-1 \leq Q < 0$ , implies sub-Poissionian statistics i.e., the variance of photon number is less than the mean. This is also often called the non-classicality criteria.

### 4.2.2.3 Antibunched and bunched light

The light from a laser can well be described as coherent state of light. If one measures the number of photon detection events in a well-defined time interval, the resulting photon number

<sup>3</sup>Fock states  $|n\rangle$  is defined as the eignestate of light field which contains  $n$  quanta of energy or equivalently as many photonic excitations in the spatiotemporal mode of the light field. The eigenvalue equation is  $\hat{H}|n\rangle = \hbar\omega(\hat{n} + 1/2)|n\rangle = \hbar\omega(n + 1/2)|n\rangle$ . For more details see my master's thesis [112] or a textbook reference [110].

statistics is Poisson distributed. The photons arrive randomly in time in an uncorrelated fashion, and the normalized second-order correlation function for such a source is equal to one. This means that the photons do not have a preference of being together or far apart, i.e., on average the probability of two photons arriving with a certain delay is constant. If the photons tend to stay far apart from one another, then they are said to be anti-correlated or anti-bunched. The opposite to this is bunched photons where the photons tend to be grouped together. For very large delays, all correlation between arrival times of the photons is lost. Therefore, all sources show a  $g^{(2)}(\infty) = 1$ . Mathematically, the definition can be summarized as :

$$g^{(2)}(\tau) = 1 \quad \forall \tau \quad \implies \quad (\text{coherent state}) \quad (4.14a)$$

$$g^{(2)}(\tau) > g^{(2)}(0) \quad \implies \quad (\text{antibunching}) \quad (4.14b)$$

$$g^{(2)}(\tau) < g^{(2)}(0) \quad \implies \quad (\text{bunching}) \quad (4.14c)$$

Comparing the definition of antibunching in equation 4.14(b) to the criteria in equation 4.8(a), one can easily see that antibunching is a nonclassical phenomena. Having said that, both antibunching ( $g^{(2)}(\tau) > g^{(2)}(0)$ ) as well as sub-Poissonian statistics ( $g^{(2)}(0) < 1$ , see section 4.2.2.2) correspond to non-classical light fields. Both phenomena may occur together but they are not the same. Sub-Poissonian statistics does not imply antibunching [114, 115]. While antibunching and sub-Poissonian statistics both can be obtained only for a non-classical light field, the absence of antibunching or sub-Poissonian statistics does not necessarily mean that a light field is classical. Reference [114] shows that photons from resonance fluorescence photons, which exhibit antibunching, can show sub- or super-poissonian statistics depending on the interval over which the photon statistics is drawn and the bandwidth of the detector used.

Typical examples of antibunched light is resonance fluorescence from an atom [48, 116, 117] or light emitted from a quantum dot [118] or an ion [119]. The former was the first experimental demonstration of the quantum nature of spontaneously emitted photon. In the experiment sodium atoms were excited by a resonant light field, and the photons collected from the resulting spontaneous emission were subject to a HBT type experiment (see section 4.2.2.4) which then revealed a distinct antibunching. Examples of classical bunched light sources are incandescent light source where the occupancy of the higher photon number falls off exponentially with the number of photons [120].

#### 4.2.2.4 Measuring second-order intensity correlations

Measuring second order correlation function,  $g^{(2)}(\tau)$  defined in equation 4.6, in principle, needs only a single fast photon number resolving detector in principle, to record the photon arrival times and extract the intensity at two time points separated by  $\tau$ . However, in realistic scenarios the detectors used in the lab are not fast enough. The detection mechanism (usually avalanche photodiodes) requires a certain time for the detector to recover from a photon detection event. Due to this, a single detector setup cannot detect multiple events if the correlation time lie within this detector dead time. For low photon fluxes, the solution to this problem is to divide the beam such that one can detect the second click on a second detector despite the first detector's dead-time.



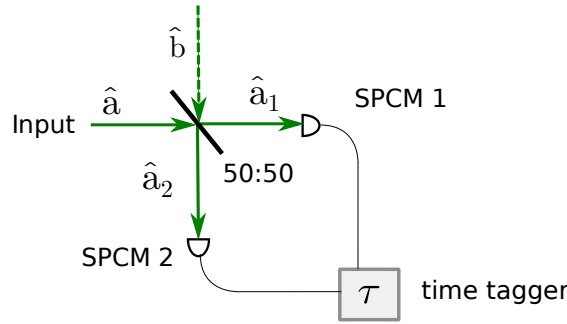


Figure 4.1: Schematics of a Hanbury Brown-Twiss type of setup for measuring temporal correlations in intensity.

Hanbury-Brown-Twiss first came up with the experiment on measuring the correlations between photons in two coherent beams of light [121]. A schematic of their setup is shown in Figure 4.1 where a light beam is incident on one of the input ports of a 50:50 beam-splitter. Two single photon counting modules (SPCMs) are placed in the two output ports which generate a TTL pulse upon detection of a photon. The output pulse of each detector is sent to a timetagger which records the timestamp whenever it receives a pulse. This setup allows one to record the photon arrival times on the detectors and from there extract a correlation function defined as:

$$g^{(2)}(\tau) = \frac{\langle \hat{a}_1^\dagger(t) \hat{a}_2^\dagger(t+\tau) \hat{a}_2(t+\tau) \hat{a}_1(t) \rangle}{\langle \hat{a}_1^\dagger(t) \hat{a}_1(t) \rangle \langle \hat{a}_2^\dagger(t+\tau) \hat{a}_2(t+\tau) \rangle} \quad (4.15)$$

where  $\hat{a}_1(t)$  and  $\hat{a}_2(t+\tau)$  are the annihilation operators in the two modes at time  $t$  and  $t+\tau$  respectively. One can prove that the expression 4.15 is equivalent to the  $g^{(2)}(\tau)$  for the input beam. For this we use the beam-splitter transformation  $\hat{a}_1 = (\hat{a} - \hat{b})/\sqrt{2}$  and  $\hat{a}_2 = (\hat{a} + \hat{b})/\sqrt{2}$ , and calculate the expectation values in the numerator and denominator of the RHS of equation 4.15 for the input two-mode state  $|\psi\rangle = |\psi_a\rangle \otimes |0\rangle$ , where the input  $|\psi_a\rangle$  corresponds to mode  $\hat{a}$  and the vacuum state  $|0\rangle$  corresponds to the mode  $\hat{b}$ . For brevity, I shall use the notation  $t' = t + \tau$  and  $\hat{a}, \hat{b}$  and  $\hat{a}', \hat{b}'$  for operators at time  $t$  and  $t'$  respectively. It follows that

$$\begin{aligned} \langle \hat{a}_1^\dagger(t) \hat{a}_1(t) \rangle &= \langle \psi_a, 0 | \hat{a}^\dagger \hat{a} - \hat{a}^\dagger \hat{b} - \hat{b}^\dagger \hat{a} + \hat{b}^\dagger \hat{b} | \psi_a, 0 \rangle / 2 \\ &\stackrel{\hat{b}|0\rangle = \langle 0 | \hat{b}^\dagger = 0}{=} \langle \psi_a | \hat{a}^\dagger \hat{a} | \psi_a \rangle / 2 \end{aligned} \quad (4.16a)$$

$$\begin{aligned} \langle \hat{a}_2^\dagger(t') \hat{a}_2(t') \rangle &= \langle \psi_a, 0 | \hat{a}'^\dagger \hat{a}' + \hat{a}'^\dagger \hat{b}' + \hat{b}'^\dagger \hat{a}' + \hat{b}'^\dagger \hat{b}' | \psi_a, 0 \rangle / 2 \\ &\stackrel{\hat{b}|0\rangle = \langle 0 | \hat{b}^\dagger = 0}{=} \langle \psi_a | \hat{a}'^\dagger \hat{a}' | \psi_a \rangle / 2 \end{aligned} \quad (4.16b)$$

$$\begin{aligned} \langle \hat{a}_1^\dagger(t) \hat{a}_2^\dagger(t') \hat{a}_2(t') \hat{a}_1(t) \rangle &= \langle \psi_a, 0 | (\hat{a}^\dagger - \hat{b}^\dagger) (\hat{a}'^\dagger + \hat{b}'^\dagger) (\hat{a}' + \hat{b}') (\hat{a} - \hat{b}) | \psi_a, 0 \rangle / 4 \\ &\stackrel{\hat{b}|0\rangle = \langle 0 | \hat{b}^\dagger = 0}{=} \langle \hat{a}^\dagger \hat{a}'^\dagger \hat{a}' \hat{a} \rangle / 4 \end{aligned} \quad (4.16c)$$

Using equations 4.16 and equation 4.15, one obtains the expression for second-order correlation function for the input as defined in equation 4.5. Therefore, using the HBT scheme shown in

Figure 4.1, one can measure the second-order correlation function for a given input state despite the dead time of the detector.

### 4.3 Photon transport across coupled emitters

The observation of discrete lines in the Hydrogen and Helium spectrum [122] sparked among the scientists in the early 20<sup>th</sup> century an interest to study light-matter interaction in depth [5, 8, 9, 123]. The discovery of lasers in the mid-half of the 20<sup>th</sup> century provided scientist a coherent, quasi-monochromatic light source with well-defined photon statistics [13]. Since then there have been numerous research papers about studying the phenomena of photon scattering by a single or multiple atomic emitters coupled to a resonant laser light field [116, 124, 125]. Efficient light-matter interaction relies on strong coupling of the photons to a two-level quantum emitter. An obvious instrument for increasing it beyond free-space coupling strength is using a cavity or a strongly confining waveguide as a tool to enhance the coupling [41, 64, 126–130]. The latter approach is a convenient tool owing to its size, feasibility of implementation and fabrication. The theoretical study of the phenomenon of photon scattering from quantum emitters has gathered attention few decades ago [125, 131, 132]. Since then there have been several detailed studies on expanding the physical understanding of photon scattering, and to control it, especially through waveguide-coupled quantum emitters [41, 49, 51, 133–137]. To get an understanding of photon transport in complex quantum systems with multiple photons or emitters, it is essential to understand the most basic scheme of a single photon scattering across a waveguide coupled to number of quantum emitters as in reference [133, 137]. Therefore in the following section I will discuss in full detail the respective theory.

#### 4.3.1 One-photon scattering across a waveguide coupled to a single emitter

In this section I will derive a model for the problem of single photon scattering by a two-level quantum impurity coupled to the waveguide through which the photon is propagating. The steps here, follow the approach outlined in references [133, 134, 137]. In the following, we consider a single photonic excitation travelling inside a waveguide which is coupled to a two level atom (see Figure 4.2). For this system one can write the Hamiltonian as

$$\begin{aligned} \frac{\hat{H}}{\hbar} = & \int dx \left[ \hat{c}_R^\dagger(x) (\omega_{arb} - iv_g \frac{\partial}{\partial x}) \hat{c}_R(x) + \hat{c}_L^\dagger(x) (\omega_{arb} + iv_g \frac{\partial}{\partial x}) \hat{c}_L(x) \right] \\ & + V_R \int dx \delta(x) \left[ \hat{S}_+ \hat{c}_R(x) + \hat{c}_R^\dagger(x) \hat{S}_- \right] + V_L \int dx \delta(x) \left[ \hat{S}_+ \hat{c}_L(x) + \hat{c}_L^\dagger(x) \hat{S}_- \right] \\ & + (\omega_e - i\gamma_e/2) \hat{a}_e^\dagger \hat{a}_e + \omega_g \hat{a}_g^\dagger \hat{a}_g \end{aligned} \quad (4.17)$$

where, the operators  $\hat{c}_R^\dagger(x), \hat{c}_L^\dagger(x)$  correspond to the bosonic operator creating a right- and left-propagating photon respectively,  $\hat{S}_- = \hat{S}_+^\dagger = \hat{a}_g^\dagger \hat{a}_e = |g\rangle \langle e|$ , where the letters  $e$  and  $g$ , correspond to the excited and ground state of the two-level emitter,  $|e\rangle$  and  $|g\rangle$ , with energies  $\omega_e$  and  $\omega_g$  respectively,  $V_L$  and  $V_R$  are the dipole interaction term, and  $\gamma_e$  accounts for the spontaneous emission of the excited state into other modes different from the waveguide mode (free space),

$\omega$  is the frequency of the input light field. We linearize the dispersion of the waveguide such that  $\omega = \omega_{arb} + v_g Q$ , where  $Q$  is the wavevector of the input light field around the frequency  $\omega$  and  $v_g$  is the photon group velocity. The first line of the equation corresponds to the energy of a single photonic excitation in the right and left propagating modes of the waveguide. The first and second brackets on the second line of equation 4.17 corresponds to the interaction of the right and left propagating photon with the atom that sits at the position  $x = 0$ . In the following, we consider a photon incident from the left. The atom may absorb this photon, get excited and then decay by emitting a photon. A photon emission into the environment is described by the non-Hermitian damping term,  $-i(\gamma_e/2)\hat{a}^\dagger\hat{a}$ , of the Hamiltonian. The emitted photon can also couple into the right or left propagating mode as describe by the second line. The coupling constant to the left and right propagating mode,  $V_{L/R}$ , is related to the decay rates into the left and right propagating waveguide modes,  $\Gamma_{wg}^\alpha = V_\alpha^2/v_g$  for  $\alpha \in \{L, R\}$  and, in general,  $V_L \neq V_R$  indicates a chiral atom-light interaction [138]. In the following, we will derive a steady state solution of 4.17. The steady state solution will comprise of a superposition of the photon in the left and right propagating mode and the atom being in excited state with a certain probability. This can be represented mathematically as

$$|\Psi(t)\rangle = e^{-i\omega't} \left( \int dx \left[ \phi_R(x)\hat{c}_R^\dagger(x) + \phi_L(x)\hat{c}_L^\dagger(x) \right] + \phi_a\hat{a}_e^\dagger\hat{a}_g \right) |\phi\rangle = e^{-i\omega't} |\psi\rangle \quad (4.18)$$

where  $|\phi\rangle = |0, g\rangle$  represents zero photons and atom in the ground state and  $\omega' = \omega + \omega_g$  is the energy of the steady state solution which is equal to the energy of the single photonic excitation which interacts with the atom and the energy of the atom in the ground state. We can write the Schrödinger equation  $\hat{H}|\Psi(t)\rangle = i\hbar\partial/\partial t|\Psi(t)\rangle$  which translates to  $\hat{H}|\psi\rangle = \hbar\omega'|\psi\rangle$  for the steady-state case. By using equation 4.18 and 4.17, we obtain :

$$\begin{aligned}
 \frac{\hat{H}}{\hbar}|\psi\rangle &= \int dx (\omega_{arb}\phi_R(x) - iv_g\phi'_R(x)) \hat{c}_R^\dagger(x) |\phi\rangle \\
 &+ \int dx (\omega_{arb}\phi_L(x) + iv_g\phi'_L(x)) \hat{c}_L^\dagger(x) |\phi\rangle \\
 &+ V_R \int dx \delta(x) \left( \hat{S}_+\hat{c}_R \int dx' \phi_R(x')\hat{c}_R^\dagger(x') + \hat{c}_R^\dagger(x)\hat{S}_-\phi_a\hat{S}_+ \right) |\phi\rangle \\
 &+ V_L \int dx \delta(x) \left( \hat{S}_+\hat{c}_L(x) \int dx' \phi_L(x')\hat{c}_L^\dagger(x') + \hat{c}_L^\dagger(x)\hat{S}_-\phi_a\hat{S}_+ \right) |\phi\rangle \\
 &+ (\omega_e - i\gamma_e/2)\hat{a}_e^\dagger\hat{a}_e\phi_a\hat{a}_e^\dagger\hat{a}_g |\phi\rangle + \omega_g\phi_a\hat{a}_g^\dagger\hat{a}_g |\phi\rangle
 \end{aligned} \quad (4.19)$$

where,  $\phi'_i = \partial\phi_i/\partial x$ . In the following, we consider, without loss of generality, the situation where the photon is initially incident from the left (right propagating). The third interaction term of the form  $\hat{S}_+\hat{c}_L$ , is not possible as it describes a process where the photon is incident from the right (left propagating) and excites the atom. Therefore, for a single excitation case we ignore this term. Using the commutation relation  $[\hat{c}(x), \hat{c}^\dagger(x')] = \delta(x - x')$ , as well as,

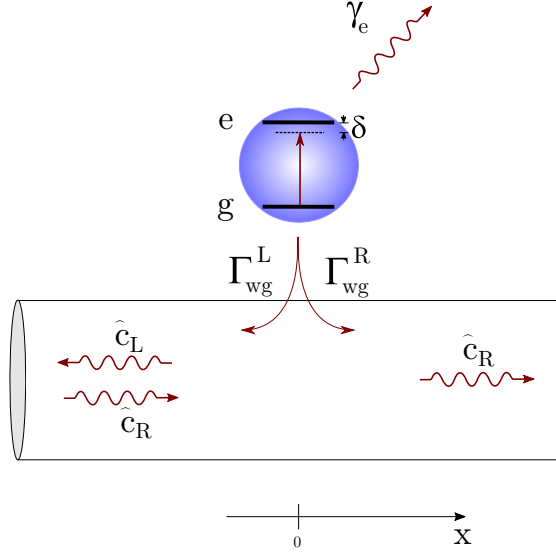


Figure 4.2: Schematics of a single two-level quantum emitter coupled to a nanofiber-like waveguide with the left (right) propagating modes denoted by the subscript  $R$  and  $L$ . The emitter sits at  $x = 0$  with decay rates into free-space as  $\gamma_e$  and into left and right propagating waveguide modes as  $\Gamma_{wg}^L$  and  $\Gamma_{wg}^R$  respectively. The input light field is at frequency  $\omega$  detuned from the atomic transition frequency ( $\omega_e - \omega_g$ ) by  $\delta$ .

$\hat{O}|\phi\rangle = 0 \forall \hat{O} \in \{\hat{S}^-, \hat{c}_R, \hat{c}_L\}$ , one arrives at the Eigenvalue equation

$$\begin{aligned}
 \frac{\hat{H}}{\hbar}|\psi\rangle &= \int dx (\omega_{arb}\phi_R(x) - iv_g\phi'_R(x)) \hat{c}_R^\dagger|\phi\rangle \\
 &+ \int dx (\omega_{arb}\phi_L(x) + iv_g\phi'_L(x)) \hat{c}_L^\dagger|\phi\rangle \\
 &+ V_R \int dx \delta(x) (\phi_R(x)\hat{S}_+ + \phi_a\hat{c}_R^\dagger) + V_L \int dx \delta(x) (\phi_a\hat{c}_L^\dagger)|\phi\rangle \\
 &+ (\omega_e - i\gamma_e/2)\phi_a\hat{S}_+|\phi\rangle + \omega_g \int dx (\phi_R(x)\hat{c}_R^\dagger + \phi_L(x)\hat{c}_L^\dagger)|\phi\rangle \\
 &= (\omega + \omega_g)|\psi\rangle
 \end{aligned} \tag{4.20}$$

Comparing equation 4.18 and 4.20, one can see that the equations contains terms corresponding to the states  $\int dx \hat{c}_R^\dagger(x)|\phi\rangle$ ,  $\int dx \hat{c}_L^\dagger(x)|\phi\rangle$ , and  $\hat{a}_e^\dagger\hat{a}_g|\phi\rangle$ . Equating the probability amplitudes, gives us the following set of coupled equations.

$$-iv_g\phi'_R(x) + \delta(x)V_R\phi_a = (\omega - \omega_{arb})\phi_R(x) \tag{4.21a}$$

$$iv_g\phi'_L(x) + \delta(x)V_L\phi_a = (\omega - \omega_{arb})\phi_L(x) \tag{4.21b}$$

$$(\omega_e - i\gamma_e/2)\phi_a + V_R\phi_R(0) = (\omega + \omega_g)\phi_a \tag{4.21c}$$

To solve the above set of differential equations, we use the ansatz:

$$\phi_R(x) = e^{iQx} [\theta(-x) + t \theta(x)] \quad (4.22a)$$

$$\phi_L(x) = e^{-iQx} r \theta(-x) \quad (4.22b)$$

From this we can calculate the derivatives as:

$$\phi'_R(x) = iQ\phi_R(x) + e^{iQx} [\theta'(-x) + t \theta'(x)] \quad (4.22c)$$

$$\phi'_L(x) = -iQ\phi_L(x) + e^{-iQx} r \theta'(-x) \quad (4.22d)$$

where  $\theta(x)$  is the Heaviside step function with the values 1/2 at  $x = 0$  and derivatives  $\lim_{x \rightarrow 0} \theta'(\pm x) = \delta(x)$ ,  $Q$  is the wave-vector of the input photon with frequency  $\omega$  and  $t$  and  $r$  are the field transmission and reflection coefficients, respectively. Using this Ansatz for the coupled equations 4.23, we obtain for  $x = 0$

$$-iv_g \phi'_R(0) + V_R \phi_a = (\omega - \omega_{arb}) \phi_R(0) \quad (4.23a)$$

$$iv_g \phi'_L(0) + V_L \phi_a = (\omega - \omega_{arb}) \phi_L(0) \quad (4.23b)$$

$$(\omega_e - i\gamma_e/2) \phi_a + V_R \phi_R(0) = (\omega + \omega_g) \phi_a \quad (4.23c)$$

Substituting from 4.22, we obtain:

$$(\omega - \omega_{arb})(1 + t) - i2v_g(t - 1) + 2V_R \phi_a = (\omega - \omega_{arb})(1 + t) \quad (4.24a)$$

$$(\omega - \omega_{arb})r - i2v_g r + 2V_L \phi_a = (\omega - \omega_{arb})r \quad (4.24b)$$

$$2(\omega_e - i\gamma_e/2) \phi_a + V_R(1 + t) = 2(\omega + \omega_g) \phi_a \quad (4.24c)$$

Solving the above set of equations yields the field reflection and transmission coefficients for the general case as:

$$t = \frac{\gamma_e - V_R^2/v_g - i2\delta}{\gamma_e + V_R^2/v_g - i2\delta} = \frac{\gamma_e - \Gamma_{wg}^R - i2\delta}{\gamma_e + \Gamma_{wg}^R - i2\delta} \quad (4.25a)$$

$$r = \frac{-2V_L V_R}{v_g(\gamma_e + V_R^2/v_g - i2\delta)} = \frac{-2\sqrt{\Gamma_{wg}^R \Gamma_{wg}^L}}{\gamma_e + \Gamma_{wg}^R - i2\delta} \quad (4.25b)$$

where, in the last step, we have introduced the detuning  $\delta = \omega - (\omega_e - \omega_g)$  and substituted  $V_{L/R}^2/v_g = \Gamma_{wg}^{L/R}$ . However, we are interested in the chiral case, where,  $V_R \gg V_L$  and hence the  $\Gamma_{wg}^R \gg \Gamma_{wg}^L$ . Therefore, in the chiral limit, we substitute  $V_L \rightarrow 0$ . Setting  $V_R^2/v_g = \Gamma_{wg}^R = \Gamma_{wg}$ , one obtains the field transmission amplitude for the chiral case as

$$t = \frac{\gamma_e - \Gamma_{wg} - i2\delta}{\gamma_e + \Gamma_{wg} - i2\delta} \quad (4.26)$$

The same result can be obtained by input-output formalism as discussed in reference [136].

### 4.3.2 Optical depth due to a single waveguide-coupled atom

We can define the coupling constant,  $\beta$ , as the ratio of light scattered into the guided mode versus the light scattered into all possible channels by the atom,  $\Gamma_{tot} = \gamma_e + \Gamma_{wg}$ . This can be expressed as

$$\beta = \frac{\Gamma_{wg}}{\Gamma_{tot}} \quad (4.27)$$

In this way, equation 4.26 simplifies to

$$t(\delta) = 1 - \frac{2\beta}{1 - i2\delta/\Gamma_{tot}} \quad (4.28)$$

For on-resonance light ( $\delta = 0$ ), and in the limit of weak coupling ( $\beta \ll 1$ ), the power transmission is given by  $T = |t|^2$ . In the linear absorption regime, optical depth is related to the transmission as  $-\ln[T]$ , therefore, for a single atom the on-resonance ( $\delta = 0$ ), we can define the optical depth per atom is given as:

$$OD/\text{atom} = \ln[T_{\text{atom},\delta=0}] = \ln[|t(\delta=0)|^2] = \ln[(1 - 2\beta)^2] \approx 4\beta \quad (4.29)$$

The on-resonance transmission for  $N$  atoms is given as  $T_N(\delta=0) = (1 - 2\beta)^{2N}$  as is also used in the reference [139].

### 4.3.3 Two-photons scattering across single emitter: Scattering matrix formalism

In section 4.3.1 we looked at a single photon propagating in a waveguide chirally coupled to a single quantum impurity. To understand the physics of photon transport in a nanofiber based atomic ensemble, we need to consider the case where more than one photon interacting with quantum emitter which is a non-trivial task. Reference [49, 136, 139] have solved this problem by introducing the scattering matrix formalism for a single emitter problem and extending it to the case of multiple coupled quantum emitters. They use a weak coherent state as the input limiting their calculations to the situation of at most two photons. The scattering process is represented as a matrix,  $\hat{S}_{mn}$ , corresponding to a projective operator in the Fock-basis,  $|m\rangle\langle n|$ , where  $(m, n) \leq 2$ . The wavefunction of the eigenstates of the scattering matrix is expressed in the position basis. The total scattering process of photons on a quantum emitter can then be written as a sum of individual scattering processes as:

$$\hat{S} = \hat{S}_{11} + \hat{S}_{22} + \hat{S}_{12} \quad (4.30)$$

The three matrices,  $\hat{S}_{11}$ ,  $\hat{S}_{22}$ , and  $\hat{S}_{12}$  describe the single photon, the two-photon scattering process and the two-photon scattering process where one photon is lost.

#### $\hat{S}_{11}$ matrix:

The basis states for the  $\hat{S}_{11}$  matrix is a single photon Fock state defined by the bosonic annihilation operator  $\hat{a}_\delta^\dagger$  where  $\delta$  is the detuning from the transition frequency of the quantum emitter.

The transformation of single photon, described by the  $\hat{S}_{11}$  matrix is given by

$$\hat{a}_\delta^\dagger \xrightarrow{\hat{S}_{11}} t_\delta \hat{a}_\delta^\dagger(\delta) \quad (4.31)$$

where  $t_\delta$  is the complex transmission factor defined in 4.26.

### $\hat{S}_{22}$ matrix:

The two photon scattering process is more complicated as it may lead to energy exchange between the photons. Reference [49] has used the Bethe-ansatz approach to derive the analytical form of the two-photon wavefunctions that can be used as an orthonormal basis for describing the input and output two-photon state and hence the two photon scattering matrix. Another alternative approach utilizing the input-output formalism also arrives at the same result [136]. In the basis of so called *bound* and *unbound states*, one can express the  $\hat{S}_{22}$  operator as [49, 139]:

$$\hat{S}_{22} = \sum_{\delta_1, \delta_2} \bar{t}_{\delta_1} \bar{t}_{\delta_2} |W_{\delta_1, \delta_2}\rangle \langle W_{\delta_1, \delta_2}| + \sum_E \tilde{t}_E |B_E\rangle \langle B_E| \quad (4.32)$$

where we have followed the notation of reference [51], where the waveguide dispersion is linearized and the group velocity is set to 1 such that time separation can be equivalently expressed by position separation and the dimensions of wave-number, frequency as well as distance and time are the same, and  $\delta_1$  and  $\delta_2$  are photon detunings such that  $E = \delta_1 + \delta_2$  is the two photon detuning and  $\Delta = (\delta_1 - \delta_2)/2$  is the difference of two-photon energies. The state  $|W_{\delta_1, \delta_2}\rangle$  is the so called Weigmann Andrei States and the  $|B_E\rangle$  are called the bound-states. Mapping  $\{\delta_1, \delta_2\}$  to  $\{E, \Delta\}$  and switching to continuous variable, we can re-write the equation 4.32 as

$$\hat{S}_{22} = \frac{1}{2} \iint dE d\Delta \bar{t}_{E/2+\Delta} \bar{t}_{E/2-\Delta} |W_{E, \Delta}\rangle \langle W_{E, \Delta}| + \int dE \tilde{t}_E |B_E\rangle \langle B_E| \quad (4.33)$$

where the two-photon basis states can be expressed as:

$$|W_{E, \Delta}\rangle = \frac{1}{\sqrt{2}} \iint dx_1 dx_2 \hat{a}^\dagger(x_1) \hat{a}^\dagger(x_2) W_{E, \Delta}(x_c, x) |0\rangle \quad (4.34a)$$

$$|B_E\rangle = \frac{1}{\sqrt{2}} \iint dx_1 dx_2 \hat{a}^\dagger(x_1) \hat{a}^\dagger(x_2) B_E(x_c, x) |0\rangle \quad (4.34b)$$

and the real-space representation of the basis states is written as:

$$W_{E, \Delta}(x_c, x) = \frac{1}{\sqrt{4\Delta^2 + \Gamma^2}} \frac{\sqrt{2}}{2\pi} e^{iEx_c} [2\Delta \cos(\Delta x) - \Gamma \text{sgn}(x) \sin(\Delta x)] \quad (4.34c)$$

$$B_E(x_c, x) = \sqrt{\frac{\Gamma}{4\pi}} e^{iEx_c} e^{-\frac{\Gamma}{2}|x|} \quad (4.34d)$$

where,  $x_c = (x_1 + x_2)/2$  is the centre-of-mass coordinate and  $x = x_1 - x_2$  is the position difference. The transmission amplitudes defined in equation 4.32 can be written as

$$\bar{t}_e = \frac{e + i\Gamma(1 - 2\beta)/(2\beta)}{e + i\Gamma/(2\beta)}, \quad e \in \{\delta_1, \delta_2\} \quad (4.35a)$$

$$\tilde{t}_E = \frac{E + i\Gamma(1 - 3\beta)/\beta}{E + i\Gamma(1 + \beta)/\beta} \quad (4.35b)$$

### $\hat{S}_{21}$ matrix:

There can be a scattering event where one photon from the two incident photons gets lost to the environment via scattering into the radiative mode from the atomic emitter. Reference [139] has modeled the radiative loss as being equivalent to a emission in the backward direction. The chiral approximation [41], does not allow for coupling of the forward and backward propagating modes as the treatment does not consider backward propagating photons (see section 4.3.1 for details). Therefore, the photon emitted into the backward propagating mode is effectively lost, therefore, similar to the photon being scattered into the radiative modes. The scattering matrix corresponding to this process is represented by (taken from Reference [51]):

$$\begin{aligned} \hat{S}_{21} \iint d\delta_1 d\delta_2 \hat{a}^\dagger(\delta_1) \hat{a}^\dagger(\delta_2) |0\rangle f(\delta_1, \delta_2) = \\ \iint d\delta_1 d\delta_2 \hat{a}_R^\dagger(\delta_1) \hat{a}_{loss}^\dagger(-\delta_2) |0\rangle \left[ 2\bar{r}_{-\delta_2} \bar{t}_{\delta_1} f(\delta_1, -\delta_2) \right. \\ \left. + \frac{i\beta\sqrt{\Gamma(1-\beta)}}{\pi} \bar{s}_{\delta_1} \bar{s}_{-\delta_2} \int d\bar{\delta}_1 d\bar{\delta}_2 (\bar{s}_{\bar{\delta}_1} + \bar{s}_{\bar{\delta}_2}) \delta(\delta_1 - \delta_2 - \bar{\delta}_1 - \bar{\delta}_2) f(\bar{\delta}_1, \bar{\delta}_2) \right] \end{aligned} \quad (4.36)$$

where  $\hat{a}_R^\dagger(\delta_1)$  creates a forward propagating photon and  $\hat{a}_{loss}^\dagger(\delta_1)$  creates a backward propagating photon (with negative wavevector),  $\bar{r}_\delta = -2i\sqrt{\beta(1-\beta)}/(1 - 2i\delta/\Gamma_{tot})$  and  $\bar{s}_\delta = \sqrt{\Gamma_{tot}}/(\delta + i\Gamma_{tot}/2)$ . In case that there are more than one emitter, such a scattering process can happen only once in the limit of a two-photon input state.

### 4.3.4 Scattering matrix with multiple emitters

Extention of the scattering matrix to  $N$  emitters is simply obtained from the single emitter matrix (see equation 4.33) taken to the  $N^{\text{th}}$  power. The single photon scattering matrix,  $\hat{S}_{11}$ , contributes as:

$$\hat{S}_{11}^N = t_\delta^N \hat{a}_\delta^\dagger |1\rangle \langle 1| \quad (4.37)$$

where  $t_\delta$  is the transmission given by equation 4.28 and  $N$  in the superscript is the number of atoms. The two photon scattering matrix,  $\hat{S}_{22}$ , for transmission through  $N$  atoms similarly obtained by applying the scattering matrix consecutively for each atom. This translates to taking the  $N^{\text{th}}$  power of the transmission coefficients



$$\hat{S}_{22}^N = \frac{1}{2} \int dE d\Delta (\bar{t}_{E/2+\Delta})^N (\bar{t}_{E/2-\Delta})^N |W_{E,\Delta}\rangle \langle W_{E,\Delta}| + \int dE \bar{t}_E^N |B_E\rangle \langle B_E| \quad (4.38)$$

The scattering process denoted by  $\hat{S}_{21}$  can happen only once in a chain of  $N$  emitters. Assuming that for the first  $M$  emitters, the two photon scattering, denoted by  $\hat{S}_{22}$ , happens, at  $M^{\text{th}}$  emitter the process  $\hat{S}_{21}$  happens, then, for the rest of the  $N - M - 1$  emitters only the process denoted by  $\hat{S}_{11}$  can happen because one photon is lost. The output after  $N$  emitters will be given by applying the matrix  $\sum_{M=0}^{N-1} \hat{S}_{11}^{N-M-1} \hat{S}_{12} \hat{S}_{22}^M$  where scattering process before and after the  $M^{\text{th}}$  atom is constrained to 2 and 1 incident photons respectively. In general, therefore, the transmission of an input with at most 2 photons through  $N$  quantum emitters, the net scattering process can be calculated from a sum of all possible scattering events in the mutually orthogonal one- and two-photon subspace:

$$\hat{S}^N = \hat{S}_{11}^N + \hat{S}_{22}^N + \sum_{M=0}^{N-1} \hat{S}_{11}^{N-M-1} \hat{S}_{12} \hat{S}_{22}^M \quad (4.39)$$

### 4.3.5 Total transmission

In many experiments, the typical input state can be considered a single-mode coherent state, which in low power/weak saturation limit can be approximated by:

$$\begin{aligned} |\alpha_{in}\rangle &= e^{-\frac{|\alpha|^2}{2}} e^{\alpha \hat{a}_{\delta_0}^\dagger} |0\rangle \\ &\sim e^{-\frac{|\alpha|^2}{2}} \left[ 1 + \alpha \hat{a}_{\delta_0}^\dagger + \frac{\alpha^2}{2} \hat{a}_{\delta_0}^\dagger(\delta_0) \hat{a}_{\delta_0}^\dagger(\delta_0) \right] |0\rangle \end{aligned} \quad (4.40)$$

where  $\hat{a}_{\delta_0}^\dagger$  creates a photon in the waveguide at detuning  $\delta_0$ . The input power can then be defined as  $P_{in} \approx \alpha^2$  with real  $\alpha$ . We can use the scattering matrices from the previous section and apply them to the single and two-photon components of the input state. The output state  $|\text{out}\rangle$  then consists of transmitted single photons and two photon components as

$$\begin{aligned} |\text{out}\rangle &= \hat{S}^N |\alpha_{in}\rangle \\ &= |\text{out}\rangle_1 + |\text{out}\rangle_2 \end{aligned} \quad (4.41)$$

where the output one- and two-photon states represented by  $|\text{out}\rangle_1$  and  $|\text{out}\rangle_2$  respectively can be expressed in terms of the scattering matrices as:

$$\begin{aligned} |\text{out}\rangle_1 &= |\text{out}\rangle_{11} + |\text{out}\rangle_{21} \\ &= \hat{S}_{11}^N \langle 1|\alpha_{in}\rangle |1\rangle + \sum_{M=0}^{N-1} \hat{S}_{11}^{N-M-1} \hat{S}_{12} \hat{S}_{22}^M \langle 2|\alpha_{in}\rangle |2\rangle \end{aligned} \quad (4.42a)$$

$$|\text{out}\rangle_2 = \hat{S}_{22}^N \langle 2|\alpha_{in}\rangle |2\rangle \quad (4.42b)$$

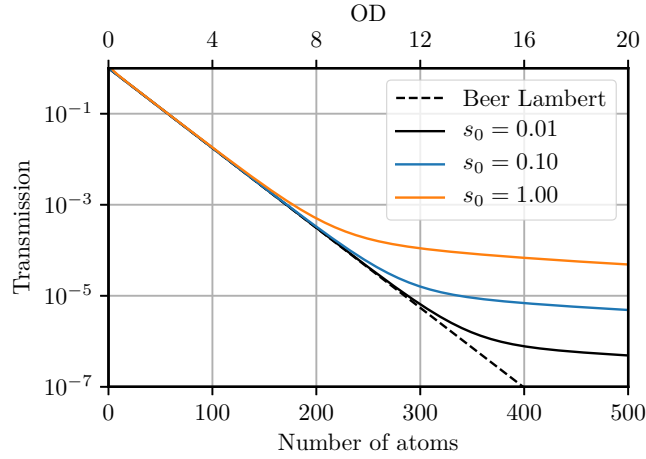


Figure 4.3: Predicted transmission for different number of atoms ( $N$ ) or correspond optical depth assuming  $\beta = 0.01$ . The three different curve correspond to different values of the incident probe power. The dashed line corresponds to the exponential decay of the transmission with atom number as predicted by the Beer-Lambert's law (see equation 4.29).

In the asymptotic limit of low  $\beta$  and weak saturation with large number of atoms, one can derive for the on-resonance transmission, a simplified expression [51]:

$$T = \frac{P_{out}}{P_{in}} = \underbrace{(1 - 2\beta)^{2N}}_{\propto \langle \hat{a}^\dagger \hat{a} \rangle_{11} \propto t_{\delta_0=0}^{2N}} + \underbrace{\frac{P_{in}}{8P_{sat}} \frac{\beta}{4\sqrt{\pi}(N\beta(1-\beta))^{3/2}} \frac{3 - 2\beta(1-\beta)}{1 - 2\beta(1-\beta)}}_{\propto \langle \hat{a}^\dagger \hat{a} \rangle_{21} + \langle \hat{a}^\dagger \hat{a} \rangle_{22}} \quad (4.43)$$

where the first term is the proportional to the output single photon flux due to single photon scattering ( $\hat{S}_{11}$ ), whereas the second term has contributions from two-photon scattering process ( $\hat{S}_{12}$  and  $\hat{S}_{22}$ ).

Figure 4.3 shows the asymptotic limit of the transmission (solid lines) as compared with the transmission for a linear absorber (dashed line) predicted by equation 4.29. The three solid lines show the transmission for different incident powers. The on-resonance saturation parameter experienced by the first atom in the chain is indicated by the values in the legend of the figure. There are a couple of interesting feature observable in transmission. First and foremost, the transmission from the atomic ensemble deviates from the transmission of a linear absorbing ensemble for large values of  $N$ . For a linear absorber, the transmission decays exponentially with the number of absorbers (here atoms). The first term, which is a consequence of linear absorption, has vanishing contribution for large number of atoms, thus the second term defines the transmission in this regime and yields a power-law dependence on the number of atoms. In the limit of large  $N$ , the second term of the equation 4.43 dominates. Therefore, the transmission decays as  $N^{-3/2}$  instead of the exponential decay,  $(1 - 2\beta)^{2N}$ , as predicted by the dashed black line. Also, from the figure, we see that with increasing saturation, the deviation of the transmission (solid lines) from that of a linearly absorbing medium (dashed line) is higher, indicating increasing nonlinear effects for higher saturation. In the following section, we shall look

at how one can get an even better understanding of the nonlinear phenomena by focusing on the correlated photon pair generated as a result of two-photon scattering process ( $\hat{S}_{22}$ ).

### 4.3.6 Two-photon output in transmitted light

It is interesting to consider the physics of the two-photon scattering process so as to understand why photon transport through nanofiber based ensemble gives rise to correlated photons. One can do a very simple treatment where only a single emitter is considered and then look at it in the limit of large number of emitters. Let us consider a two photon state:

$$|\psi_{k,p}\rangle = \iint dx_1 dx_2 g(x_1, x_2) \frac{1}{\sqrt{2}} \hat{c}^\dagger(x_1) \hat{c}^\dagger(x_2) |0, g\rangle \quad (4.44a)$$

where the *Bethe-Ansatz* dictates that the two photon wavefunction  $g(x_1, x_2)$  can, in general, be represented by a superposition of plane waves as:

$$g(x_1, x_2) = A e^{ikx_1 + ipx_2} + B e^{ipx_1 + ikx_2} \quad (4.44b)$$

where,  $A$  and  $B$  are two constants, and  $k$  and  $p$  are wavevectors corresponding to the plane wave solution to the free propagating photon. Wavevectors  $k$  and  $p$  also are linearly related to the photon detunings  $\delta_k$  and  $\delta_p$  from the resonance frequency of the emitter. Let the input  $|\psi_{k_1, p_1}\rangle$  undergo a two-photon scattering process, such that the output state,  $|\text{out}\rangle = \hat{S}_{22} \psi_{k_1, p_1}$ . The overlap of the output state with a plane wave-basis state is given as [49]:

$$\begin{aligned} \langle \psi_{k_2, p_2} | \hat{S}_{22} | \psi_{k_1, p_1} \rangle &= t_{k_1} t_{p_1} [\delta(k_1 - k_2) \delta(p_1 - p_2) + \delta(k_1 - p_2) \delta(k_2 - p_1)] \\ &+ B \delta(E_1 - E_2) \end{aligned} \quad (4.45)$$

where  $B$  is a function of  $k_1, p_1, k_2$  and  $p_2$  and  $E_i/\hbar = \delta_{k_i} + \delta_{p_i}$  is the total energy of the photon pair. Equation 4.45 gives us hint towards the presence of energy correlations in the output photon pair. The first and second term in equation 4.45 describe an uncorrelated two-photon state. The incident photons are transmitted directly (first term) or with momentum exchange (second term). The input two-photon component remains energetically uncorrelated i.e., the outgoing photons have the same individual energies as the incident photons. It can be verified [49] that the contribution to the uncorrelated part comes entirely from the  $|W_{k,p}\rangle$  part of the scattering matrix operator (see equation 4.32). In contrast the last term, which can also be written as  $\propto \delta(\delta_{k_1} + \delta_{p_1} - \delta_{k_2} - \delta_{p_2})$ , amounts to conservation of total energy but the individual energies of the outgoing photons can be different from that of the incident photons. This describes an output state where the two photons are highly correlated in their energies. This also means that an incident resonant photon pair may, after a two-photon scattering event emerge as a photon pair where each photon is detuned equally but in opposite directions from the resonance. Owing to this detuning such a photon pair suffers lesser attenuation (see equation 4.28) and is more likely to pass through the ensemble unabsorbed. In the following, we will see how generation of such correlated pair of photons combined with exponential attenuation of the single photons leads to deviation from the Beer-Lambert's law in the limit of large number of emitters.

### 4.3.7 Photon statistics in the output

One can see from section 4.3.5, that for a weakly saturating resonant field propagating through the nanofiber, the single photon component is attenuated (first term in equation 4.43) with exponential the number of coupled emitters. On the other hand, the two-photon transmission probability amplitude can be obtained from equation 4.42 as [51]:

$$\langle x_1, x_2 | \text{out} \rangle_2 = \psi_N(x_c, x) = e^{2i\delta_0 x_c / v_g} [t_{\delta_0}^{2N} - \phi_N(x)] \quad (4.46)$$

where,  $x_c$  is the centre-of-mass coordinate and  $x$  is the relative coordinate of the two photons as was used in equation 4.34. The first term,  $e^{2i\delta_0 x_c / v_g} t_{\delta_0}^{2N}$ , represents the uncorrelated photon pair wavefunction, which is extended in both  $x_1$  and  $x_2$  space similar to the input, but subject to attenuation by the factor  $t^{2N}$ , where  $N$  is the atom number, as we saw in equation 4.45. The value of  $t_{\delta_0}$  can be obtained from equation 4.35(a) by substituting single-photon detuning,  $\delta = \delta_0 = 0$ . The second term represents the correlated part with the spatial extent of the two-photon wavefunction being modified now by  $\phi_N(x)$ . There is a phase shift of  $\pi$  which can be explained by the quantum nature of absorption. The atom can absorb only one photon at a time. The second photon of the correlated pair can be seen as causing a stimulated emission of the first photon which gives a phase shift of  $\pi$  with respect to the incident light. A general expression for  $\phi_N(x)$  is cumbersome and can be found in reference [51]. Nevertheless, for resonant drive and in the limit of small coupling strength  $\beta$ , one can write expressions for the asymptotic limit of small and large optical depths as:

$$\phi_N(x) \approx 4N\beta^2 e^{-\Gamma|x|/(2v_g)} \quad (N\beta \ll 1, \text{ small OD}) \quad (4.47a)$$

$$\phi_N(x) \approx \frac{\beta\Gamma}{2\pi} \int d\delta \cos(\delta x / v_g) e^{-\xi_N^2 \Gamma / \delta^2} / \delta^2 \quad (N\beta \gg 1, \text{ large OD}) \quad (4.47b)$$

where  $\xi_N^2 = N\beta(1 - \beta)$ . One can notice an interesting trend for small coupling strength  $\beta$ . For a resonant drive, equations 4.35, 4.46, 4.47(a) give:

$$\psi_N(0, 0) = (1 - 2\beta)^{2N} - 4N\beta^2 \quad (4.48)$$

where the first term originates from the transmitted uncorrelated part of the two-photon wavefunction, whereas the second term originates from the linearly growing scattered two-photon component. For small  $N$  and  $\beta$ ,  $\psi_N(0, 0) \approx 1 - N(4\beta) + \mathcal{O}[\beta^2]$ , which is a linearly decreasing function with  $N$  but greater than zero. This originates from the fact that for small number of atoms ( $N \ll 1/\beta$ ), the uncorrelated two-photon amplitude dominates. Moreover as  $N$  is increased the uncorrelated part goes down exponentially where as the correlated part grows linearly<sup>4</sup>. At some point, when  $\phi_N(x) = t_{k_0}^{2N}$ , they cancel each other out making two photon contribution in the output go to zero. When  $N$  is increased further, the correlated photons dominate

<sup>4</sup>One can also verify this alternatively by showing that  $D(t_{\delta_0}^{2N}) < 0$  whereas  $D(\phi_N(x)) > 0$  from equation 4.47(a) where  $D := (\partial/\partial N)$ , and  $t_{\delta_0} = (1 - 2\beta)$  for low coupling strength  $\beta$  (see equation 4.29), and number of atoms is  $N$  where  $1 \leq N \ll 1/\beta$ .

the 2-photon probability amplitude until in the limit of  $N \gg 1/\beta$ ,  $\psi_N(0, x) \approx -\phi_N(x)$ . For large  $N$ , the single-photon component and uncorrelated two-photon component undergo exponential attenuation such that the output photons has a relatively higher fraction of the correlated two-photon component.

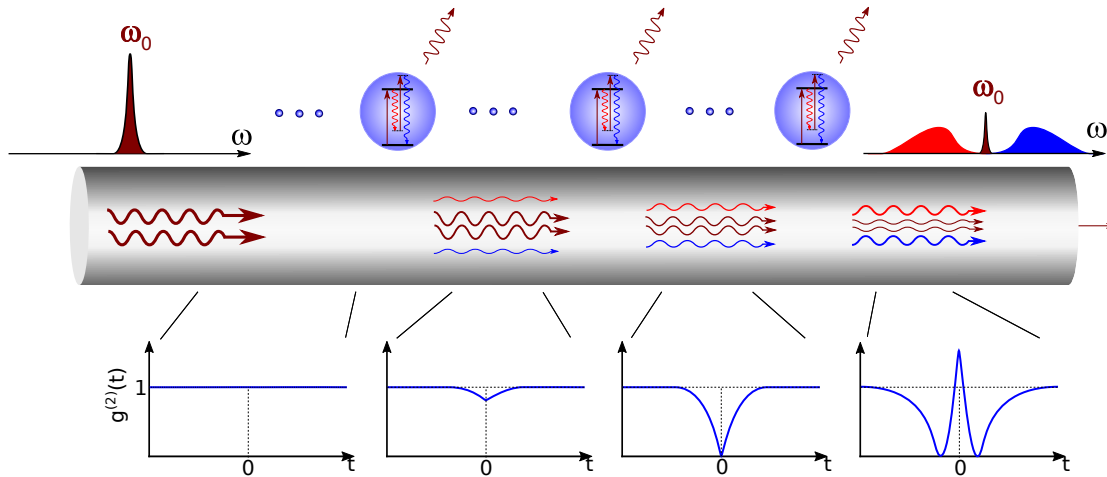


Figure 4.4: Two-photon transport dynamics of guided resonant light field (probe) interfaced with multiple two-level atoms interfaced with the nanofiber (grey cylinder). The blue circles depicting a 2-photon Raman scattering process denote the atoms with two probe photons as the input and the detuned photon pair as the output. The colored arrows in brown show the resonant probe photons whereas in red and blue show the red- and blue-detuned photon pair resulting from the two-photon scattering process. The curve arrow away from the atoms represent the photons lost to the radiative mode. Increasing arrow sizes show the increasing field strengths. The three atoms shown have many atoms in between represented by the blue ellipsis. The top left and right show the power spectrum of the input and output light field respectively. In the bottom is shown the expected correlation function of the transmitted field when sampled without atoms, after passing a few atoms, after passing the critical number of atoms where two-photon probability amplitude is zero, and after a large number of atoms where the correlated photons dominate the output.

Figure 4.4 depicts schematically the variation of the second-order correlation function for the light transmitted as it propagates through the ensemble. On the left bottom, where the light just enters into the waveguide, the photons correspond to the narrow-linewidth coherent laser beam and hence show a flat  $g^{(2)}(\tau)$  (bottom, left). After encountering a few atoms, there is small fraction of detuned correlated two-photon which contributes to the two-photon probability amplitude,  $\pi$  out of phase, with the mostly unattenuated uncorrelated component. Consequently, destructive quantum interference of two-photon probability amplitudes leads to reduced two-photon events at the output which leads to slight anti-bunching dip (bottom, second sketch) for a few atoms. With more scattering possibilities more of these correlated photon pairs are generated. At a critical number of atoms, the destructive quantum interference of the correlated

and uncorrelated two-photon probability amplitude (see equation 4.46) leads to perfect cancellation of the two-photon probability amplitude. In the limit of weak saturation, the output must then consist only of a stream of single photons that exhibit a strong antibunching at time scales comparable to inverse atomic linewidth (bottom third sketch). Upon increasing the number of emitters further, the correlated photon pair dominates over the transmitted uncorrelated single photons and two-photon pairs. This shows up in the form of monotonously increasing bunching with increasing atom number. Since the correlated photons consists mostly of the detuned photon pairs, the power spectrum of the output light must then consist mostly of the red- and blue-detuned sidebands. This is sketched in the top right of the figure 4.4 where the central resonant peak is attenuated exponentially while distinct sidebands emerge due to scattering from a large number of emitters.

### 4.3.8 Quantitative prediction

In the previous section, we saw that with increase in the number of atomic emitters coupled to the nanofiber waveguide, we increase the fraction of correlated photon pairs relative to the uncorrelated photons which should first lead to strong antibunching and then transition to bunching with increase in atom number. To quantify it one can compute the normalized second-order correlation function from equation 4.6. The numerator comes only from the two-photon component at the output, and is hence proportional to  $|\psi_N(x_c, x)|^2$  whereas the denominator is dependent on the total output flux. From the authors, we obtained the code for numerical evaluation of  $g^{(2)}(\tau = 0)$  up to zeroth order in  $P_{\text{in}}/P_{\text{sat}}$ , as a function of  $N$  and  $\beta$ . The resulting trend of  $g^{(2)}(0)$  with number of atoms  $N$  for a constant coupling strength  $\beta = 0.01$  is shown in Figure 4.5.

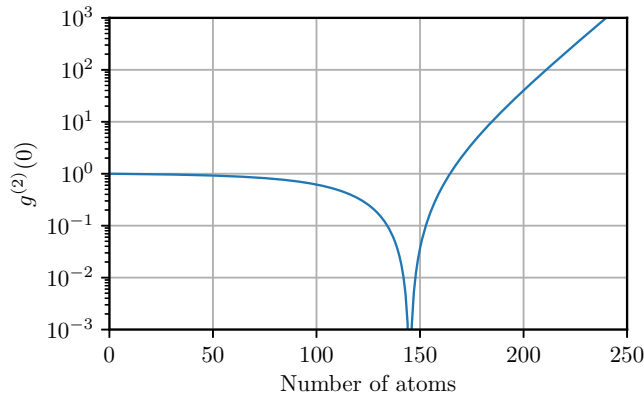


Figure 4.5: Variation of the second-order correlation function amplitude at time delay  $\tau = 0$  for varying number of atoms trapped around a nanofiber. The value of the coupling strength ( $\beta$ ) used for the above curve is 1%.

As was discussed in the previous section 4.3.6, for small optical depths (here proportional to small  $N$ ) one sees a decreasing two-photon amplitude as the number of emitters is increased. This is because of the increasing destructive interference of the two-photon probability ampli-

tude of the correlated and uncorrelated photons as the correlated two-photon amplitude grows. The point of lowest  $g^{(2)}(0)$  corresponds to the complete cancellation of the two-photon amplitude. Increasing  $N$  further enhances the correlated two-photon component further, as a result of which, the  $g^{(2)}(0)$  starts rising and grows beyond 1 at some point showing bunching at the output. As the dissipation is further increased by increasing number of atoms, correlated photon pairs constitute most of the output intensity which leads to increasing bunching.

In the next chapter, we shall show the experiment that we performed to analyze photon transport across atomic ensembles weakly coupled to the nanofiber guided modes. In particular, we measure experimentally the curve shown in figure 4.5, compare the experimentally obtained results with corresponding theoretical predictions.



Die approbierte gedruckte Originalversion dieser Dissertation ist an der TU Wien Bibliothek verfügbar.  
The approved original version of this doctoral thesis is available in print at TU Wien Bibliothek.



# Observation of correlated photon transport in nanofibers

In the present chapter, we shall look at how we studied experimentally the phenomena of correlated photon transport through an atomic ensemble trapped around a nanofiber-based waveguide. I will first explain our experimental setup and sequence design which allows us to probe atoms coupled to the nanofiber-guided light field. This will be followed by details on data taking and analysis. In the end, I will list the main results of our experimental study and discuss possible applications.

## 5.1 Experimental Methods

### 5.1.1 Setup

We trap laser-cooled cesium (Cs) atoms using a nanofiber-based two-color optical dipole trap [32, 64] as was described in detail in chapter 2 and chapter 3. The schematics of the experimental setup is outlined in Fig 5.1. The power of the blue-detuned light field (*blue trap*) at  $\lambda = 685$  nm is  $\sim 14$  mW. The pair of counter-propagating red-detuned fiber-guided light fields (*red trap*) at  $\lambda = 935$  nm has  $\sim 0.18$  mW per beam. Both trapping fields are at magic wavelength of Cs. All light fields are quasi-linearly polarised such that the blue-detuned trapping light field is perpendicular to the red-detuned trapping field and the probing field. In this configuration, the minima of the optical trap potential are located at a distance of  $\sim 250$  nm from the surface of the 400 nm diameter nanofiber as shown in figure 5.3.

#### 5.1.1.1 Detection

The input light field after transmission through the nanofiber-trapped atomic ensemble also contains photons from other light fields such as the trap laser induced Raman scattered photons from the optical fibers, residual trapping fields that remain after reflection from the dichroic mirrors

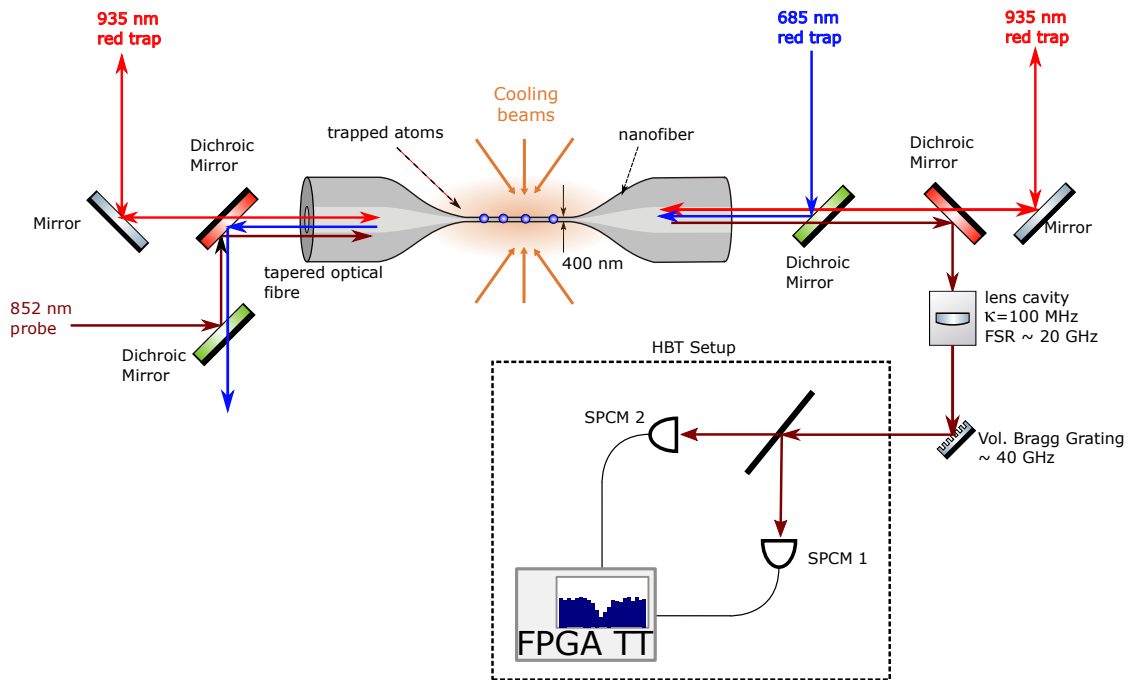


Figure 5.1: Experimental setup for trapping atoms and measuring correlations in the transmission. The two color optical dipole trap uses light fields at 935 nm and 685 nm, represented by the red and blue arrows and called the *red-trap* and *blue-trap* respectively. The probing light field depicted with brown colored arrows is sent in from one side of the nanofiber. After passing through the atomic ensemble, the transmitted probe at the nanofiber output is separated from the trapping fields using dichroic mirrors, and filtered further using an optical lens cavity and a volume bragg grating. It is then sent to a Hanbury-Brown Twiss (HBT) setup for coincidence detection using SPCMs connected to FPGA based time-tagging electronics.

and any amplified spontaneous emission from the lasers used in the experiment. Due to the high power ( $\sim 14$  mW) of the 685 nm blue-detuned trapping field, the resulting Raman scattered photons flux is high and contributes the most to the background photons around 852 nm. For this reason, the light transmitted through the nanofiber-coupled atomic ensemble is, first, sent to a spectral filtering stage consisting of a Fabry-Pérot cavity (from *Quantaser*, spectral width:  $\sim 100$  MHz linewidth, FSR  $\sim 20$  GHz) and a reflective volume Bragg grating filter (from *Optigrate*) with a  $\sim 0.1$  nm filtering window. Altogether, the total background counts is reduced from about 50 photons/s without to around  $< 300$  photons/s.

After most of the filtering, the light is sent onto a Hanbury-Brown-Twiss setup that consists of a beam splitter with a single photon counting module (SPCM) in each output. The light after the beam-splitter is coupled into a multimode fiber and then guided to the SPCM. Before each fiber, we place a 852 nm bandpass filter (LL01-852-25 Semrock Maxline) with  $\sim 3.5$  nm transmission window to block any spurious photons from light emission during photon detection

in the avalanche silicon photodiodes in the SPCMs (*Excellitas*, spcm-aqrh-15). The SPCMs are connected to a field-gate programmable array (FPGA) based time tagger which records the photon detection events with a timing resolution of better than one nanosecond. We make sure that the cable lengths and the optical path lengths are the same in both arms so as to avoid introducing any time delay in one of the arms. A self written program records the time stamps of every single count registered by the SPCMs and stores this data automatically after every half an hour of experimental run.

### 5.1.2 Experimental Sequence

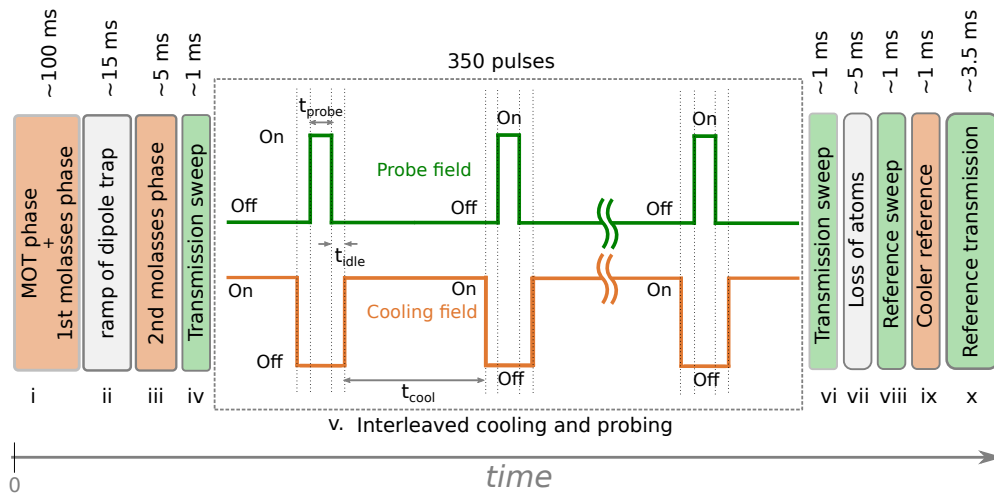


Figure 5.2: Experimental sequence for the correlated photons measurement. The various steps of the experiment are represented by boxes numbered from i to x, and the duration of the steps mentioned above the boxes. In step (i), we laser cool the Cs atoms (MOT) and load them into the trapping sites (molasses). Then we bring the atoms slightly closer to the nanofiber surface by gradually ramping up the power of the red-detuned trap laser in step (ii). The second molasses in step (iii) is to cool the atoms remaining in the trap, before measuring the transmission spectrum in step (iv). The main part of the experiment is carried out in step (v), where we do cooling and then resonant probing of the atoms 350 times ( $t_{cool}, t_{probe}, t_{idle} = 200 \mu s, 10 \mu s, 5 \mu s$ ). After the experiment, we measure the transmission spectrum with remaining atoms (step (vi)), and without any atoms (step (viii)). Step (ix) and (x) are used for measuring the photon clicks due to the cooling beam scattered into the nanofiber via the impurities in the nanofiber waist and due to the resonant probing pulse in absence of any atoms respectively.

The step-wise timeline of one single run of the experiment is shown in figure 5.2. A single run comprises of three main stages: preparation and characterization of the atomic ensemble before and after the run (steps i-iv, vi-viii), interleaved cooling and probing (step v) and reference measurements (steps ix and x). The details of the three stages of the experiment are described in the following subsections. This experimental sequence, with a single run duration of  $\sim 300$  ms,

was repeated over a period of over 8 days and consists of in total around 2.5 million runs.

### 5.1.2.1 Ensemble preparation

The ensemble preparation and characterization is done in step (i -iv) of the experiment sequence shown in Figure 5.2.

**(i) MOT and molasses:** In this step, the atoms are loaded into the optical dipole trap from a cigar-shaped cloud of cold Cs atoms. The atom cloud is created using a magneto-optical trap (MOT) with elongated magnetic coils. The MOT is followed by a molasses cooling stage where the atoms are cooled down to sub-Doppler temperature and loaded into the trap.

**(ii) Ramp of the dipole trap depth:** After the first molasses, the cooling light field and the MOT magnetic fields are turned off, and the red-trap power is adiabatically ramped up over a time of  $15 \mu\text{s}$ . During this time, the cold cloud of untrapped atoms from step (i) of the sequence expands and falls down leaving only the trapped atoms around the fiber. The adiabatic ramp-up of the red trap power moves the potential minimum of the trap closer to the fiber surface. This leads to a better overlap between the evanescent field of the nanofiber-guided probe field and the atomic scattering cross section, thereby increasing the coupling strength. To prepare different atom numbers, we change the time duration of the adiabatic ramp. As our trapping duration is 6 ms, changing the ramping time, thus, allows us to obtain different number of trapped atoms in the ensemble at the end of the ramp.

**(iii) Second molasses:** After the power ramp, a second molasses phase cools the remaining trapped atoms. This is necessary to compensate for the heating during the ramp which would otherwise lead to a larger distance of the atoms from the fiber surface due to the anharmonicity of the trap.

**(iv) Transmission sweep:** To measure the OD of the ensemble at this point we record the transmission ( $\bar{C}_{\text{atoms}}(\delta)$ ) of the probe field as a function of the probe detuning, as indicated by step (iv). Using equation 3.4, we infer the OD in conjunction with the reference and by measurements in step (viii) and (x), where we measure  $\bar{C}_{\text{without atoms}}(\delta)$  and  $\bar{C}_{\text{bkg}}$  respectively.

### 5.1.2.2 Interleaved probing:

The time duration of the resonant probing of the atomic ensemble is limited by the heating of the atoms in the trap which results in a reduction of the average coupling strength over time. However, to get enough statistics in the limit of weakly saturating probing light field and for large optical depths, one needs to probe the atomic ensemble for a sufficiently long duration. Moreover, to make a systematic study of the dependence of photon correlations on the number of atoms, a stable average atom-light coupling strength is required for the entire probing duration. To achieve this, we implement an interleaved probing and cooling sequence discussed in

the following.

**Probe pulse power and duration:** The probe light field is resonant with the D2 ( $6S_{1/2}, F = 4 \rightarrow 6P_{3/2}, F' = 5$ ) transition and launched as a travelling wave into the nanofiber. It is quasi-linearly polarised with the transverse polarization in the plane of the trapped atoms, i.e., it coincides with that of the red-detuned trapping light fields. For our trapped atoms the probe power used, is about  $\sim 2.35$  pW, which corresponds to an on-resonance saturation parameter of  $s_0 = 0.02$  for the first trapped atom. At this power, the atoms scatter  $R = s_0/(1 + s_0) \cdot (\Gamma/2) \approx 0.65$  photons per microsecond, where we assumed  $\Gamma = 2\pi \times 5.22$  MHz for the Cs D2-line cycling transition [59]. In order to keep the momentum transfer to the atoms due to the photon recoil small, we limit the probing duration to  $10 \mu\text{s}$ . For this duration, the first atom will scatter around  $n_{sc} = 7$  photons. As the probe duration is comparable to the oscillation period of the atoms in the trap, we now make the constant case assumption that all the recoil momenta add up along the same direction. In this case, the atom will acquire an additional kinetic energy given by  $E = (n\hbar k)^2/2m_{Cs} = n^2 E_r$ , where  $E_r = 0.2 \mu\text{K}$  is the recoil energy for Cs [59]. For 7 scattering events, the total increase of energy or the heating is roughly  $\sim 7^2 \times E_r = 10 \mu\text{K}$  which is far less than the trap depth of  $\sim 100 \mu\text{K}$  (see Fig 5.3). Longer probe durations should be avoided as the atoms will quickly heat up and due to anharmonic trapping potential the average atom-fiber distance would increase. Hence, a longer probing duration will progressively lower the coupling strength.

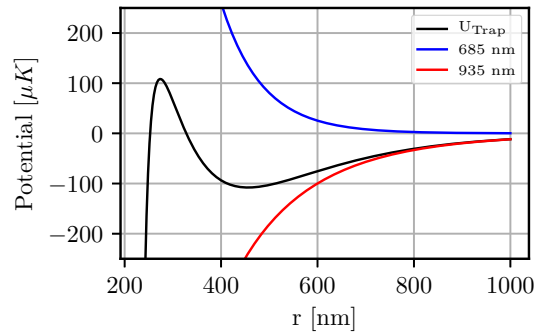


Figure 5.3: The potential (black line) of the two-color dipole trap as a function of the radial distance from the nanofiber axis. For our experimental parameters we obtain a trap-depth of  $\sim 100 \mu\text{K}$ . The red and blue lines denote the attractive and repulsive optical potential generated from the red- and blue-detuned trapping light fields (935 nm and 685 nm) respectively.

**Cooling pulse:** To compensate the residual heating during the  $10 \mu\text{s}$  of probing, we incorporated a molasses cooling pulse with a duration of  $200 \mu\text{s}$  after every probing pulse. In lieu of the rise time of the AOM pulses and the timing resolution available to us from the experimental control, we separated the probe pulse from the cooling pulse by an idle time of  $5 \mu\text{s}$ . We used 350 resonant probe pulse interleaved with molasses cooling pulses. An exemplary SPCM trace is shown in Fig 5.4(a) to elucidate the time separation. In order to select the duration of cooling

pulse which allows us to maintain a constant optical depth of the ensemble during the interleaved probing sequence, we varied the number of probing and cooling pulses for different a given duration of cooling pulse. Measuring the OD before and after the pulse sequence, we found that for a cooling pulse duration of  $200 \mu\text{s}$  the OD was approximately constant. Fig 5.4(b) shows the result. We see that over a duration of 350 probing and cooling pulses, the OD of the atomic ensemble remained constant. Constant OD implies uniform transmission across all the probing pulses throughout the interleaved cooling and probing. This allows us to sort the correlations in the transmitted photons according to the OD extracted from the transmission.

**Region of interest during resonant probing:** We want to remove effects of transient rise and fall of the transmission at the beginning and end of each probe pulse, originating, e.g., from the finite rise and fall time of the acousto-optical modulator that controls the optical pulse. Such rising edges and power spikes can lead to unnecessary bunching features. Thus, we only consider detection event that fall into the probing interval between  $1 \mu\text{s}$  and  $9 \mu\text{s}$  for each probe pulse into account as shown in the inset of Fig 5.4(a).

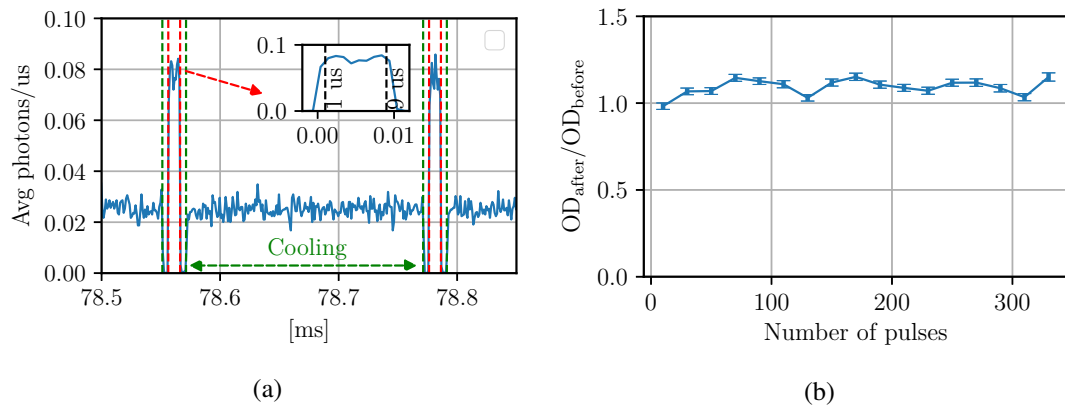


Figure 5.4: (a) Measured photon count rates from one of the SPCMs during part of the interleaved probing sequence averaged over 5000 runs of the experiment. The photon counts in the region between the red dashed lines originate from the transmitted resonant probe pulse whereas the photons in the region between the two green dashed lines originate from atomic fluorescence scattered into the nanofiber from the red-detuned molasses cooling beams. (b) Dependence of the OD, as obtained from the off-resonance transmission, of the atomic ensemble on the pulse number.

**Stable transmission:** Figure 5.5(a) shows transmission per probe pulse with respect to the probing pulse number averaged over  $\sim 5000$  runs for a particular setting. It follows an exponentially decaying profile with a  $1/e$  decay time,  $n_0$ , of around 11 pulses. We attribute the initial high transmission to the scattering induced heating of the atoms in step iv of the experimental sequence where we measure the transmission spectrum of the atomic ensemble. The first few cooling pulses of the interleaved probing sequence allows us to cool the atomic ensemble such

that we are able to attain a steady state with a higher coupling constant. Figure 5.5(b) shows the distribution of the number of cooling pulses ( $n_0$ ) required for the transmission change to reach  $1/e$  of its initial value for all the data sets recorded over 8 days. The orange dashed line shows a Gaussian fit to the distribution with  $\{\mu, \sigma\}$  of  $\{7.5, 2.1\}$  pulses. There could be several reasons for the variation of  $n_0$  which also includes the temperature and humidity changes in the lab. To work with a constant transmission, we ignore the first 20 pulses from each run.

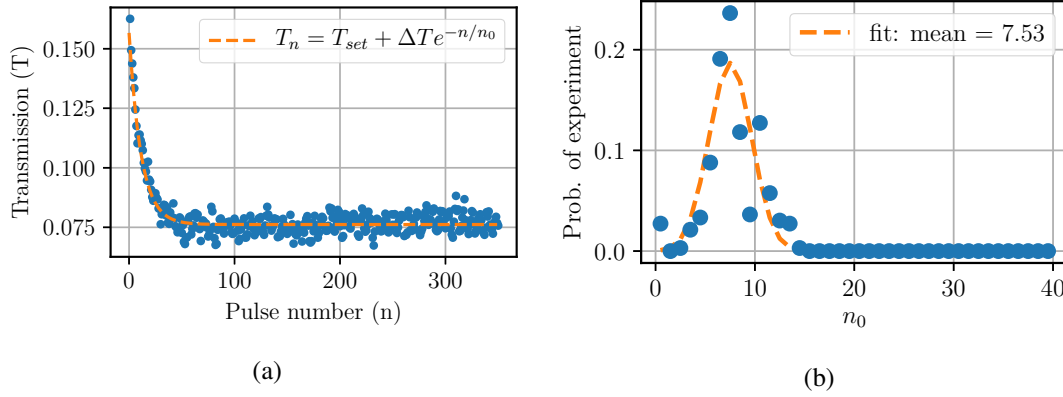


Figure 5.5: (a) Transmission as a function of the number of probing pulses in the interleaved probing sequence. The orange line is an exponential fit where  $T_{set}$  and  $n_0$  are the steady state transmission and  $1/e$  decay constant ( $n_0 = 11$  for this data set) respectively. (b) Histogram of  $1/e$  decay times,  $n_0$ , for all the data recorded over 8 days (2.5 million runs). Each point corresponds to transmission averaging over  $\sim 5000$  experimental runs. Most of the points have a transient transmission time much less than 20 pulses.

### 5.1.2.3 After the interleaved probing

After the interleaved probing sequence we perform the following measurements in each run of the experiment corresponding to steps vi - x of the experimental sequence shown in Figure 5.2).

**(vi) Transmission sweep:** This step is similar to step (iv). We measure the probe transmission ( $\bar{C}_{atoms}(\delta)$  in equation 3.4) through the atomic ensemble as a function of the probe detuning  $\delta$ , from  $\delta \in [-18, 18]$  MHz.

**(vii - viii) Reference measurement for OD measurement:** In step vii of the sequence we turn off the red trap for around 5 ms to remove the atoms from the trap. Then, we scan the probe pulse in frequency (similar to in step iv and vi), but without atoms. Together with (vi) and using this as a reference ( $\bar{C}_{without atoms}$  in equation 3.4) allows us obtain the transmission spectrum of the atomic ensemble and hence estimate the OD as mentioned in section 3.3.2.

**(ix) Reference measurement for cooler:** We record the clicks from the cooler being scattered into the nanofiber in the absence of any atoms. The reason for recording it is as follows. In

the interleaved cooling pulse, the atoms are cooled down using the free space cooling beams from the MOT/Molasses setup. In this process, a fraction of the photons scattered by the atoms are coupled into the nanofiber. Due to their large detuning from the atom resonance ( $\sim -12\Gamma$ ), the photons that are emitted into the guided mode of the nanofiber can propagate freely. Since the number of scattered photons is proportional to the number of atoms, they can serve as an alternative means to estimate the number of atoms. However, the impurities on the fiber surface can also scatter a non-negligible number of photons into the fiber giving rise to a photon background. This background may show some long term fluctuation. Therefore, we record the cooler background without atoms which then allows us to extract number of cooler fluorescence photons scattered into the fiber during the cooling stage which is also proportional to the number of trapped atoms.

**(x) Reference measurement for resonant probe:** In addition to the above reference measurements, we also record the transmission of the resonant probe without atoms for the duration equal to the total integrated duration of probing in the step  $v$  of the experimental sequence ( $= 3.5$  ms). After this step, we also acquire the background counts when all the light fields, except for the dipole trap lasers, are off. This allows us, using equation 3.4 with detuning  $\delta = 0$  to extract the on resonance OD of the atomic ensemble from transmission. The background counts originate from the dark count of the detector plus any residual unfiltered trapping-laser induced Raman scattered photons from the fiber.

### 5.1.3 Estimation of coupling strength ( $\beta$ )

In order to estimate the coupling strength  $\beta$  of a single atom to the waveguide (defined by equation 4.27), we carry out a saturation measurement as described in Ref. [64, 70, 140]. The basic principle of a saturation measurement can be summarized as follows. We assume we have an ensemble of  $N$  atoms that are equally strongly coupled to the nanofiber mode. According to generalized Beer-Lambert law the change in power of light propagating through the fiber along  $z$ - direction over a distance  $dz$  can be written as:

$$dP = -\frac{n(z)\sigma_0/A_{eff}}{1 + P(z)/P_{sat}}P(z)dz \quad (5.1)$$

where,  $n(z)$  is the local atom number density such that  $\int n(z) = N$  gives the total number of atoms,  $\sigma_0 = \hbar\omega\Gamma/2I_{sat}$  is the effective on-resonance scattering cross section of the atoms, and  $P_{sat} = I_{sat}A_{eff} = \hbar\omega\Gamma/8\beta$  is the saturation power. Separating the variables into  $P(z)$  and  $n(z)$  and integrating on both sides we get:

$$\begin{aligned} \int_{P_{in}}^{P_{out}} \left( \frac{1}{P(z)} + \frac{1}{P_{sat}} \right) dP(z) &= - \int_0^L \frac{n(z)\sigma_0}{A_{eff}} dz \\ \ln \left( \frac{P_{out}}{P_{in}} \right) + \frac{P_{out} - P_{in}}{P_{sat}} &= - \frac{N\sigma_0}{A_{eff}} \end{aligned} \quad (5.2)$$



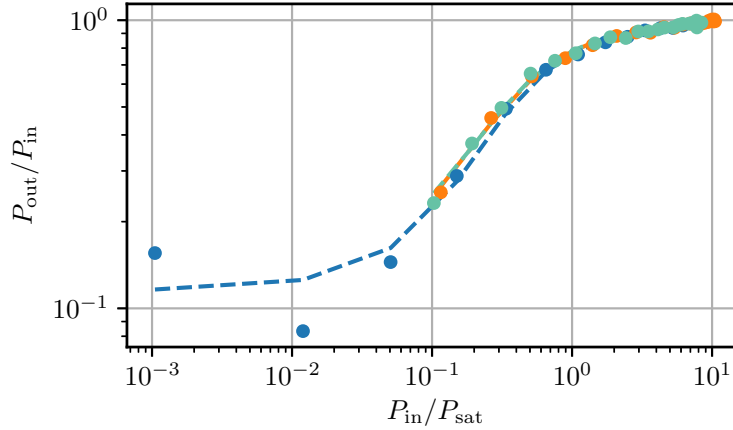


Figure 5.6: Saturation measurement: The graph shows the power transmission as a function of the input power (x-axis) in terms of the saturation power  $P_{\text{sat}}$  for three different atomic ensembles but with the same trap configuration. The dashed line shows the fit according to the modified Beer-Lambert's law as discussed in section 5.1.3. The estimated atom numbers corresponding to the colors blue, orange and green are  $N = \{60, 61, 66\} \pm 3$  atoms. The average coupling strength was obtained to be  $\beta = 0.83\% \pm 0.03\%$ .

Substituting,  $T = P_{\text{out}}/P_{\text{in}}$  (equivalent to transmission), and  $s_0 = P_{\text{in}}/P_{\text{sat}}$  (equivalent of on-resonance saturation parameter), the above equation can be expressed as:

$$\ln(T) + s_0(T - 1) + c = 0 \quad (5.3)$$

and has the solution  $T = W[s_0 e^{(s_0 - c)}]/s_0$ , where  $W[\dots]$  represents the *Lambert W* function and  $c = N\sigma_0/A_{\text{eff}}$ . In the limit,  $s_0 \rightarrow 0$ , equation 5.3 gives,  $c = -\ln(T)$ , which by definition is the optical depth. Using the definition of optical depth from equation 4.29, we get  $c = -\ln[T] = 4N\beta$ . Therefore, one can rewrite equation 5.3 as

$$T = \frac{W[s_0 e^{(s_0 - 4N\beta)}]}{s_0} \quad (5.4)$$

To extract the coupling strength ( $\beta$ ), we record  $T$  as a function of  $s_0$  and fit the data points using equation 5.4 using  $N$  and  $\beta$  as the fit parameter. For this, we prepare an optical ensemble as described in section 5.1.2.1 using a MOT and molasses phase followed by a ramp up of the dipole-trap field and a second molasses. Then, we measure the transmission of a resonant probe pulse of duration of  $10 \mu\text{s}$  for different powers of the probe pulse. For the trap configuration used in this chapter, we obtain an average value of  $\beta = 0.0083 \pm 0.0003$  from three different saturation measurements with different atom numbers. The data from one of the saturation measurements is shown in Figure 5.6.

## 5.2 Data processing

For the data used in the following, the experiment ran over a total of 8 days. The photon arrival times were saved into a file every half an hour. Parameters such as optical depth, laser powers and frequency were continuously monitored. A field gate programmable array based fast electronic time-tagger records the time stamps of the photons detected by the two SPCMs at the output of the nanofiber. Using these timetags we are able to calculate the transmission and cross-correlations.

### 5.2.1 Sorting runs based on OD from transmission

As we saw in 5.1.2.2, the transmission of the atomic ensemble during the resonant pulsing in step (v) gives us the OD of the atomic ensemble. Alternatively, the OD could also be measured from step (iv) and (vi), which is however not a reliable measure of OD in a single shot because of two reasons. First, the probe-induced heating caused during this step modifies the OD the ensemble. Secondly, due to low probe powers the transmission spectrum is very noisy and two fit parameters: OD and  $\Gamma$  (see equation 3.4) are susceptible to photon shot noise. Therefore, for a single shot measurement of the on-resonance optical depth, we choose the average transmission during the resonant probing as means to infer the OD.

**Calculating transmission:** For every run we count all the timestamps during the region of interest from all but first 20 pulse. We represent this set as  $N_p^{\text{meas}}$ , where the subscript stands for probe photons. From the reference probe pulse (without atoms), we calculate the number of photon clicks expected in the effective probing duration. We call this  $N_r^{\text{meas}}$ , where the subscript stands for reference pulse. We calculate the OD in a single run as:

$$OD = -\ln[T] = -\ln\left[\frac{N_p^{\text{meas}}}{N_r^{\text{meas}}}\right] \quad (5.5)$$

Fig 5.7 shows the distribution of photon counts acquired during each experimental run (left) and the corresponding distribution of ODs acquired (right) from all 2.5 million runs of the experiment.

**Binning the OD:** For our purpose, we sort the runs according to their OD using a binsize of 0.1, 0.25 and 0.5 for ODs in the lying in the intervals  $[0, 4.0]$ ,  $[4, 5]$  and  $[5, 8]$ , respectively. For larger ODs, we increased the binsize so as to compensate for the reduced signal to noise ratio in transmission at higher ODs. For the same reason, we require more number of experimental runs at larger OD as seen in the figure 5.7 (right).

**Uncertainty in OD:** The OD calculated from the transmission using equation 5.6 has an uncertainty because of the shot noise associated with photon counting. Because of this, the data sorted based on this OD corresponds to an uncertainty range larger than the OD bin size defined. Here we estimate this uncertainty in terms of the OD as well as in terms of atom number given a value for the coupling strength  $\beta$ .

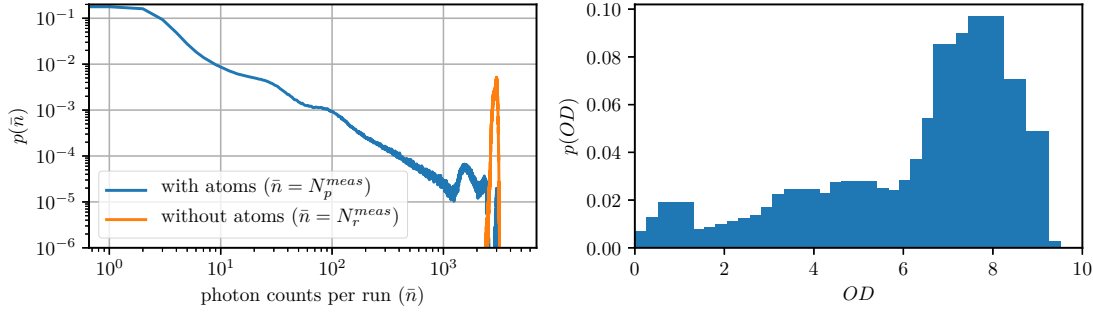


Figure 5.7: Measurement statistics: (a) Histogram of the number of photons transmitted in a single run for the probe beam during the probing interval with atoms (blue) and without atoms (orange). (b) Distribution of ODs during all the experimental runs.

We start with the fact that OD and the number of atoms in the ensemble,  $N_a$ , is linearly related for small  $\beta$  (see equation 4.29) as:

$$N_a = \frac{OD}{4\beta} = -\frac{1}{4\beta} \ln \frac{N_p}{N_r} \quad (5.6)$$

where,  $N_p$  and  $N_r$  are the number of photons in the probing and reference pulse. If  $\mathbf{N}_a$  denotes the set of all atom numbers that correspond to a given OD bin  $[OD_a, OD_b]$ , then assuming a given  $\beta$ ,

$$\mathbf{N}_a = \{ N_a : (OD_a/4\beta) \leq N_a < (OD_b/4\beta), N_a \in \mathbb{Z} \} \quad (5.7)$$

The photon and atom numbers are integers. For a given atom number,  $N_a \in \mathbf{N}_a$ , and input photons,  $N_r$ , the subset of transmitted photon counts,  $\mathbf{N}_p$ , can be obtained as:

$$\mathbf{N}_p = \left\{ N_p \in \mathbb{Z} : N_r e^{4\beta(N_a-1)} \geq N_p > N_r e^{4\beta N_a} \right\} \quad (5.8)$$

Having defined the notations, our target is to calculate the uncertainty in the atom number distribution realized in the experiment, given the reference photons count,  $N_r^{\text{meas}}$ , and the transmitted probe photon counts,  $N_p^{\text{meas}}$ , as measured in the experiment. The probability of observing a certain transmitted probe photon count depends on the measured photon distribution as:

$$\begin{aligned} p(N_p) &= \sum_{\mathbf{N}_p^{\text{meas}}} p(N_p | N_p^{\text{meas}}) p(N_p^{\text{meas}}) \\ &= \sum_{\mathbf{N}_p^{\text{meas}}} \frac{(N_p)^{N_p^{\text{meas}}} e^{-N_p}}{(N_p^{\text{meas}})!} p(N_p^{\text{meas}}) \end{aligned} \quad (5.9)$$

where,  $p(N_p^{\text{meas}})$  is the measured probability distribution as shown in blue in Figure 5.7(a) and  $p(N_p | N_p^{\text{meas}})$  is the probability of observing  $N_p$  photons when  $N_p^{\text{meas}}$  photons were present.

This arises due to the Poissonian shot noise associated with photon counting [141]. The probability  $p(N_r)$  can also be expressed similarly. However, in our case the mean reference count is high enough ( $\langle N_r \rangle \sim 4000$ ) such that the signal to noise ( $\sim \langle N_r \rangle / \sqrt{\langle N_r \rangle} \gg 1$ ) is much greater than one. Therefore, we ignore the noise in the reference pulse and use the  $p(N_r) = p(N_r^{\text{meas}})$  which is represented by the orange curve in Figure 5.7.

Summing up over all measured combinations of reference and transmitted probe photon counts, we can find the probability of realizing a certain atom number in our experiment as:

$$p(N_a) = \sum_{N_r \in \mathbf{N}_r^{\text{meas}}} p(N_r) \sum_{N_p \in \mathbf{N}_p} p(N_p) \quad (5.10)$$

Substituting equation 5.9 into equation 5.10 one can obtain the probability distribution of each atom number corresponding to the OD bin as realized by the experiment. For this distribution of  $\{\mathbf{N}_a, p(\mathbf{N}_a)\}$ , we find the mean and variance as  $\bar{N}_a$  and  $\Delta N_a$ . The error bar in the OD measurement for a given bin corresponds to the variance of the underlying atom number distribution and hence is expressed as  $\Delta OD = 4 \cdot \beta \cdot \sqrt{\langle \Delta N_a^2 \rangle}$ .

## 5.2.2 Obtaining normalized second order correlations

In the following section, we shall see how to extract the second order correlation,  $g^{(2)}(\tau)$  from the coincidences in photon detection events at the output of the nanofiber.

### 5.2.2.1 Obtaining the coincidence histogram, $(C(\tau))$

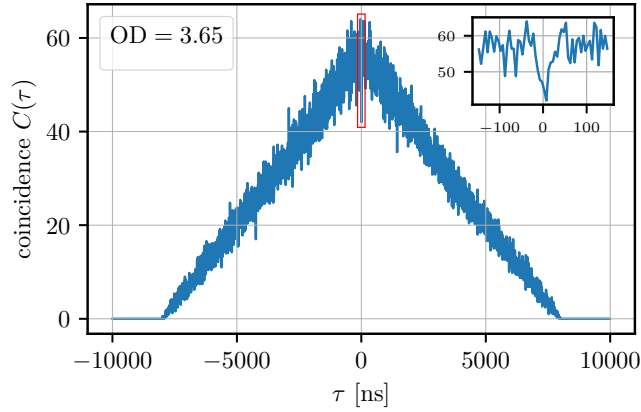


Figure 5.8: An exemplary coincidence histogram recorded for OD = 3.15. The  $y$ -axis shows the number of coincidences  $C(\tau)$  at time delay  $\tau$ . The triangular shape originates from the finite probing duration of  $8 \mu\text{s}$  which gives  $[-8\mu\text{s}, 8\mu\text{s}]$  as the possible range of  $\tau$ . For displaying purpose, the time bin size has been adjusted to 5 ns. The inset shows a zoom of the region corresponding to the red rectangle in the center.

Based on the sorting criteria mentioned in the section 5.2.1 above we obtain the correlations for different optical depths. For every run, we select all the timestamps recorded during the region of interest from all the 330 probe pulses (see section 5.1.2.2). We then histogram all the time differences ( $\Delta t$ ) between the photon detection events in the two detectors to obtain the coincidence histogram for a single run. We use a binsize of 1 ns, which is much shorter than the characteristic time scale of the expected second order correlation function which is on the order of  $\Gamma^{-1} \sim 30$  ns. Based on the OD of the atomic ensemble for the run considered, we sort and accumulate the coincidences from each run into one out of 54 such histograms,  $C(\tau)$ .

### 5.2.2.2 Normalization

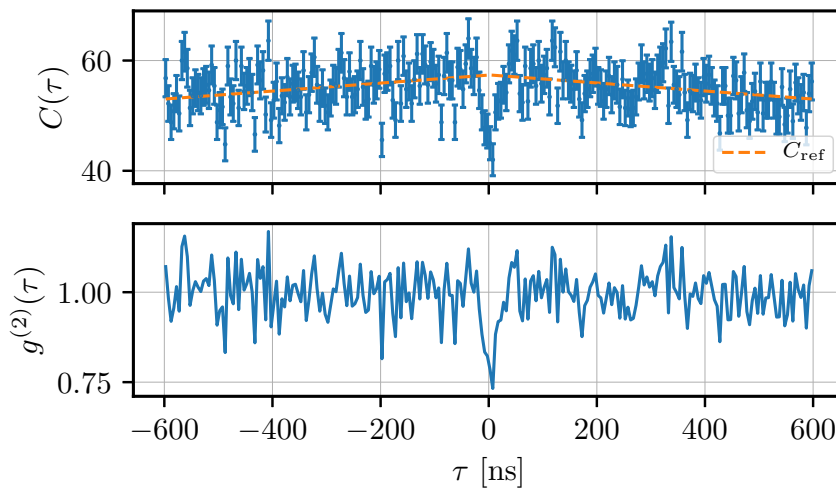


Figure 5.9: Obtaining  $g^{(2)}(\tau)$  from the coincidence histogram: The top panel shows the coincidence histogram ( $C(\tau)$ , blue) for OD = 3.15 and the corresponding reference histogram ( $C_{\text{ref}}(\tau)$ , orange). The  $y$ -axis shows the number of coincidences at time delay  $\tau$ . The bottom panel shows the corresponding  $g^{(2)}(\tau)$ . The time bin size used for displaying the data is 5 ns.

The atoms introduce the correlations between otherwise uncorrelated photons if the time delay between the photons,  $\tau \ll \Gamma^{-1}$  [51] Therefore, correlations recorded for large time delays is essentially equivalent to that of the coherent state and can serve as a reference for obtaining the  $g^{(2)}(\tau)$ . We obtain this reference by fitting the coincidence histogram,  $C(\tau \gg \Gamma^{-1})$  to an inverted symmetric triangle,  $C_{\text{ref}}(\tau) = (m|\tau| + c)$ , where  $m$  and  $c$  refer to the slope and intercept of the triangle. The inverted triangular shape is due to the finite duration of the rectangular pulse with which we probe the ensemble. Since two photons from the same pulse cannot be separated by more than the pulse duration, therefore this triangle approaches zero as shown in Figure 5.8. The corresponding  $g^{(2)}(\tau)$  is obtained as  $C(\tau)/C_{\text{ref}}(\tau)$ . To find  $\{m, c\}$  for the  $C_{\text{ref}}(\tau)$  from  $C(\tau)$ , we first define a range  $|\tau| \in [200 \text{ ns}, 600 \text{ ns}]$ , which is much greater than  $\Gamma^{-1}$ , but sufficiently smaller than the time scales of some other mechanisms such as optical pumping of the atomic ensemble which we ignore. The normalized second order correlations for all the 54

coincidence histogram for the different ODs is shown in Figure 5.13. The Appendix B shows the coincidence histogram,  $C(\tau)$  for all the OD bins side-by-side with the normalized second order correlations as obtained by the procedure described in this section.

### 5.2.3 Estimating $g^{(2)}(0)$ from coincidence histograms

From our discussion in chapter 4, we are interested in analyzing the change in  $g^{(2)}(0)$  with optical depth. Due to low counts, especially at higher optical depths, the measured value of  $g^{(2)}(0)$  is susceptible to noise. Therefore, we adopt a heuristic fit function which reasonably approximates the shape of our  $g^{(2)}(\tau)$  for small delays,  $\tau \lesssim \Gamma^{-1}$ , where  $\Gamma$  is the excited state linewidth. Based on the fact that the transmission spectrum has a Lorentzian shape [142], which in the time domain transforms to a decaying exponential, we can write:

$$g^{(2)}(|\tau|) \approx K(1 + Ae^{-|\tau|/\tau_0}) \quad \text{for } |\tau| \lesssim \Gamma^{-1} \quad (5.11)$$

where,  $\tau_0$ ,  $A$ , and  $K$  are the free parameters for the decaying exponential. The ratio  $A$  and  $\tau_0$  determine the shape of the correlations. Since the expected correlation function is symmetric,  $g^{(2)}(-\tau) = g^{(2)}(\tau)$ , we perform analysis on the folded coincidence histogram  $C(|\tau|) \stackrel{\text{def}}{=} C(\tau) + C(-\tau)$ . For completeness, Figure 5.10 shows the triangular fit (dashed orange lines) to the folded coincidence histogram (blue). The observed coincidence counts scales the reference,  $C_{\text{ref}}$ , as:

$$C_{\text{model}}(|\tau|) = C_{\text{ref}}K(1 + Ae^{-|\tau|/\tau_0}), \quad \text{if } \tau \lesssim \Gamma^{-1} \quad (5.12)$$

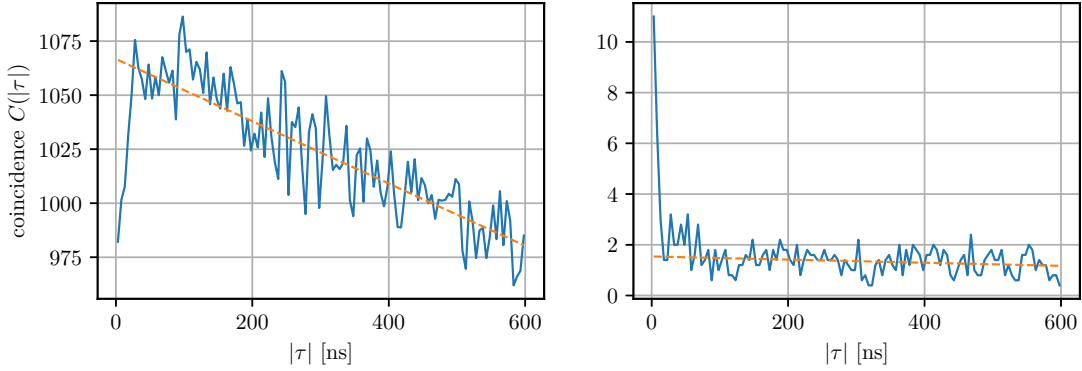


Figure 5.10: Example of fitting the folded histogram  $C(|\tau|)$  (blue) for two different ODs (left: 2.15, right: 7.25), to a line,  $C(|\tau|) = m|\tau| + c$ , (orange) in the region [200 ns, 600 ns], where  $\{m, c\}$  are the fit parameters. The time bin size used for displaying the coincidences is 5 ns.

Next, we need to fit the observed correlation statistics in a small region around zero time delay using equation 5.12. Due to the low coincidence counts for high ODs, the usual least square fitting method is not suited. Instead, we resort to a maximum likelihood estimation (MLE) of  $g^{(2)}(0)$ . In our case, MLE searches for the unknown parameters,  $\Theta = \{A, \tau_0\}$ , of  $C_{\text{model}}(|\tau|)$ ,

which maximizes the total probability to observe the measured coincidence histogram  $C(|\tau|)$ . The probability that a coincidence count that lies in the window  $[0, T]$ , leads to a coincidence click at time delay,  $\tau$ , is given by the probability distribution function

$$\begin{aligned} p(\tau|\Theta) &= \frac{C_{\text{model}}(|\tau|)}{\int_0^T C_{\text{model}}(|\tau|) d\tau} \\ &= \frac{(m|\tau| + c) \times (1 + Ae^{-\tau/\tau_0})}{cT + mT^2/2 + Ac\tau_0 + Am\tau_0^2 - A\tau_0(c + m(T + \tau_0))e^{-(T/\tau_0)}} \end{aligned} \quad (5.13)$$

The probability to obtain  $c_i$  coincidence events at time-bin  $\tau_i$  is given as  $(p(\tau_i, \Theta))^{c_i}$ . The joint probability of obtaining a measured coincidence histogram,  $C(|\tau|)$ , given parameter set  $\Theta$  is defined as the likelihood  $\mathcal{L}[\Theta]$  expressed as

$$\mathcal{L}[\Theta] = \prod_{i=1}^n (p(\tau_i, \Theta))^{C(\tau_i)} \quad (5.14)$$

We vary the parameter set,  $\Theta = \{A, \tau_0\}$ , and try to maximize the likelihood for observing the coincidence histogram,  $C(|\tau|)$ , for a given OD. We do so for all 54 coincidence histograms and find the respective parameters  $\Theta_{\text{fit}} = \{A_{\text{fit}}, \tau_{0\text{fit}}\}$  for which our model best describes the measured coincidence histograms. For larger optical depths where we expect bunching, the approximation in equation 5.11 is valid over a small range. Therefore, we limit the fit region to the characteristic time scale of the expected correlation functions to  $T \approx \Gamma^{-1}/2 \approx 15$  ns for the datasets with  $\text{OD} > 6$  as compared to 30 ns otherwise.

To find the remaining unknown,  $K$ , in equation 5.12, we normalize  $C_{\text{model}}(|\tau|)$  by comparing its integral to the integrated number of coincidences  $C(\tau)$  in the region where the MLE was applied in the previous step. Mathematically this can be expressed as:

$$K = \frac{\int_0^T C(\tau) d\tau}{\int_0^T C_{\text{model}}(\tau | m_{\text{fit}}, c_{\text{fit}}, A_{\text{fit}}, \tau_{0\text{fit}}) d\tau} \quad (5.15)$$

Therefore, corresponding to the coincidence histogram observed for each OD, the respective  $g^{(2)}(0) = K(1 + A_{\text{fit}})$  as given by equation 5.11.

**Error estimation of  $g^{(2)}(0)$ :** We estimate the error in the value of  $g^{(2)}(0)$  by means of a bootstrapping method. For each OD in Figure 5.11, we generate 50 artificial coincidence data samples,  $\{C'(\tau)\}$ , with the photon statistics given by  $p(\tau|\Theta = \Theta_{\text{fit}})$ , where  $\Theta_{\text{fit}}$  is the parameter set  $[A_{\text{fit}}, \tau_{0\text{fit}}]$  of the MLE fit which maximizes the likelihood of observing the experimentally recorded coincidences for that OD. For each of these samples generated, we again perform a MLE which yields the new fit result  $[A'_{\text{fit}}, \tau'_{0\text{fit}}]$ . We also perform the normalization (step 4) and obtain the  $K'$  for each sample. From the set of  $\{A'_{\text{fit}}, K'\}$ , one can find the estimates of  $g^{(2)}(0)$  as  $g' = K'(1 + A'_{\text{fit}})$ . The standard deviation of the resulting distribution of  $g'$  is then used as an estimation of the error in  $g^{(2)}(0)$ . Fig. 5.11 shows the value of  $g^{(2)}(0)$  (blue) and its standard deviation obtained in this way for each OD bin.

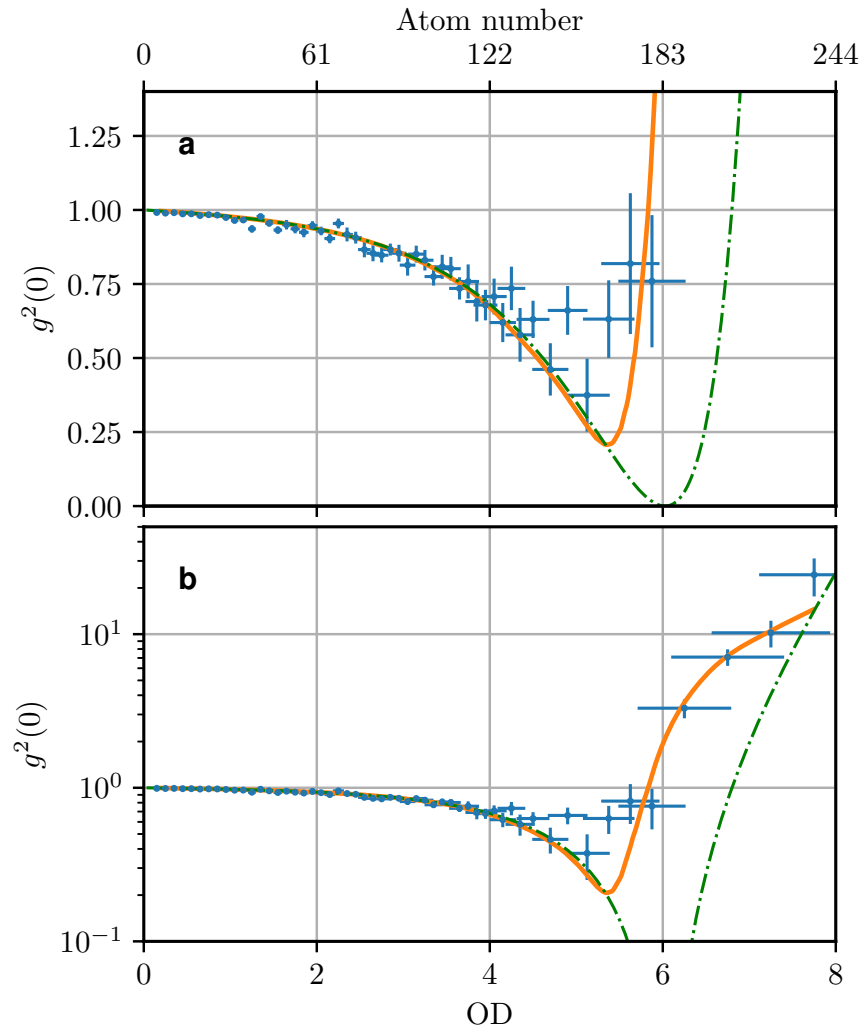


**Figure 5.11: Correlations at zero time delay vs. number of trapped atoms** The blue data points show the zero time delay value  $g^2(0)$  of the measured second order correlation functions as a function of the optical depth of the atomic ensemble (lower x-axis) or average number of trapped atoms (upper x-axis). For better visibility, we plot the same data using a linear (**a**) and a logarithmic (**b**) scale for the y-axis. The values  $g^{(2)}(0)$  and their errors are obtained from maximum likelihood fits to the individual correlation functions (see section 5.2.3 for details). The solid red line is the theory prediction taking into account the experimental uncertainty in OD estimation with the coupling strength  $\beta$  as only fit parameter (see section 5.2.4 for details). For comparison, we also show the theory curve without uncertainty in atom number for the same value of  $\beta$  (dashed green curve). The number of trapped atoms on the upper  $x$ -axis is determined from the measured OD using the measured value of  $\beta$ . The error bars in  $x$ -direction indicate the spread in atom numbers that enter in the measured correlation function.



### 5.2.4 Theoretical prediction of $g^{(2)}(0)$ vs OD

In order to understand if the measured dependence of the  $g^{(2)}(0)$  vs OD fits to our theoretical model, we have to use the exact theory to calculate a curve similar to Figure 4.5, taking into account the factors like photon shot noise and uncertainty of atom number (uncertainty of OD, see section 5.2.1). Using this model, we employ a least squared error minimization [143, 144] to obtain the fit parameter,  $\beta$ . As a first step, we precalculate<sup>1</sup> the value of  $g_{\text{exact}}^{(2)}(0, N_a, \beta)$  in the ideal case for different atom numbers ( $N_a \in [1, 2, \dots, 700]$ ) and coupling strengths ( $\beta \in [0.01\%, 0.02\%, \dots, 0.2\%]$ ) using the results from Reference [51]. To calculate the expected  $\beta$ ,  $g_{\text{th,OD}}^{(2)}(0, \beta)$ , we average the ideal case theory over the underlying atom number distribution found in equation 5.10 as

$$g_{\text{th,OD}}^{(2)}(0, \beta) = \sum_{\{N_a\}} g_{\text{exact}}^{(2)}(0, N_a, \beta) \cdot p(N_a) \quad (5.16)$$

where,  $\{N_a\}$  is the set of atoms numbers corresponding to each OD bin taking into account the shot noise in photon counting (see section 5.2.1 for more details). For every  $\beta$ , we calculated,  $\chi^{(2)}(\beta)$ , as:

$$\chi^{(2)}(\beta) = \sum_{OD} \frac{(g_{\text{th,OD}}^{(2)}(0, \beta) - g_{\text{exp,OD}}^{(2)}(0))^2}{(\Delta g_{\text{exp}}^{(2)}(0))^2} \quad (5.17)$$

where the numerator is the difference of the theoretically estimated and experimentally inferred value of  $g^{(2)}(\tau)$  for each OD bin, and the denominator is the error bar for the experimentally inferred value (see previous section 5.2.3). We vary the fit parameter,  $\beta$  so as to minimize the value of the error,  $\chi^{(2)}(\beta)$ , as given by equation 5.17. We obtained the best fit corresponding to  $\beta_{\text{fit}} = 0.82\% \pm 0.02\%$  which corresponds to the orange line in Figure 5.11. This value of coupling strength agrees well with the value obtained via the saturation measurement in section 5.1.3 of  $0.83\% \pm 0.03\%$ . Using  $\beta_{\text{fit}}$ , we now calculate the theory prediction  $g_{\text{th,OD}}^{(2)}(\tau, \beta_{\text{fit}})$  for all OD settings. The corresponding theory curves are shown in orange in Figure 5.13 and Figure 5.12.

## 5.3 Results and Interpretation

Figure 5.11 is the main result of the investigation. It shows the observed variation of  $g^{(2)}(0)$  with respect to increasing optical depth (lower axis) or atom number (upper axis). As expected for low atom numbers, where the photons statistics of the input light remains unmodified and the output second-order correlation function is approximately flat with  $g^{(2)}(0) \approx 1$ . With increase in the average number of atoms, one observes that the  $g^{(2)}(0)$  starts to fall below 1. This originates from the destructive quantum interference of two-photon probability amplitudes of the correlated and uncorrelated parts (see section 4.3.6 and 4.3.7 for theory). Further increasing the OD, one observes that  $g^{(2)}(0)$  decreases further until at an OD of 5.12, for a mean number of atoms of  $\bar{N} = 156$ , it reaches its smallest value of  $g^{(2)}(0) = 0.37 \pm 0.12$ . Ideally, the theory predicts

<sup>1</sup>We thank the authors of Reference [51] for supplying us with the numerical code for the exact theory.

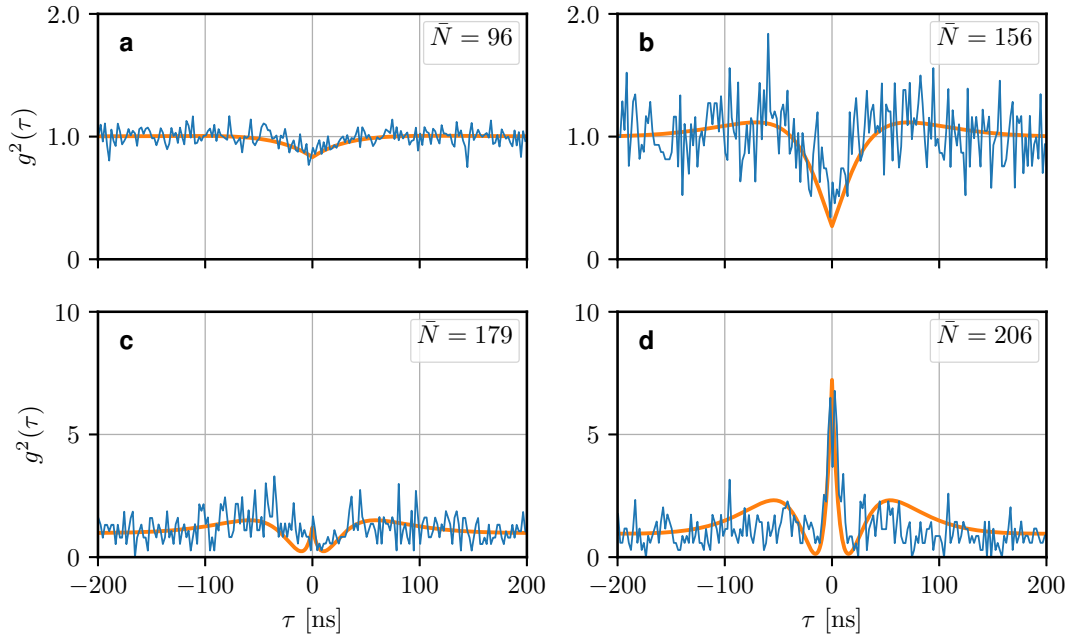


Figure 5.12: A set of four exemplary second-order correlation functions obtained for different optical depths (a) 3.15, (b) 5.13, (c) 5.88, (d) 6.75. The blue lines show the experimental data (with 2 ns binning) whereas the orange line is the theoretical prediction. The four plots help us to see a general trend in the correlations introduced between the photons. For small atom numbers, a:  $\bar{N} = 96$ , we see antibunching. For an increased atom number, b:  $\bar{N} = 156$ , we observe the best antibunching. As the atom number is increase further, c:  $\bar{N} = 179$ , we see a rise of bunching by the peak at  $\tau = 0$ . For large atom number, d:  $\bar{N} = 206$ , we observe a strong photon bunching. The corresponding curves for all the OD bins is shown in Figure 5.13.

that  $g^{(2)}(0)$  should go down to zero, which happens when the ratio of correlated to uncorrelated two-photon amplitude is  $-1$ . However, in the experimental situation, the uncertainty in the atom number distribution leads to an averaging over different atom numbers (see section 5.2.1) and thus we do not reach  $g^{(2)}(0) = 0$ . For even higher mean atom numbers, the correlated photon pairs originating from nonlinear interaction dominate over the transmitted uncorrelated photons, such that  $g^{(2)}(0)$  starts to rise and increases above 1 at around  $\bar{N} \sim 180$  atoms. At extremely high OD, all transmitted photons originate from nonlinear interaction with the atoms, and the bunching increases indefinitely. The highest bunching that we observed is  $g^{(2)}(0) = 24 \pm 6.5$  corresponding to mean atom number of  $\bar{N} = 237$ .

Figure 5.12 shows four exemplary second-order correlations for different regimes of the experiment as discussed above. The blue curve shows the observed  $g^{(2)}(\tau)$  whereas the orange overlay is the theory prediction calculated for  $\beta = \beta_{\text{fit}}$  assuming an atom number variation for the respective bins. Panel (a), which corresponds to an average atom number  $\bar{N} = 96$ , shows weak antibunching as expected for low atom numbers which gradually increase until it becomes

the maximum for  $\bar{N} = 156$  atoms. At this point, one can see an oscillatory behavior of  $g^{(2)}(\tau)$  for larger time delay,  $\tau$  which can be attributed to the frequency difference of the two photons of the correlated two photon component from the laser frequency [145]. In panel (c), one can see a peak near  $\tau = 0$  for a mean atom number of  $\bar{N} = 179$ . Around this point, two-photon pairs start to dominate which changes the output photon statistics to bunching. This photon-bunching becomes stronger going to higher atom numbers. Panel (d) shows an exemplary bunched photon statistics observed at the output for mean atom number,  $\bar{N} = 206$  atoms. Figure 5.13 shows all the normalized second order correlations  $g^{(2)}(\tau)$  (blue) obtained experimentally for the different optical depths. For each OD, the theoretically expected  $g_{th,OD}^{(2)}(\tau, \beta_{\text{fit}})$  (orange) is also shown.

## 5.4 Conclusion and Outlook

The results presented in this chapter show that atomic ensembles can be used to realize strongly correlated many-body states of photons despite weak light-matter coupling and dissipation. In particular, our system enables tuning the second-order correlations of the transmitted light by changing the number of emitters coupled to the light. On one hand, for low atom numbers we observe antibunched photons, while on the other hand, for larger optical depths we observe bunched photons. Both regimes have a range of possible applications, in particular in the realm of quantum information science. Our approach lifts the restriction of having a strong optical driving fields to enhance the optical non-linearity, which have so far been used for generating non-trivial states of light. Our results show that one can collectively enhance [25, 30] the nonlinearities by using an ensemble of emitters weakly coupled to the optical mode of the nanofiber.

Our system offers a novel method for generating antibunched photons. Around the point of lowest antibunching at around  $OD \sim 5.4$ , see orange line in Figure 5.11, we measured an output photon flux of  $\sim 45$  KHz for our input light intensity corresponding to an on-resonance saturation parameter of  $s_0 = 0.02$ . In order to know how far can one increase the flux of antibunched photons and thus to gauge the performance of this new type of source, we calculate the output flux,  $n(s_0, \beta)$  as a function of saturation intensity and  $\beta$ . We compare it against the maximum output flux from a perfect source of antibunched photons, such as spontaneously emitted photons from a single atom. For this, we first determine the configuration,  $\{N_\beta, \beta\}$ , for lowest  $g^{(2)}(0)$  numerically similar to Figure 4.5. We then calculate the transmission  $T_{\{N_\beta, \beta\}}$  for this configuration, up to first order in  $\Gamma/\beta$  using the formalism outlined in [51]. The transmission at the point of best antibunching is plotted against the respective coupling strength in Figure 5.14 in blue and can be approximated well with a fit  $T_{\{N_\beta, \beta\}}^{\text{fit}} \approx \beta^{1.15}$ , for  $\beta < 0.1$ , which is relevant for most systems. For an input power corresponding to,  $s_0 = P_{\text{in}}/P_{\text{sat}}$ , where  $P_{\text{sat}} =$

<sup>2</sup>Since transmission of the input is found up to the first order in  $\Gamma/\beta$ , changing the input power can modify the value of the exponent of the fit  $T_{\{N_\beta, \beta\}}^{\text{fit}}$ . For example, for a different  $s_0 \sim 0.8$ , where the first order approximation still holds,  $T_{\{N_\beta, \beta\}}^{\text{fit}} \approx \beta^{1.17}$ . The fit gives us a conservative estimate on the transmission as can be seen from Figure 5.14.

## 5. OBSERVATION OF CORRELATED PHOTON TRANSPORT IN NANOFIBERS

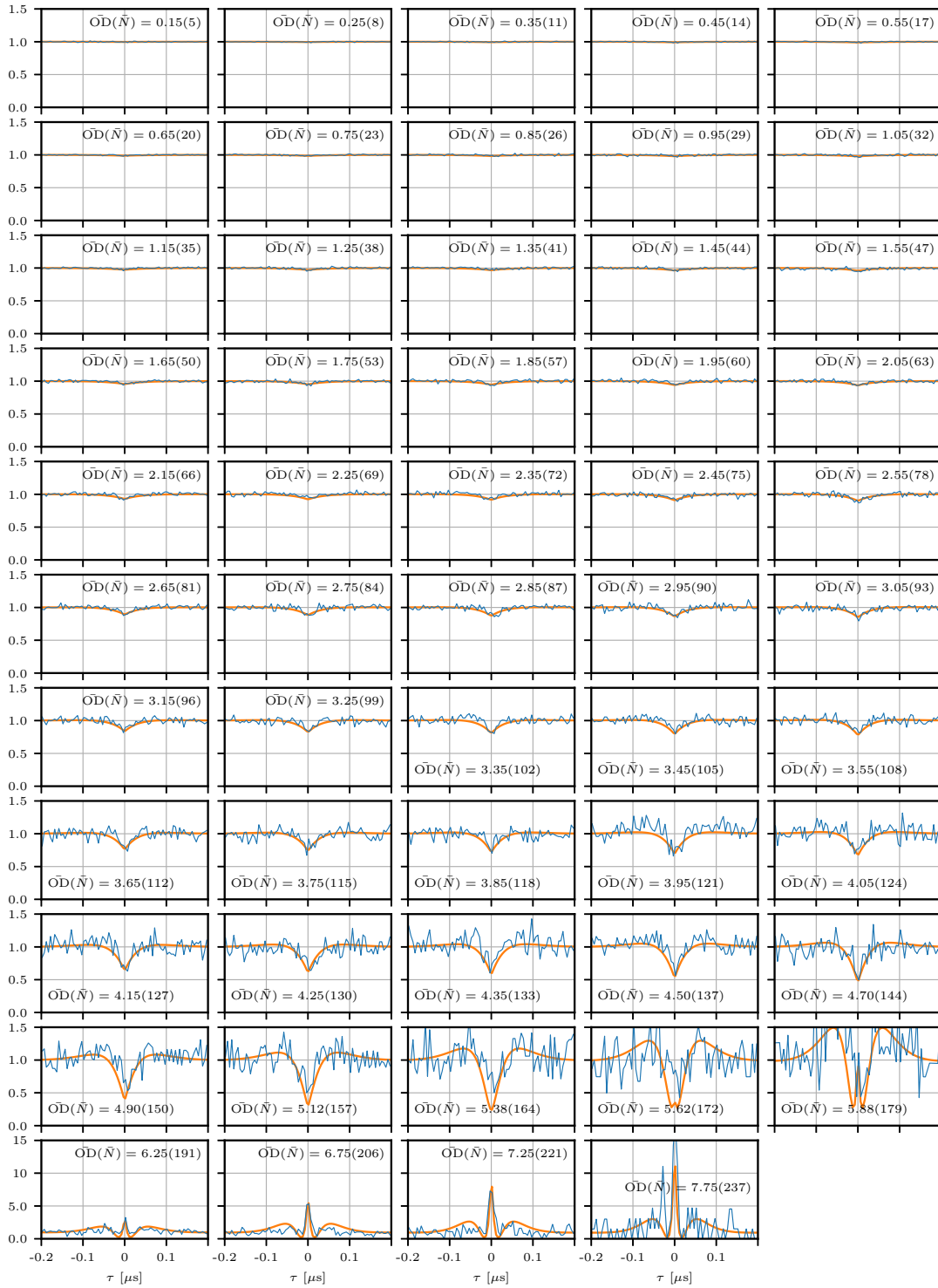


Figure 5.13: Normalized second order correlations,  $g^{(2)}(\tau)$ , (blue) obtained for different average optical depths ( $\overline{OD}$ ) (corresponding mean atom number given by  $\bar{N}$ ) stated in respective panels. The orange line is the theoretically expected curve (see section 5.2.4). The time bin size used for the plot is 5 ns.

$\hbar\omega_0\Gamma/(8\beta)$  is the saturation power, the output photon flux is then given as:

$$n_{\text{out}}(s_0, \beta) = \frac{P_{\text{out}}}{\hbar\omega_0} = \frac{T_{\{N_\beta, \beta\}} \cdot P_{\text{in}}}{\hbar\omega_0} = \frac{T_{\{N_\beta, \beta\}} \cdot s_0 P_{\text{sat}}}{\hbar\omega_0} = \frac{T_{\{N_\beta, \beta\}} s_0 \Gamma}{8\beta} \quad (5.18)$$

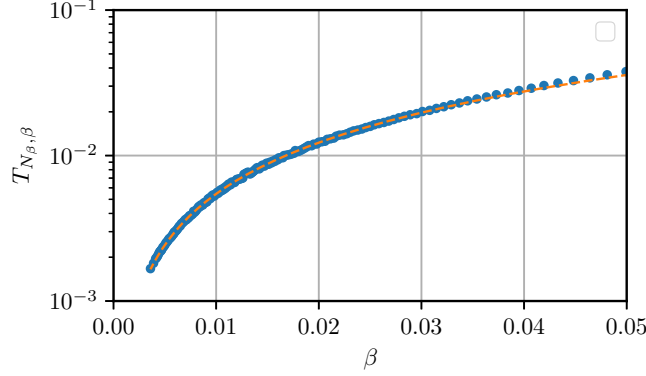


Figure 5.14: Transmission at the point of lowest  $g^{(2)}(0)$  for different values of single atom-photon coupling strength  $\beta$ . The transmission was numerically computed using the expressions from reference [51]. The dashed green line is a fit of the form  $\beta^x$  over the range  $[0.003, 0.03]$ .

For our experiment with parameters  $\{s_0, \beta, \Gamma\} = [2\%, 0.8\%, 2\pi \cdot 5.2\text{MHz}]$ , the above expression gives,  $n_{\text{out}} = s_0\Gamma\beta^{0.15} \approx 39$  KHz, which agrees well with the experimentally observed value. In the ideal case, the best antibunching is expected at around OD of 6, see dashed green line in Figure 5.11, in which case the output rate would be lower. The ratio  $\eta = n(s_0, \beta)/n_{\text{max}} \approx s_0 T_{\{N_\beta, \beta\}}/\beta$  gives a relative figure of merit of our source against a perfect single photon source, where,  $n_{\text{max}} = \Gamma/2$ , is the maximum output photon flux that can in principle be collected from a single emitter source. We plot  $\eta$  in Figure 5.15 as a function of the input power and the single atom-light coupling strength  $\beta$ . Increasing the input power, the output flux of the antibunched photons reaches up to almost 40% of the rate theoretically achievable with a perfectly coupled single atom. In addition, the underlying physics is independent of the type of the emitter or specific optical mode or frequency used and this method can be used for all frequencies spanning the electromagnetic spectrum without the need for controlling the individual emitters and their coupling strengths. These features makes the observed effects highly promising for realizing new sources of nonclassical light, such as single photon sources, in particular for wavelengths where it is not possible to achieve strong coupling of individual atoms or emitters to an optical mode.

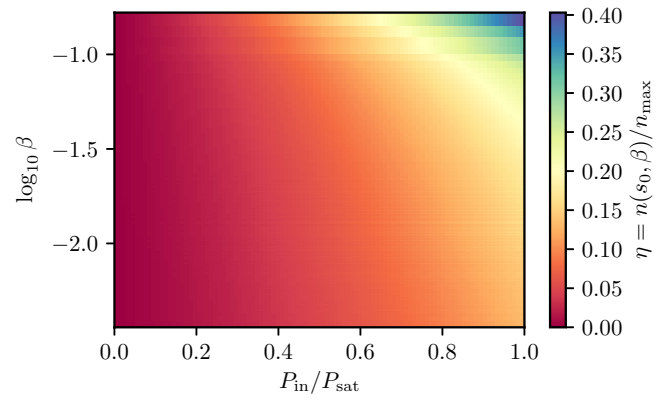


Figure 5.15: Expected photon output at the point of perfect anti-bunching of our scheme as a function of input power and  $\beta$  in units of the maximum photon rate  $\Gamma/2$  achievable with a perfect single emitter source.

# Outlook and conclusion

## 6.1 Summary

In my thesis, the nonlinear photon transport through an array of weakly coupled atomic emitters was studied. For this purpose, we trap neutral Cesium atoms around a sub-wavelength diameter optical glass fiber with a novel experimental setup. I contributed to building the setup from the scratch. In my thesis, some of the key features of our setup have been explained, namely, a large cigar shaped MOT, scalar light shift compensated trapping, highly tunable magnetic-field, good optical access, long nanofiber waist and fiber translation capabilities. I have theoretically described the non-trivial features of light propagation in nanofibers and calculated values of light shifts from the trapping and probing light fields that are used in our experiments. I showed experimental results where we have achieved high optical depths of about 1000 from the nanofiber trapped atomic ensembles despite weak single atom-light coupling. The experimental techniques for generating and characterizing the atomic ensembles were explained.

In the following, I focus on the physics of photon scattering through waveguides coupled weakly to one or many quantum emitters. First, a theoretical foundation is laid for understanding the role of temporal correlations in intensity of a light field. Then, the simplest case of a single photon scattering via a quantum emitter coupled to a waveguide is studied, followed by introduction of the scattering-matrix formalism, with up to two input photons, following which the theoretical results in the limit of many weakly coupled emitters are summarized [51]. Based on the theory, I explain how our system can show a complex interplay between nonlinear processes and dissipation to generate nonclassical photon statistics at the output. In particular, I explain how by changing the number of atoms one can control the ratio of the correlated and uncorrelated two-photon components and how their destructive interference leads to a stream of perfectly anticorrelated photons. Following it, I explained why increasing the number of emitters further leads to photon pairs at the output thereby generating strongly correlated photons.

Following it, I have demonstrated an experimental technique to study such strong photon-photon interactions in a nanofiber-trapped atomic ensemble. First, I explain the experimental setup where we study the output photon correlations via a Hanbury-brown-twiss setup. I explain

in detail the experimental sequence that allow us to prepare an atomic ensemble with varying atom numbers and probe it with a weak coherent field for long enough duration without changing much the single-atom light coupling strength. We sort each run according to the OD and obtain photon coincidence histograms corresponding to 54 different ODs. For each coincidence histogram, the second-order correlation function,  $g^{(2)}(\tau)$ , is calculated and its value at photon time delay of zero is estimated via a maximum likelihood estimation.

Our results confirm strong photon-photon interactions despite the weak single atom-light coupling and the inherent dissipation in the system. It shows in particular that by optimizing the balance between nonlinear and linear transmission (dissipative) one goes from generating anti-bunched photons to bunched photon pairs. From the second-order correlation function for different optical depths, we see that by increasing the atom number we could monotonously decrease the  $g^{(2)}(0)$  until it reached a minimum value. Increasing the number of atoms further we could tune the photon-photon interaction from repulsive to attractive such that the  $g^{(2)}(0)$  increases monotonously as predicted. In our measurements, especially at higher optical depths, we were mostly limited by the background noise of the detection process. Our analysis taking into account the OD averaging and atom-number fluctuations associated with each OD bin shows that the observed crossover in  $g^{(2)}$  from coherent to antibunched to bunched behavior for growing atom number is in very good agreement with the theoretical expectations, and gives convincing evidence for the physics of interacting photons for quantum emitters chirally coupled to a waveguide.

The research presented in my thesis demonstrates a many-body non-equilibrium phenomena that can makes photons interact with the help of just a few weakly coupled atoms. Furthermore, in contrast to other protocols for the generation of non-trivial states of light that rely on strong driving fields to enhance the nonlinear effect, we work in a weak saturation limit but yet see an enhancement of the nonlinearity owing to the collective response of the atoms. Our results show possibility of creating a source of anticorrelated photons with a photon flux comparable to that of a perfectly coupled fully saturated single emitter even in the limit of weak coupling.

## 6.2 Outlook

Having summarized the results, I would like to motivate the readers towards other possible lines of investigation.

### Photon-pair generation and anticorrelated photons

Our setup is in principle capable of generating correlated photons pairs as we saw in section 4.3.6. This is evident from the fact that we get a very high  $g^{(2)}(0)$  for very high optical depths. A possible study would be to herald the single photons and perform a second-order correlation measurement on the heralded photon. Since increasing the number of emitters also correspond to an effective attenuation for the correlated two-photon component, therefore, going to very large optical depths may not be ideal and needs to be investigated. The effect of increasing the input pump power can be investigated as well. Lower pump powers may lower the rate of pair generation. However, higher pump powers might increase the chances of obtaining photon



number states with more than two photons. Therefore, optimum pump power for pair generation needs to be investigated.

As discussed in section 5.4, another obvious line of investigation is to find out the performance of our system as a resource for anticorrelated single photons. It could be investigated if it is possible to increase the flux of anticorrelated photons without compromising the antibunching. A very simple way to do so would be to increase the input power as is also evident from Figure 5.15. A separate line of investigation could be to realize a source of antibunched photons based on a recent proposal [146], where working near the conditions of electromagnetically induced transparency of the nanofiber-trapped Cs atoms can be harnessed to generate a source of antibunched photons. The proposed method can be effective without additional requirement of accurate control of the number of coupled emitters, as was the case for our system.

### Investigating collective effects

**Bragg scattering:** Nanofiber based atom trapping provides by default a periodic array of trapping sites. The scattered light from atoms placed in such a periodical fashion show a well-defined phase relationship which leads to interesting consequences for the guided mode of the fiber [45, 46]. However, the periodicity could also modify the emission of the photons scattered into the radiative modes such that they are preferably emitted in a direction determined by the phase matching condition. Such an effect may provide insights into coupling radiative modes of the atom to the fiber guided mode [147]. To this end, I have presented some preliminary classical simulations in Appendix A, taking into account the realistic fiber, dipolar emission pattern of the trapped atoms and a realistic filling factor of the trapping sites.

**Investigating trapping with counterpropagating blue-trap** The optical setup of the experiment allows one to trap the atoms in a configuration where the periodicity is determined by the blue-detuned standing wave while the red-detuned trapping field is a running wave. By doing so one might be able to trap more atoms as there will be more trapping sites per unit length along the waist. Moreover, this change in separation between the trapped atoms will change the ratio of scattering into the free space to that into the guided modes of the fiber [40]. Such an effect will have applications in increasing the fidelity of storage and retrieval of optical excitations in nanofiber-based atomic ensemble [40, 148]. Therefore, it could be a possibility to investigate trapping using a configuration where the periodicity of the trapping sites is determined by the blue-detuned trap laser.



Die approbierte gedruckte Originalversion dieser Dissertation ist an der TU Wien Bibliothek verfügbar.  
The approved original version of this doctoral thesis is available in print at TU Wien Bibliothek.

# Appendices



Die approbierte gedruckte Originalversion dieser Dissertation ist an der TU Wien Bibliothek verfügbar.  
The approved original version of this doctoral thesis is available in print at TU Wien Bibliothek.

## Bragg Scattering

Nanofiber-trapped atoms have advantageous properties for the implementation of quantum memories for light: One can obtain a very high OD, and the decoherence due to atomic motion and collisions is highly suppressed. This is beneficial for implementations using existing quantum memory protocols. In particular a recently proposed scheme [149] uses engineered subradiant collective states of a periodic array of atoms coupled to a nanofiber. The result is an increase of the storage success probability that scales exponentially with the number of atoms.

A first step towards the implementation of this specialized protocol is to prove that the experimental system supports collective scattering effects. Recently, it was demonstrated that periodic arrays of around 2000 atoms next to a nanofiber can lead to significant reflection of the fiber-guided light [46, 150]. Here, the collective back-scattering of the periodically arranged atoms gave rise to a Bragg resonance. In this case both incoming and outgoing modes are fiber guided, and the reflection is independent of the non-uniformities in the fiber waist. We propose to take these experiments one step further by using the atomic array to couple fiber-guided and free-space modes using a Bragg resonance. In this case, interference of the fields scattered by different atoms should result in a collective emission into a cone with a well-defined angle with respect to the fiber axis. The angle  $\theta$ , enclosed between the wavevector of the emitted light and the fiber axis, is given by the condition for constructive interference,

$$k_0\Lambda \cos \theta + \beta\Lambda = 2\pi \quad (\text{A.1})$$

where  $\beta$  and  $k_0$  are the propagation constants of the probe light in the fiber and in free-space, respectively, and  $\Lambda$  is the distance between the trapping sites. The condition for constructive interference can be easily derived from the illustration in Fig. A.1(b). The relative phase of the light that is scattered out of the fiber by a first atom and a second atom  $\Lambda$  away from the first is given by the sum of two terms in the left hand side of equation A.1. The first term corresponds to the free-space propagation of light under an angle  $\theta$ . The second term describes the propagation of light in the fiber.

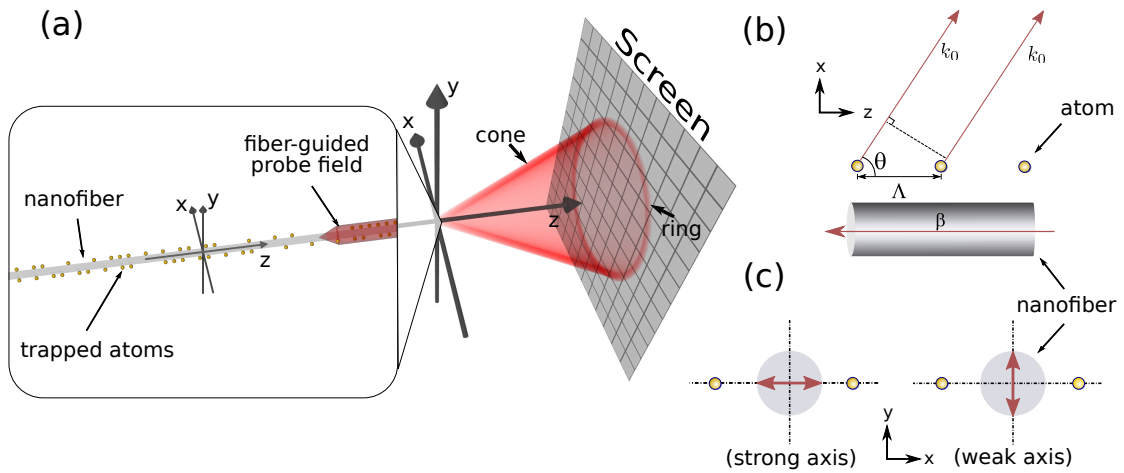


Figure A.1: (a) A sketch of the Bragg cone shows that it will be detected as a circular ring on a screen placed normal to the  $z$ -axis. Moreover, the vertex of the cone opens along  $+z$  direction. The zoom-in shows the atoms trapped in the periodic trapping potential with a certain probability called the filling factor of the trapping sites. (b) A simple scheme demonstrating the interference of light scattered by two atoms (yellow circles) separated by a distance  $\Lambda$ . The light is propagating along  $-z$  direction. (c) Two configurations where probe field is quasilinearly polarized along  $x$  or  $y$  axis, also called strong and weak axis, respectively. Defining the quantization axis along  $y$ , the local polarization experienced by the atoms on the two sides of the fiber is  $\sigma^+$  and  $\sigma^-$  for strong axis configuration. For the weak axis configuration, atoms on both sides of the fiber are  $\pi$  polarized.

## A.1 Simulation

### A.1.1 Analytical calculation of intensity distribution

When equation A.1 is fulfilled, light scattered under angle  $\theta$  interferes constructively. Thus we expect that most of the optical power is concentrated in a cone. Such a cone with respect to the nanofiber is shown in Fig. A.1(a). To be able to better understand the Bragg resonance-mediated coupling of radiative and guided modes, one needs to know the exact spatial distribution of the intensity of the radiated field in the free-space. This involves taking into account several factors such as the lattice constant ( $\Lambda$ ), probing field wavelength ( $\lambda = 2\pi/k_0$ ), variation of the nanofiber radius and the effect of the polarization of the probe field at the position of the atoms. In this section, I will be discussing these factors one by one. Then I will numerically compute the realistic intensity distribution as would be seen on a screen as shown in Fig. A.1(a) placed orthogonally to the nanofiber axis at a macroscopic distance from the atoms.

As a first step, we start with approximating the trapped atoms as point emitters. Assuming a collection of atoms, where the  $j^{\text{th}}$  atom has coordinates  $\vec{r}_j = (x_j, y_j, z_j)$ , the radiated field at a

position  $\vec{r}$  due to the  $j^{\text{th}}$  atom, assuming it to be a pointlike scatterer, is given by:

$$\vec{\mathcal{E}}_j(\vec{r}) = A_j \frac{e^{i(k_0|\vec{R}_j|+\beta z_j)}}{|\vec{R}_j|} \quad (\text{A.2})$$

where  $A_j$  is the amplitude of the electric field at the position,  $\vec{r}_j$ , of the  $j^{\text{th}}$  atom and  $\vec{R}_j = \vec{r} - \vec{r}_j$ , where  $\vec{r}$  denotes the point at which the field is being observed. The intensity due to the scattering on multiple trapped atoms can be obtained as

$$I(\vec{r}) \propto \left| \sum_k \vec{\mathcal{E}}_j(\vec{r}) \right|^2 \quad (\text{A.3})$$

### A.1.2 Array of dipole emitters

In our experimental configuration, the probe field is quasi-linearly polarized such that the transverse linear polarization is either in the trapping plane or perpendicular to it (see 2.2.3). There is an azimuthal asymmetry in the probe field intensity, and the atom-light interaction is the strongest when the probe is quasilinearly polarized in the trapping plane and hence this is called the *strong axis*. For probe polarization being orthogonal to the trapping plane, the local field intensity at the position of the trapped atoms is weaker and hence is called the *weak axis*. For the configuration shown in Fig. A.1, the strong and weak axis corresponds to the probe polarization along  $x$ - and  $y$ - axis, respectively. Along the strong axis, the longitudinal field of the probe is maximum and it is always  $\pm\pi/2$  phase shifted from that along the transverse direction where the negative and positive phase shift correspond to azimuthally opposite sides. For more details on the electric field distribution around the nanofiber see section 2.2.2. For a probe field that is quasi-linearly polarized along the  $x$ -direction, the local polarization of the probe field is approximately  $\sigma_+ = (\hat{x} + i\hat{z})/\sqrt{2}$  for the atoms on one side of fiber, and it is  $\sigma_- = (\hat{x} - i\hat{z})/\sqrt{2}$  for the atoms on the other side. For a probe quasi-linearly polarized along the  $y$ -direction, the polarization for the atoms in the  $x$ - $z$  plane corresponds to  $\pi = \hat{y}$ . Since the dipole emission pattern will be non-isotropic depending upon the local polarization of the probe field, therefore, we must take it into account. Fig. A.2 shows the simulated emission pattern from a single atom which is treated as a spherical wave emitter (left),  $\pi$ -polarized emitter (centre) and  $\sigma_+$ -polarized dipole emitter (right) as seen on a screen placed 10 cm away. One can clearly see the difference in the emission patterns for the three cases. Therefore, for a precise calculation of the spatial intensity distribution of the scattered light, we must consider the dipole emission pattern of all the atoms that contribute to it. This is discussed in the following.

Treating the trapped atoms as dipole emitters with dipole vector  $d_j^\pm$  where subscript  $j$  denotes the  $j^{\text{th}}$  atom, and the superscript + and - refers to the atoms on opposite sides of the nanofiber waist, the resulting electric field at  $\vec{r}$ , due to the  $j^{\text{th}}$  atom at  $r_j$ , can be written as:

$$\vec{\mathcal{E}}_j(\vec{r}) = A_j \frac{e^{i(k_0|\vec{R}_j|+\beta z_j)}}{|\vec{R}_j|^3} (\vec{R}_j \times \vec{d}_j) \times \vec{R}_j \quad (\text{dipole emitter}) \quad (\text{A.4})$$

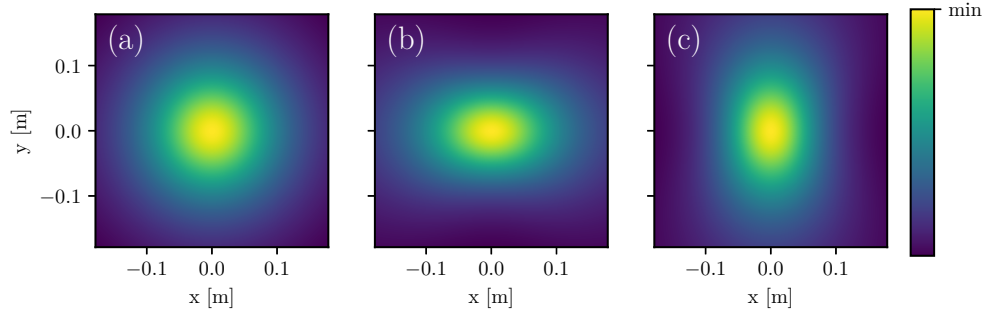


Figure A.2: Simulated isotropic and non-isotropic emission patterns due to a single atom at  $z = 0$  as seen on a screen placed at  $z = -0.1$  m. The atom is treated as (a) a spherical wave emitter, (b) a  $\pi$ -polarized emitter for probe quasilinearly polarized along  $y$ -axis, and (c) a  $\sigma_+$ -polarized dipole emitter for probe quasilinearly polarized along  $x$ -axis.

where,  $\vec{R}_j = \vec{r} - \vec{r}_j$ . As the next step, I calculate using equation A.2, A.3 and A.4, the intensity distribution due to the simplest case of a single array of atoms trapped around a perfect nanofiber with filling factor  $p_F = 1$ . Considering individual atoms of the array as a spherical wave emitter, a  $\pi$ -polarized dipole emitter, and a  $\sigma_+$  polarized emitter, the collective emission pattern as seen on a screen is calculated and shown in Fig. A.3, panels (a-c) respectively. Owing to the symmetry of point like emitters, the resulting pattern is an azimuthally symmetric ring as shown by panel (a). The anisotropy of the dipole emission breaks this symmetry of the ring as shown for  $d_j = \pi$  (panel (b)) and  $d_j = \sigma_+$  (panel (c)). In panel (d) we have used two emitter arrays on diametrically opposite sides of the fiber with dipole polarization  $\sigma_+$  and  $\sigma_-$  respectively as will be the case for probe field along the strong axis.

### A.1.3 Incorporating imperfections

For the results in Fig. A.3 we had assumed an ideal nanofiber waist with uniform radius,  $a$ , of 200 nm. In addition, we had assumed that all the trapping sites were filled with a filling factor  $p_F = 1$  and comprised of an array of spherical wave emitters or dipole scatterers. In this section, we shall have a look at more realistic scenarios corresponding to parameters from our experimental setup.

#### A.1.3.1 Non-uniformities in the fiber

In a realistic scenario, the nanofiber surface is non-uniform as can be extracted from an SEM (scanning electron microscopy) imaging of the nanofiber waist (see Fig. A.4(a)). Due to this, the local propagation constant of the red-detuned trapping field changes according to Equation 2.1 (red line in Fig. A.4(b)) which leads to a change in the periodicity of the lattice as  $\Lambda_n = \pi/\beta_n^{\text{red}}$ . This also changes the propagation constant of the probe (blue line in Fig. A.4(b)). In addition, the resulting change in the intensity distribution in the evanescent field of the nanofiber waist changes the radial trapping potential. Hence the position of the trapped atoms ( $r^{\text{trap}}$ ) is also



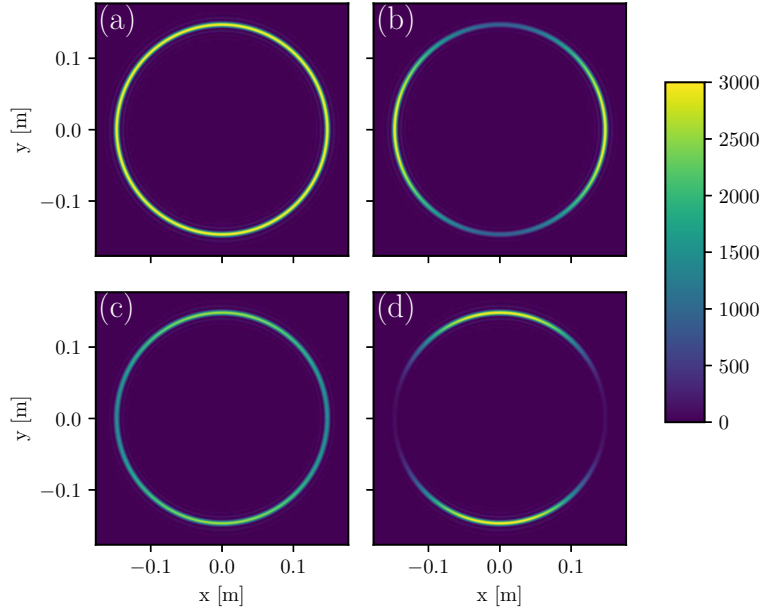


Figure A.3: (a-c) Collective emission pattern for an array consisting of  $N = 100$  atoms on one-side of the nanofiber with filling factor  $p_f = 1$ . Each atom of the array is a (a) spherical emitter (b) dipolar emitter  $\pi$ -polarized (c) dipolar emitter  $\sigma_+$ -polarized. (d) Total of 200 atoms such that there are  $N^+ = N^- = 100$  atoms on each side of the nanofiber which are  $\sigma^+$  and  $\sigma_-$ -polarized respectively. The intensity shown in each panel is normalized to the total number of emitters considered for each case. The screen is located at  $z = -0.1$  m. All atoms are assumed to be 250 nm from the surface of an ideal cylindrical nanofiber with waist radius of 200 nm.

modified. This changes the  $x$ -coordinate of the atoms trapped in the  $x$ - $z$  plane. For incorporating the resulting changes, we re-write equation A.4 and discretize the  $z$ -axis into segments denoted by subscript  $j$  containing only a pair of trapping sites on opposite sides of the fiber as:

$$\beta^{\text{probe}} = \beta_j^{\text{probe}}(a_j) \quad (\text{A.5a})$$

$$x_j^\pm = \pm r_j^{\text{trap}} \cos(\phi_j^{\text{trap}}) \quad (\text{A.5b})$$

$$y_j^\pm = \pm r_j^{\text{trap}} \sin(\phi_j^{\text{trap}}) \quad (\text{A.5c})$$

$$z_j = \sum_{n=1}^{j-1} \Lambda_n = \sum_{n=1}^{j-1} \frac{\pi}{\beta_n^{\text{red}}} \quad (\text{A.5d})$$

where the subscript  $j$  denotes quantities at  $z = z_j$ ,  $a_j$  is the local radius of the fiber, and  $r_j^{\text{trap}}, \phi_j^{\text{trap}}$  are the radial and azimuthal position of the trapping minima. The following subsection explains why the azimuthal position of the trapped atoms may show a local variation.

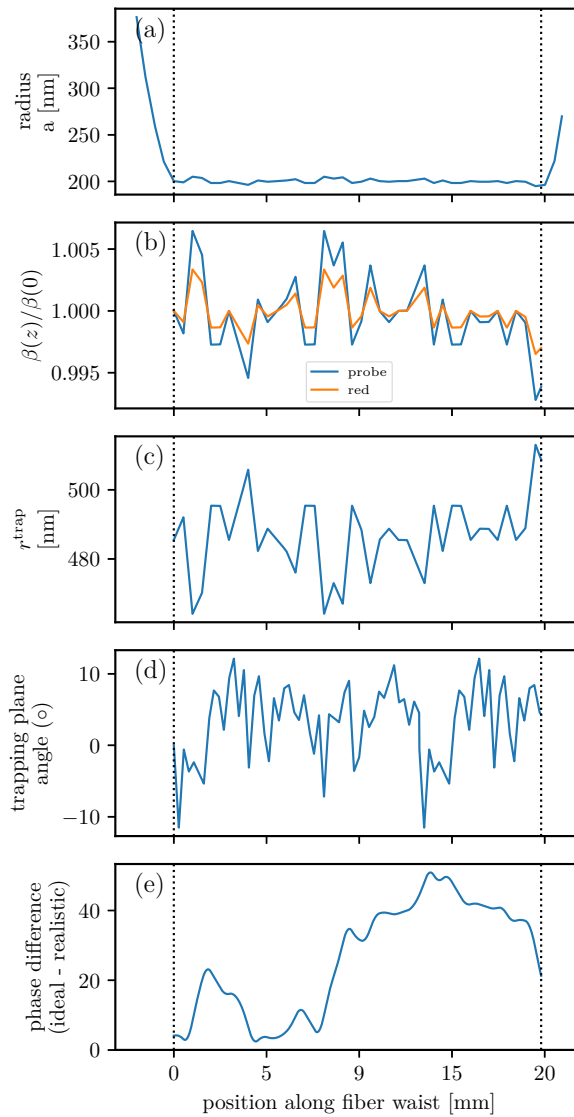


Figure A.4: Effect of fiber non-uniformity over different parameters along the waist of the fiber. (a) A sample nanofiber radius profile as extracted by scanning electron microscopy. (b) The local propagation constant of the probe field and the red-detuned trapping field as determined by the local nanofiber waist dimensions. (c) The radial distance of the trapping minima, given the local fiber profile, for the trap powers mentioned in section A.1.3.3. (d) The rotation of the trapping plane over 50 adjacent sections on the nanofiber waist. The calculation is done from a polarization measurement similar to described in section 3.2.2.3. (e) The phase difference between the light emitted from the atom at position  $z$  when the realistic fiber shown here is used instead of an ideal nanofiber with a perfectly cylindrical waist.

### A.1.3.2 Rotation of trapping plane

The birefringence of the nanofiber waist causes a quasilinearly polarized light field to rotate its polarization. From the visibility measurement similar to the discussion in section 3.2.2.3, one can obtain the relative orientation of the quasilinear polarization of the red-trapping field along the section of a 20 mm long nanofiber waist. This is shown in Fig. A.4(d). The data points corresponds to the entire length of the nanofiber waist being divided into 50 adjacent segments. Due to smaller segment size, the signal to noise per segment is higher, which results in a higher noise in the estimation of the angle of the trapping plane and leads to a more conservative estimate of the directional scattering. However, it must be noted that such a noisy behavior of the change of the trapping plane orientation is not physically expected, as can be seen for larger segment sizes in Fig. 3.6(a). Assuming that the counter-propagating red-trap field is polarization matched to the first one, we can use the values plotted in the figure as a sample  $\phi_j^{\text{trap}}$ .

### A.1.3.3 Position distribution of the atoms about the trapping minima

The uncertainty in the position of trapping minima is shown in the Fig. A.4 (c) and has been accounted for in equation A.5. An additional uncertainty arises from the vibrational motion of the trapped atoms about the trapping minima. The anharmonic trapping potential can be approximated by a harmonic trap centered at the trapping minima. One can extract the trap frequencies from the trap depth. For our case we find trapping frequencies  $(\omega_r, \omega_\theta, \omega_z) = 2\pi \times (110, 55, 172)\text{kHz}$ , respectively, for a configuration  $\sim 20$  mW of blue-trap at 685 nm and  $(0.8 + 0.4)$  mW of red-trap at 1064 nm for two counterpropagating red-detuned trapping field. We assume probing on the strong axis. Assuming a trapped atom as a quantum mechanical harmonic oscillator, one can find out the position spread of the atom in  $n^{\text{th}}$  excited vibration state as  $\sqrt{(2n+1)\hbar/\omega m_{\text{Cs}}}$  where  $\omega$  is the trap frequency. Assuming atoms to be in the first motional ground state, gives as the average position uncertainty as  $(\langle \Delta x \rangle, \langle \Delta y \rangle, \langle \Delta z \rangle) \sim (30, 45, 25)$  nm. To simulate the position uncertainty of the atoms, we shift the position of the atoms,  $(x_j, y_j, z_j)$  in equation A.5(b-d) to  $(x_j + \delta x_j, y_j + \delta y_j, z_j + \delta z_j)$ , according to a normal distribution with the uncertainties calculated as the standard deviation.

### A.1.3.4 Filling factor

As we know from section 3.3.5, not all of the available trapping sites are occupied. We choose a maximum filling factor of around 16 % for all our simulations. Assuming a large MOT with a uniform overlap with the fiber waist and a uniform MOT density, all trapping sites in our simulation have the same probability of being loaded with an atom.

### A.1.3.5 Uncertainty of loading

The overlap of the MOT with the nanofiber waist is not exactly the same in every run. Due to this, the ensembles of atoms are loaded at slightly different regions of the nanofiber waist in different runs of the experiment. Therefore, one can try to add a position uncertainty to the average loading position of the ensemble. This can be restricted over a small region of the nanofiber waist. One can implement it by the shifting the  $z$ -coordinate of the first atom  $z_0$  by a

distance  $\delta'z$ , such that  $\delta'z$  is sampled from a normal distribution with mean of zero and standard deviation being a fraction of the total stretch of the MOT cloud around the fiber. We choose it to be less than a millimeter.

### A.1.3.6 Scattering losses from trapped atoms

Due to the scattering of light from the nanofiber trapped atoms, the intensity of the light field decays as it propagates further through the trapped ensemble. Assuming an OD per atom, one can incorporate this effect as:

$$A_j = A_0 \exp \left[ - \sum_{i=1}^{j-1} \frac{(\alpha^+ o_i^+ + \alpha^- o_i^-)}{2} \right] \quad (\text{A.6})$$

where  $o_i^\pm$  is the occupancy of the site with values 1 or 0 if an atom is present or absent in the  $i^{\text{th}}$  trapping site and  $\pm$  denotes the diametrically opposite sides,  $A_j$  is the electric field amplitude. The factor of 2 arises because the electric field amplitude,  $A_j$ , is proportional to the square root of the intensity. The factor  $\alpha^\pm$  accounts for the OD per atom on the two sides of the nanofiber. This could be different for the two sides owing to difference in the atom-light coupling strengths on the two sides of the fiber. For our simulations, we assume  $\alpha^+ = \alpha^- = 0.03$ . The ratio of amplitude  $A_0$  for probing along strong ( $\sigma_\pm$  dipolar emission, probe polarized along  $x$ ) or weak ( $\pi$  dipolar emission, probe polarized along  $y$ ) axis is  $A_0^{\text{strong}}/A_0^{\text{weak}} \sim \sqrt{2}$  as can be seen from the radial intensity plots (along strong and weak axis) in Fig. 2.3.

### A.1.4 Realistic intensity distribution of the cone

Based on the discussion in the previous sections, one can simulate the scattering from the atoms and calculate the intensity distribution pattern as would be seen on a screen placed at a distance of 0.1 m from the first atom in case of a realistic fiber shown in Fig. A.4. The probe is assumed to propagate along  $-z$  direction. The atoms are loaded into 500 trapping sites on each side of the nanofiber, with filling factor  $p_F = 0.16$ , with the position of the first atom ( $z_0$ ) normally distributed in the first 1 mm section of the fiber shown in Fig. A.4. All fiber imperfections discussed are taken into account with accordingly modified position of the trapped atom ( $x_j, y_j, z_j$ ) and associated position uncertainties ( $\delta z_j, \delta x_j, \delta y_j$ ), propagation constants, trapping plane angle, and filling factor. We calculate the intensity pattern as recorded on the screen averaged over 500 realizations of the atomic ensemble. The result is shown in Fig. A.5. The leftmost and rightmost plots are intensity distribution along the vertical direction,  $y = 0$ , for probing along weak and strong axis respectively. The top left and top right plots are intensity distribution along the  $x$ -axis of the screen for probing along the weak and strong axis. The intensity distribution on the entire screen is shown by the two central plots. The left and right half of the figure corresponds to a simulated collective Bragg scattering as expected to be seen on a screen for an array of  $\pi$  and  $\sigma_\pm$  polarized atomic dipoles, respectively.

From our calculations, we conclude that one should be able to observe the Bragg scattering despite the imperfections in the fiber. One can compare the intensity pattern for a nonuniform

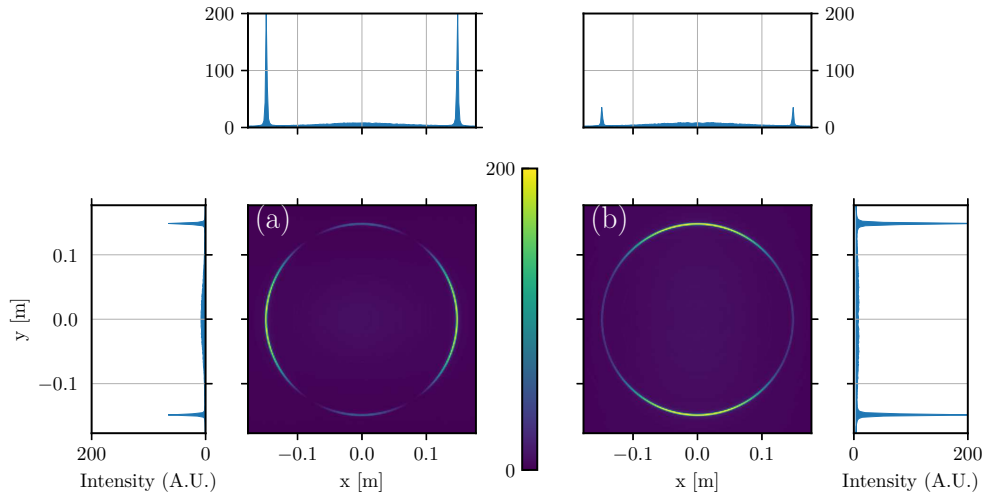


Figure A.5: Average intensity pattern as expected on a screen for atoms filled in 500 pairs of trapping sites with filling factor  $p_F = 0.16$  when probed along weak axis (a) and strong axis (b) corresponding to  $\pi$  polarized and  $\sigma$  polarized atomic dipoles respectively. The fiber radius, propagations constants, trap minima position and trapping plane angular deviations are accounted for as in Fig. A.4. The averaging is done over 500 ensembles which are assumed to be within the first 1 mm section of the fiber. The averaged intensity is normalized to the number of atoms in each case. The screen is located at  $z = -0.1$  m. The top and side panels show the intensity distribution as seen along the lines  $y = 0$  and  $x = 0$  respectively.

fiber Fig. A.5(b) with the case of a uniform nanofiber waist Fig. A.3(d). Both the figures have the same probe configuration (quasilinearly polarized along  $x$ ) and also equal number of  $\sigma_+$  and  $\sigma_-$  polarized atoms on the two sides of the fiber. The intensity distribution along the line  $x = 0$ , for both cases is shown in Fig. A.6. One can see that in the case of an imperfect fiber, the contrast of the intensity pattern decreases at the cost of increase of the background. The fiber imperfections causes imperfect phase matching of the light emitted from nonuniformly spaced emitters, thereby causing only a partial constructive interference. In addition, the decrease in the filling factor causes the atoms to be spread out further, such that the paraxial approximation in the far-field limit (shown in Fig. A.1(b)) does not hold. In other words, the angle  $\theta$  for constructive interference of light emitted from atoms placed far apart, is no longer given by the Bragg condition in equation A.1, which blurs the cone. In general, the biggest factor contributing to the reduction of the cone contrast is the non-uniform fiber surface. It causes the relative phase between the light emitted from any atom with respect to the first atom to fluctuate as shown in Fig. A.4(e). Over a distance of a few hundred micrometers the phase change can be more than  $2\pi$ . Therefore, each small section of the fiber, creates a ring on the screen because of almost perfect phase matching. Each of these rings is slightly displaced from one another because different sections of fiber emit light at the angle given by the Bragg condition. However, due to imperfect filling factor, each of these rings is broader than the ideal case and can partially overlap and destructively interfere with the adjacent rings. As a result, for very large atomic

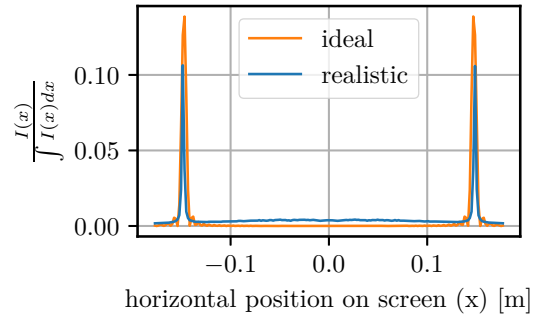


Figure A.6: Comparison of intensity distribution for the case of uniform (ideal) and nonuniform fiber (realistic). The normalized intensity distribution along the line,  $y = 0$ , on the imaging screen is plotted. The probe field is quasilinearly polarized along  $x$  direction in both cases, and the position of the screen is the same. The position of the cone is indicated by the intensity peaks. There is a significant background in the region other than the cone, and the contrast of the cone is reduced when the realistic situation is considered (see main text).

ensemble we still expect to observe the directed emission, but instead of a single peak, there will be multiple bright and dark fringes at roughly the angle given by the Bragg condition in equation A.1.

## A.2 Detection

To prove the existence of such a directed emission, the most direct way seems to image the ring on a single-photon sensitive camera (Andor iXon 897) using a two lens imaging system as shown in Fig. A.8. For that one needs to evaluate the Bragg angle for a resonant probe field for a given red-trap laser wavelength using the equation A.1. Fig. A.7 (top) shows the Bragg scattering angles for various red-trap wavelengths for a probing field at  $\sim 852$  nm (blue, D2 line of Cs) and  $\sim 894$  nm (orange, D1 line of Cs). For the simulations done in this chapter, the red-detuned trap laser was assumed to be at 1064 nm for which most of the D2 light is scattered out at roughly  $56^\circ$  and most of the D1 light is scattered out at  $49^\circ$ .

The light emitted from the atomic ensemble along the direction of the cone has a plane wavefront with wavevector oriented along the cone. To collect this light and image the cone, an example two-lens imaging system is shown in Fig. A.8. The example calculation for Fig. A.8 was done using ABCD matrix formalism by a postdoc in our group. The Bragg angle corresponding to the figure is  $20^\circ$  corresponding to red-trap laser at the magic wavelength of Cs (935 nm) and probing at D1-line of Cs at  $\sim 894$  nm. To resolve the angular distribution of the emitted light, the first convex lens collects the light emitted at different angles and focuses it to a point in the focal plane. Therefore, the light from the cone is focussed to a ring shaped intensity distribution. The closest this lens can be placed to the ensemble is  $\sim 11$  cm which is limited by the glass vacuum chamber. The aperture of this lens needs to be large enough such that it can collect light from the entire cone, with minimum spherical aberration. We propose to

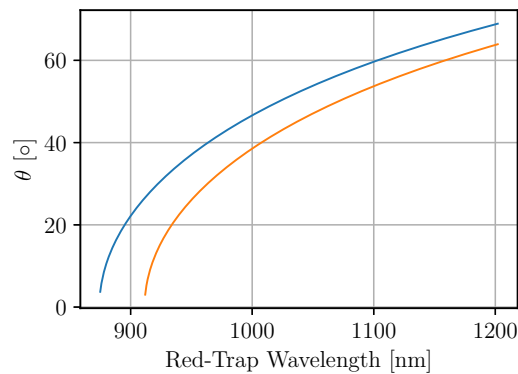


Figure A.7: Scattering angle for different red-trap wavelengths for D2- and D1-lines of Cs at 852.35 nm (blue) and 894.59 nm (orange), respectively.

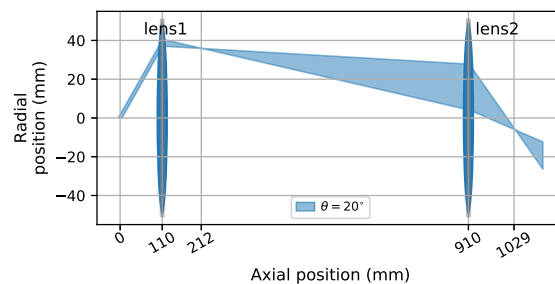


Figure A.8: A possible imaging setup for the Bragg ring. The Bragg emission is at  $20^\circ$  corresponding to a red-detuned trap field at 935 nm and resonant probe at wavelength of 894.59 nm which corresponds to the D1-line of Cs. The camera sensor is placed at the focus of the second lens at  $\approx 1030$  mm. Each lens in the setup has a focal length of 110 mm.

use a Fresnel lens from Edmund Optics with focal length of 110 mm for this purpose. Due to the finite size of the sensor on the camera ( $8.2 \text{ mm} \times 8.2 \text{ mm}$ ), the ring shaped image focussed behind the first lens has a larger diameter than the sensor and has to be demagnified. Therefore, a second convex lens is placed at roughly 910 mm from the atoms to obtain a demagnified image at  $\approx 103 \text{ cm}$  from the atoms, with the diameter of the ring shape image reduced by a factor of roughly 6. We place the camera sensor at this point to obtain the sharpest image of the ring.

### A.3 Outlook

The Bragg scattering process as discussed here occurs as a result of constructive interference. It is quite obvious that by destroying the periodicity (for example by switching to a running wave configuration instead of standing wave for the red-trap field) one randomizes the phase of the light scattered out which leads to a uniform rather than directed emission. This can serve as a negative control measurement to prove the dependence of directional emission on the ordering

of trapping array. Another possible negative control measurement to confirm directional emission will be to destroy the phase coherence of the emissions from the individual atoms so as to prevent constructive interference. This should give a uniform emission in  $4\pi$  rather than a directional emission. To do so, we propose to excite the atoms with a short (duration  $\tau_{\text{pulse}} \ll \Gamma^{-1}$ ) intense resonant light pulse such that the pulse area corresponds to  $\pi$ . By doing so one can achieve a population inversion of the whole atomic ensemble. Upon decay, the photons emitted from each excited atom will have random phases and, therefore, they will not show any preferential direction of emission. In this case as well, we expect the ring to be absent. A positive control experiment for confirmation of the Bragg scattering would be to scan the red-detuned trap laser wavelength and verify the dependence of the scattering angle on the wavelength of the red-detuned trap laser. The dependence is given according to the Bragg condition in equation A.1 and shown by Fig. A.7. The scattering angle in this measurement can be inferred from the diameter of the observed ring.

The treatment here is elementary and serves as a guideline for a more thorough approach. Other factors that could be taken into account are multi-level nature of the atoms, reflection of light from the nanofiber waist surface (Mie-scattering) in the vicinity of the atoms, heating of the atoms due to scattering of resonant photons, birefringence experienced by each light field as it propagates in the nanofiber waist and any possible back-reflection of the red-detuned trapping field. Once established experimentally, Bragg scattering opens up avenues for efficient coupling of radiative modes of the atom with the guided modes of the nanofiber waveguide. The topic in general is a complex many-body physics problem and a thorough theoretical treatment and an experimental verification could be a future direction of research.



## Supplementary information

### B.1 Correlations for all atom numbers

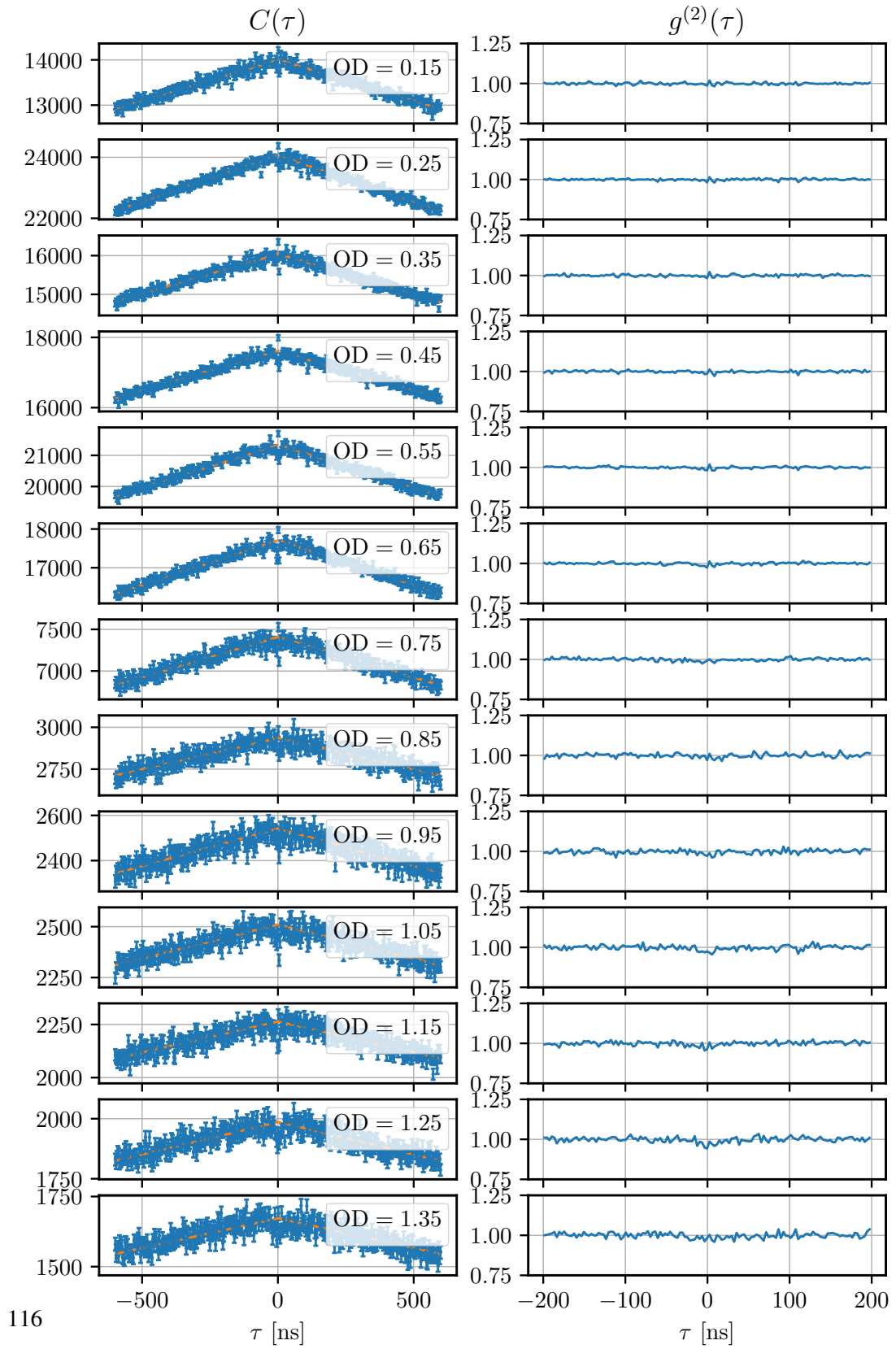


Figure B.1

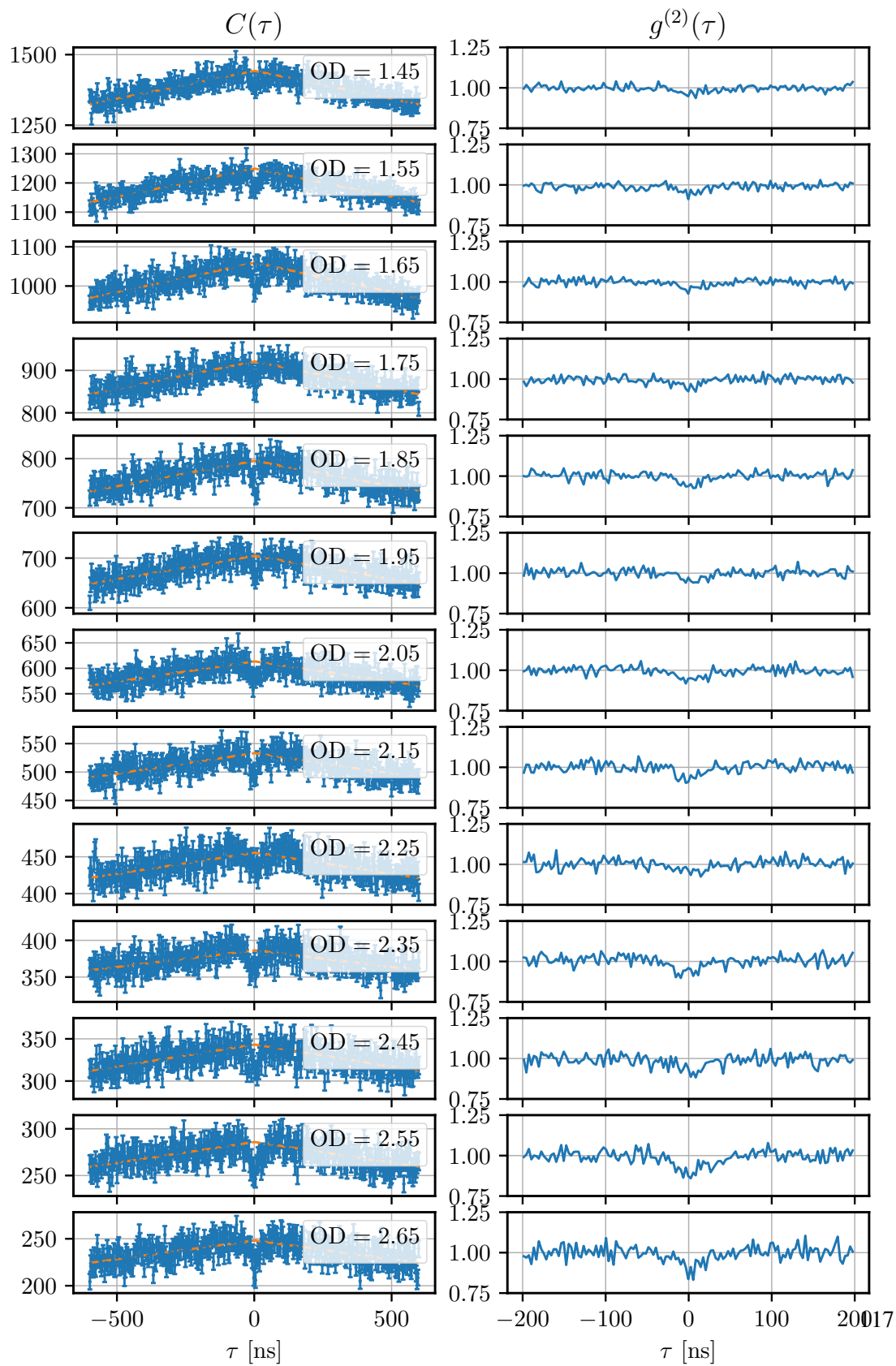


Figure B.2

B. SUPPLEMENTARY INFORMATION

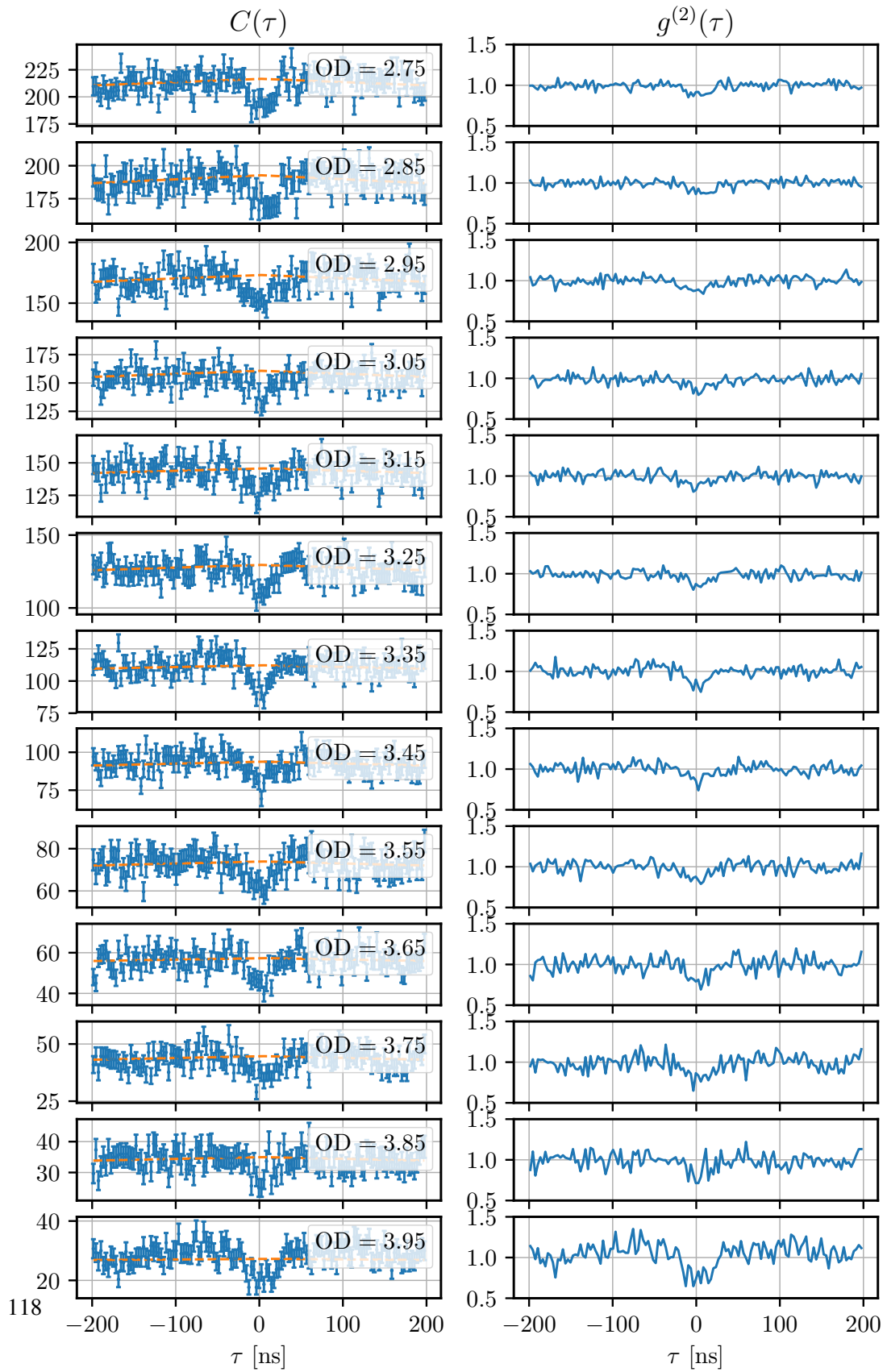


Figure B.3

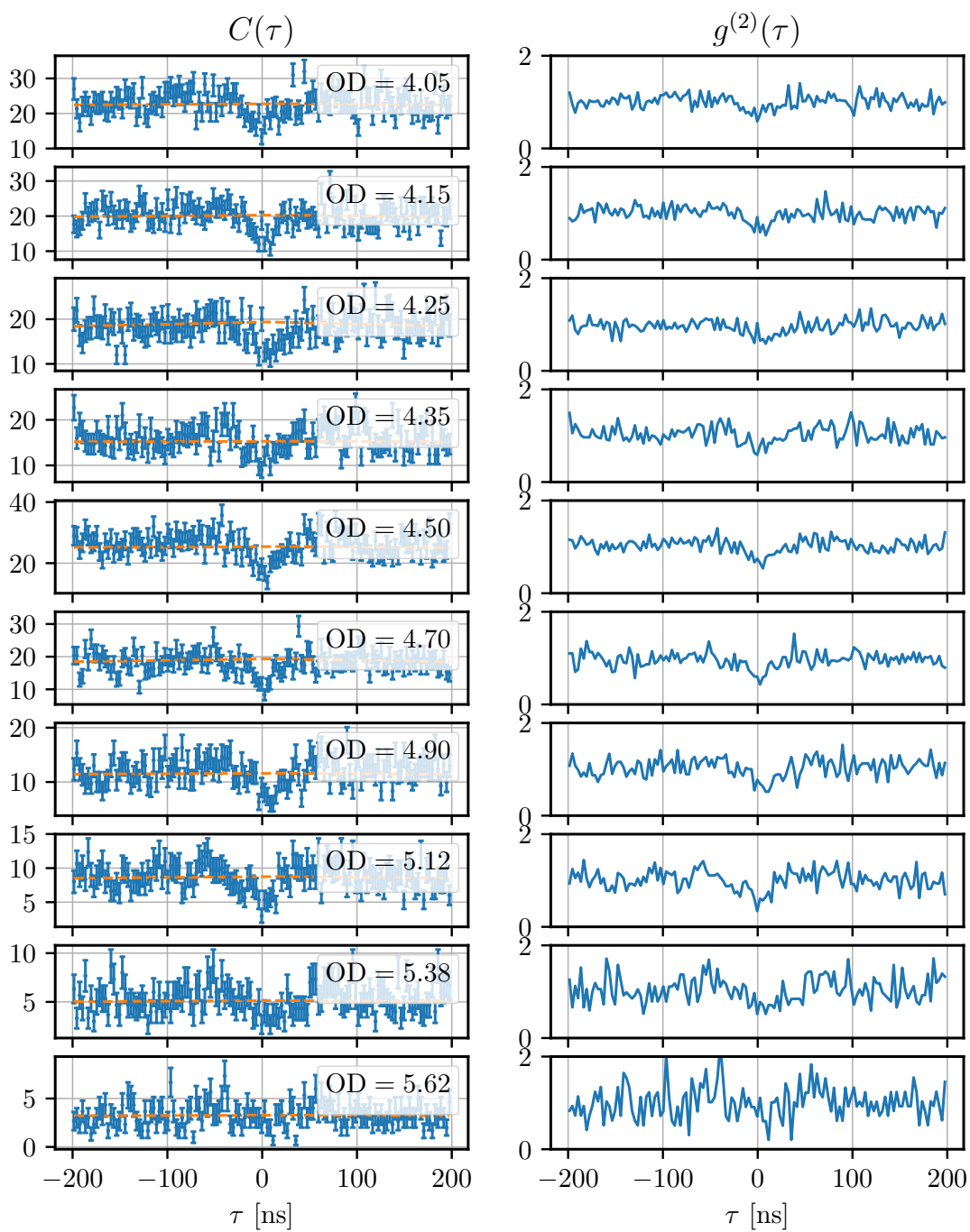


Figure B.4

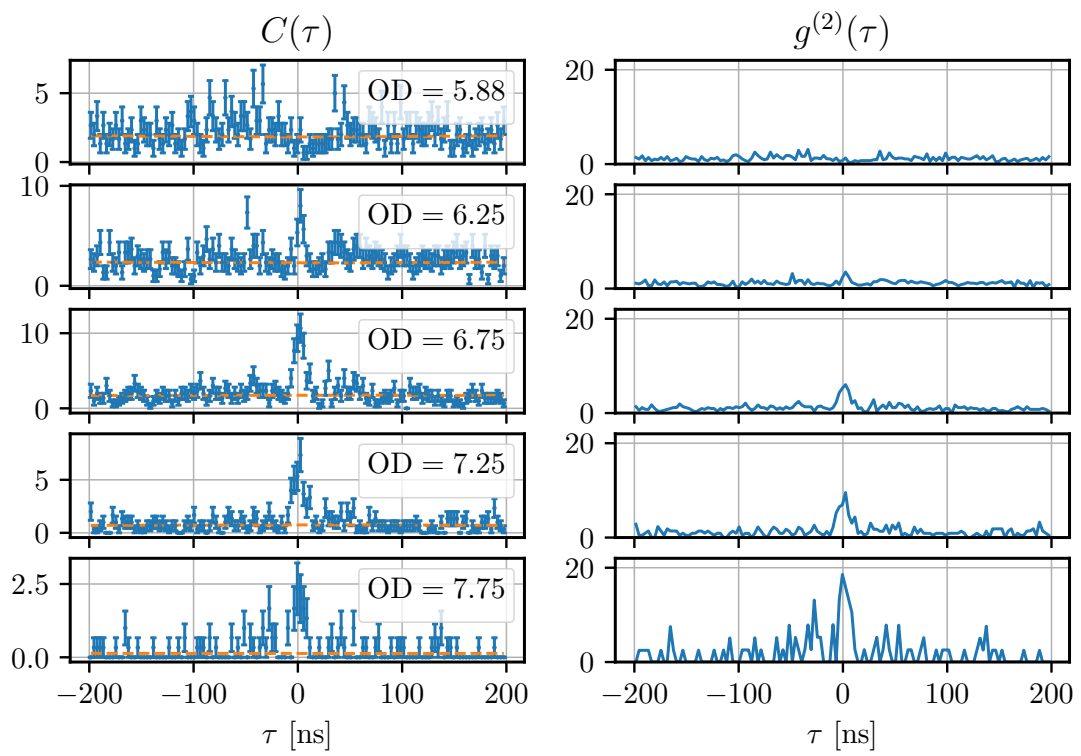


Figure B.5

# Bibliography

- [1] Max Planck. On the law of distribution of energy in the normal spectrum. *Annalen der physik*, 4(553):1, 1901.
- [2] A Einstein. Einstein's proposal of the photon conceptia translation of the annalen der physik paper of 1905. *Ann. Physik*, 17:132, 1905.
- [3] Albert Einstein. Zur quantentheorie der strahlung. *Phys. Z.*, 18:121–128, 1917.
- [4] Eugene Hecht. Hecht optics. *Addison Wesley*, 997:213–214, 1998.
- [5] Niels Bohr. Xxxvii. on the constitution of atoms and molecules. *The London, Edinburgh, and Dublin Philosophical Magazine and Journal of Science*, 26(153):476–502, 1913.
- [6] Louis De Broglie. *Recherches sur la théorie des quanta*. PhD thesis, Migration-université en cours d'affectation, 1924.
- [7] Werner Heisenberg. Quantum-theoretical re-interpretation of kinematic and mechanical relations. *Z. Phys*, 33:879–893, 1925.
- [8] Erwin Schrödinger. An undulatory theory of the mechanics of atoms and molecules. *Physical review*, 28(6):1049, 1926.
- [9] Paul Adrien Maurice Dirac. Quantum mechanics and a preliminary investigation of the hydrogen atom. *Proceedings of the Royal Society of London. Series A, Containing Papers of a Mathematical and Physical Character*, 110(755):561–579, 1926.
- [10] Paul Adrien Maurice Dirac. The quantum theory of the emission and absorption of radiation. *Proceedings of the Royal Society of London. Series A, Containing Papers of a Mathematical and Physical Character*, 114(767):243–265, 1927.
- [11] Arthur L Schawlow and Charles H Townes. Infrared and optical masers. *Physical Review*, 112(6):1940, 1958.
- [12] Amnon Yariv and JP Gordon. The laser. *Proceedings of the IEEE*, 51(1):4–29, 1963.
- [13] GJ Troup. Photon counting and photon statistics. *Progress in Quantum Electronics*, 2:1–43, 1973.

- [14] John F Clauser. Experimental distinction between the quantum and classical field-theoretic predictions for the photoelectric effect. *Physical Review D*, 9(4):853, 1974.
- [15] P. G. Kwiat, K. Mattle, H. Weinfurter, A. Zeilinger, A. V. Sergienko, and Y. Shih. New high-intensity source of polarization-entangled photon pairs. *Physical Review Letters*, 75(24):4337, 1995.
- [16] D. V. Strekalov, T. B. Pittman, A. V. Sergienko, Y. H. Shih, and P. G. Kwiat. Postselection-free energy-time entanglement. *Phys. Rev. A*, 54:R1–R4, Jul 1996.
- [17] Roy S. Bondurant, Prem Kumar, Jeffrey H. Shapiro, and Mari Maeda. Degenerate four-wave mixing as a possible source of squeezed-state light. *Phys. Rev. A*, 30:343–353, Jul 1984.
- [18] M. D. Lukin and A. Imamoglu. Nonlinear optics and quantum entanglement of ultraslow single photons. *Physical Review Letters*, 84(7):1419, 2000.
- [19] H-J Briegel, Tommaso Calarco, Dieter Jaksch, Juan Ignacio Cirac, and Peter Zoller. Quantum computing with neutral atoms. *Journal of modern optics*, 47(2-3):415–451, 2000.
- [20] Mete Atatüre, Dirk Englund, Nick Vamivakas, Sang-Yun Lee, and Joerg Wrachtrup. Material platforms for spin-based photonic quantum technologies. *Nature Reviews Materials*, 3(5):38–51, 2018.
- [21] Hannes Bernien, Sylvain Schwartz, Alexander Keesling, Harry Levine, Ahmed Omran, Hannes Pichler, Soonwon Choi, Alexander S Zibrov, Manuel Endres, Markus Greiner, et al. Probing many-body dynamics on a 51-atom quantum simulator. *Nature*, 551(7682):579–584, 2017.
- [22] Vittorio Giovannetti, Seth Lloyd, and Lorenzo Maccone. Quantum metrology. *Phys. Rev. Lett.*, 96:010401, Jan 2006.
- [23] Luca Pezzè, Augusto Smerzi, Markus K Oberthaler, Roman Schmied, and Philipp Treutlein. Quantum metrology with nonclassical states of atomic ensembles. *Reviews of Modern Physics*, 90(3):035005, 2018.
- [24] H. J. Kimble. The quantum internet. *Nature*, 453:1023, 2008.
- [25] Klemens Hammerer, Anders S Sørensen, and Eugene S Polzik. Quantum interface between light and atomic ensembles. *Reviews of Modern Physics*, 82(2):1041, 2010.
- [26] Yixing Yang, Ying Zheng, Weiran Cao, Alexandre Titov, Jake Hyvonen, Jesse R Manders, Jiangeng Xue, Paul H Holloway, and Lei Qian. High-efficiency light-emitting devices based on quantum dots with tailored nanostructures. *Nature Photonics*, 9(4):259, 2015.
- [27] J. P. Dowling and Gerard J Milburn. Quantum technology: the second quantum revolution. *Philosophical Transactions of the Royal Society of London. Series A: Mathematical, Physical and Engineering Sciences*, 361(1809):1655–1674, 2003.



- [28] Herbert Walther, Benjamin TH Varcoe, Berthold-Georg Englert, and Thomas Becker. Cavity quantum electrodynamics. *Reports on Progress in Physics*, 69(5):1325, 2006.
- [29] R. H. Dicke. Coherence in spontaneous radiation processes. *Phys. Rev.*, 93:99, 1954.
- [30] L. M. Duan, M. D. Lukin, J. I. Cirac, and P. Zoller. Long-distance quantum communication with atomic ensembles and linear optics. *Nature*, 414(6862):413–418, 2001.
- [31] Jonathan P Dowling and Julio Gea-Banacloche. Evanescent light-wave atom mirrors, resonators, waveguides, and traps. In *Advances in atomic, molecular, and optical physics*, volume 37, pages 1–94. Elsevier, 1996.
- [32] F. Le Kien, V. I. Balykin, and K. Hakuta. Atom trap and waveguide using a two-color evanescent light field around a subwavelength-diameter optical fiber. *Physical Review A*, 70(6):063403, 2004.
- [33] Pablo Solano, Jeffrey A Grover, Jonathan E Hoffman, Sylvain Ravets, Fredrik K Fatemi, Luis A Orozco, and Steven L Rolston. Optical nanofibers: a new platform for quantum optics. In *Advances In Atomic, Molecular, and Optical Physics*, volume 66, pages 439–505. Elsevier, 2017.
- [34] Kali P Nayak, Mark Sadgrove, Ramachandrarao Yalla, Fam Le Kien, and Kohzo Hakuta. Nanofiber quantum photonics. *Journal of Optics*, 20(7):073001, 2018.
- [35] F. Le Kien, J. Q. Liang, K. Hakuta, and V. I. Balykin. Field intensity distributions and polarization orientations in a vacuum-clad subwavelength-diameter optical fiber. *Optics communications*, 242(4):445–455, 2004.
- [36] E. Vetsch, D. Reitz, G. Sagué, R. Schmidt, S. T. Dawkins, and A. Rauschenbeutel. Optical interface created by laser-cooled atoms trapped in the evanescent field surrounding an optical nanofiber. *Phys. Rev. Lett.*, 104(20):203603, 2010.
- [37] Neil V Corzo, Jérémy Raskop, Aveek Chandra, Alexandra S Sheremet, Baptiste Gouraud, and Julien Laurat. Waveguide-coupled single collective excitation of atomic arrays. *Nature*, 566(7744):359–362, 2019.
- [38] D. Reitz, C. Sayrin, R. Mitsch, P. Schneeweiss, and A. Rauschenbeutel. Coherence properties of nanofiber-trapped cesium atoms. *Physical Review Letters*, 110(24):243603, 2013.
- [39] Y. Meng, A. Dareau, P. Schneeweiss, and A. Rauschenbeutel. Near-ground-state cooling of atoms optically trapped 300 nm away from a hot surface. *Phys. Rev. X*, 8:031054, Sep 2018.
- [40] A. Asenjo-Garcia, M. Moreno-Cardoner, A. Albrecht, H. J. Kimble, and D. E. Chang. Exponential improvement in photon storage fidelities using subradiance and “selective radiance” in atomic arrays. *Phys. Rev. X*, 7:031024, 2017.

- [41] Peter Lodahl, Sahand Mahmoodian, Søren Stobbe, Arno Rauschenbeutel, Philipp Schneeweiss, Jürgen Volz, Hannes Pichler, and Peter Zoller. Chiral quantum optics. *Nature*, 541(7638):473–480, 2017.
- [42] Jan Petersen, Jürgen Volz, and Arno Rauschenbeutel. Chiral nanophotonic waveguide interface based on spin-orbit interaction of light. *Science*, 346:67, 2014.
- [43] R. Mitsch, C. Sayrin, B. Albrecht, P. Schneeweiss, and A. Rauschenbeutel. Quantum state-controlled directional spontaneous emission of photons into a nanophotonic waveguide. *Nat. Commun.*, 5:5713, 2014.
- [44] Aisling Johnson, Martin Blaha, Alexander E Ulanov, Arno Rauschenbeutel, Philipp Schneeweiss, and Jürgen Volz. Observation of multimode strong coupling of cold atoms to a 30-m long optical resonator. *arXiv preprint arXiv:1905.07353*, 2019.
- [45] Fam Le Kien and Arno Rauschenbeutel. Propagation of nanofiber-guided light through an array of atoms. *Physical Review A*, 90(6):063816, 2014.
- [46] Neil V Corzo, Baptiste Gouraud, Aweek Chandra, Akihisa Goban, Alexandra S Sheremet, Dmitriy V Kupriyanov, and Julien Laurat. Large bragg reflection from one-dimensional chains of trapped atoms near a nanoscale waveguide. *Physical Review Letters*, 117(13):133603, 2016.
- [47] Pablo Solano, Pablo Barberis-Blostein, Fredrik K Fatemi, Luis A Orozco, and Steven L Rolston. Super-radiance reveals infinite-range dipole interactions through a nanofiber. *Nature communications*, 8(1):1857, 2017.
- [48] H Jeff Kimble, Mario Dagenais, and Leonard Mandel. Photon antibunching in resonance fluorescence. *Physical Review Letters*, 39(11):691, 1977.
- [49] Jung-Tsung Shen and Shanhui Fan. Strongly correlated multiparticle transport in one dimension through a quantum impurity. *Phys. Rev. A*, 76:062709, 2007.
- [50] Xin HH Zhang and Harold U Baranger. Quantum interference and complex photon statistics in waveguide qed. *Physical Review A*, 97(2):023813, 2018.
- [51] Sahand Mahmoodian, Mantas Čepulkovskis, Sumanta Das, Peter Lodahl, Klemens Hammerer, and Anders S. Sørensen. Strongly correlated photon transport in waveguide quantum electrodynamics with weakly coupled emitters. *Phys. Rev. Lett.*, 121:143601, Oct 2018.
- [52] Sahand Mahmoodian. *In preparation*, 2019.
- [53] Katsunari Okamoto. *Fundamentals of optical waveguides*. Academic press, 2006.
- [54] Allan W Snyder and John Love. *Optical waveguide theory*. Springer Science & Business Media, 2012.

- [55] Ariane Stiebeiner, Ruth Garcia-Fernandez, and Arno Rauschenbeutel. Design and optimization of broadband tapered optical fibers with a nanofiber waist. *Optics express*, 18(22):22677–22685, 2010.
- [56] Fam Le Kien and A Rauschenbeutel. Anisotropy in scattering of light from an atom into the guided modes of a nanofiber. *Physical Review A*, 90(2):023805, 2014.
- [57] Fam Le Kien, S Dutta Gupta, VI Balykin, and K Hakuta. Spontaneous emission of a cesium atom near a nanofiber: Efficient coupling of light to guided modes. *Physical Review A*, 72(3):032509, 2005.
- [58] R. Mitsch, C. Sayrin, B. Albrecht, P. Schneeweiss, and A. Rauschenbeutel. Exploiting the local polarization of strongly confined light for sub-micrometer-resolution internal state preparation and manipulation of cold atoms. *Phys. Rev. A*, 89(6):063829, 2014.
- [59] Daniel A Steck. Cesium d line data. *Los Alamos National Laboratory (unpublished)*, 124, 2003.
- [60] K-H Weber and Craig J Sansonetti. Accurate energies of ns, np, nd, nf, and ng levels of neutral cesium. *Physical Review A*, 35(11):4650, 1987.
- [61] J. D. Jackson. *Classical Electrodynamics*. John Wiley & Sons, Inc., 1999.
- [62] Fam Le Kien, Philipp Schneeweiss, and Arno Rauschenbeutel. Dynamical polarizability of atoms in arbitrary light fields: general theory and application to cesium. *The European Physical Journal D*, 67(5):92, 2013.
- [63] Fam Le Kien, Philipp Schneeweiss, and Arno Rauschenbeutel. State-dependent potentials in a nanofiber-based two-color trap for cold atoms. *Physical Review A*, 88(3):033840, 2013.
- [64] E. Vetsch, D. Reitz, G. Sagué, R. Schmidt, S. T. Dawkins, and A. Rauschenbeutel. Optical interface created by laser-cooled atoms trapped in the evanescent field surrounding an optical nanofiber. *Physical Review Letters*, 104(20):203603, 2010.
- [65] F. Le Kien, V. I. Balykin, and K. Hakuta. State-insensitive trapping and guiding of cesium atoms using a two-color evanescent field around a subwavelength-diameter fiber. *Journal of the Physical Society of Japan*, 74(3):910–917, 2005.
- [66] A Goban, KS Choi, DJ Alton, D Ding, C Lacroûte, M Pototschnig, T Thiele, NP Stern, and HJ Kimble. Demonstration of a state-insensitive, compensated nanofiber trap. *Physical Review Letters*, 109(3):033603, 2012.
- [67] Bernhard Albrecht, Yijian Meng, Christoph Clausen, Alexandre Dureau, Philipp Schneeweiss, and Arno Rauschenbeutel. Fictitious magnetic-field gradients in optical microtraps as an experimental tool for interrogating and manipulating cold atoms. *Physical Review A*, 94(6):061401, 2016.

- [68] Christopher J Foot et al. *Atomic physics*, volume 7. Oxford University Press, 2005.
- [69] J.-B. Béguin, M. Bookjans, E. L. Christensen, S. L. Sørensen, H. H. Müller, J. S. Polzik, E. and J. Appel. Generation and detection of a sub-poissonian atom number distribution in a one-dimensional optical lattice. *Phys. Rev. Lett.*, 113:263603, Dec 2014.
- [70] B. Gouraud, D. Maxein, A. Nicolas, O. Morin, and J. Laurat. Demonstration of a Memory for Tightly Guided Light in an Optical Nanofiber. pages 4–8, 2015.
- [71] Michael Morrissey, Kieran Deasy, Mary Frawley, Ravi Kumar, Eugen Prel, Laura Russell, Viet Truong, and Síle Nic Chormaic. Spectroscopy, manipulation and trapping of neutral atoms, molecules, and other particles using optical nanofibers: a review. *Sensors*, 13(8):10449–10481, 2013.
- [72] E. Vetsch, S. T. Dawkins, R. Mitsch, D. Reitz, P. Schneeweiss, and A. Rauschenbeutel. Nanofiber-based optical trapping of cold neutral atoms. *Selected Topics in Quantum Electronics, IEEE Journal of*, 18(6):1763–1770, 2012.
- [73] Margareta Wallquist, Klemens Hammerer, Peter Rabl, Mikhail Lukin, and Peter Zoller. Hybrid quantum devices and quantum engineering. *Physica Scripta*, 2009(T137):014001, 2009.
- [74] Juan Ignacio Cirac, Peter Zoller, H Jeff Kimble, and Hideo Mabuchi. Quantum state transfer and entanglement distribution among distant nodes in a quantum network. *Physical Review Letters*, 78(16):3221, 1997.
- [75] Jakob Hinney. *Generation of squeezed light with nanofiber trapped atoms*. PhD thesis, 2019.
- [76] M Succi, R Canino, and B Ferrario. Atomic absorption evaporation flow rate measurements of alkali metal dispensers. *Vacuum*, 35(12):579–582, 1985.
- [77] Philipp Schneeweiss, Sophie Zeiger, Thomas Hoinkes, Arno Rauschenbeutel, and Jürgen Volz. Fiber ring resonator with a nanofiber section for chiral cavity quantum electrodynamics and multimode strong coupling. *Optics letters*, 42(1):85–88, 2017.
- [78] Yen-Wei Lin, Hung-Chih Chou, Prashant P Dwivedi, Ying-Cheng Chen, and A Yu Ite. Using a pair of rectangular coils in the mot for the production of cold atom clouds with large optical density. *Optics express*, 16(6):3753–3761, 2008.
- [79] Christopher J. Foot. *Atomic physics*, 2005.
- [80] EA Donley, TP Heavner, F Levi, MO Tataw, and SR Jefferts. Double-pass acousto-optic modulator system. *Review of Scientific Instruments*, 76(6):063112, 2005.
- [81] Isabelle Serre, Laurence Pruvost, and Hong Tuan Duong. Fluorescence imaging efficiency of cold atoms in free fall. *Applied optics*, 37(6):1016–1021, 1998.

- [82] David A Smith, Simon Aigner, Sebastian Hofferberth, Michael Gring, Mauritz Anderson, Stefan Wildermuth, Peter Krüger, Stephan Schneider, Thorsten Schumm, and Jörg Schmiedmayer. Absorption imaging of ultracold atoms on atom chips. *Optics express*, 19(9):8471–8485, 2011.
- [83] Martin Blaha. Combined polarisation and absorption imaging for experiments with nanofiber trapped atoms. Master’s thesis, Technische Universität Wien, 2016.
- [84] Bernhard Albrecht. *Storage of fiber-guided light in a nanofiber-trapped ensemble of cold cesium atoms*. PhD thesis, Wien, 2017.
- [85] Baptiste Gouraud. *Optical Nanofibers Interfacing Cold Atoms-A Tool for Quantum Optics*. PhD thesis, 2016.
- [86] Ying-Cheng Chen, Yean-An Liao, Long Hsu, and A Yu Ite. Simple technique for directly and accurately measuring the number of atoms in a magneto-optical trap. *Physical Review A*, 64(3):031401, 2001.
- [87] Daniel Hümmer, Philipp Schneeweiss, Arno Rauschenbeutel, and Oriol Romero-Isart. Heating in nanophotonic traps for cold atoms. *Physical Review X*, 9(4):041034, 2019.
- [88] Andreas Reiserer, Norbert Kalb, Gerhard Rempe, and Stephan Ritter. A quantum gate between a flying optical photon and a single trapped atom. *Nature*, 508(7495):237–240, 2014.
- [89] Thibault Peyronel, Ofer Firstenberg, Qi-Yu Liang, Sebastian Hofferberth, Alexey V Gorshkov, Thomas Pohl, Mikhail D Lukin, and Vladan Vuletić. Quantum nonlinear optics with single photons enabled by strongly interacting atoms. *Nature*, 488(7409):57, 2012.
- [90] Peter Lodahl, Sahand Mahmoodian, Søren Stobbe, Arno Rauschenbeutel, Philipp Schneeweiss, Jürgen Volz, Hannes Pichler, and Peter Zoller. Chiral quantum optics. *Nature*, 541(7638):473–480, 2017.
- [91] Peter Lodahl, Sahand Mahmoodian, and Søren Stobbe. Interfacing single photons and single quantum dots with photonic nanostructures. *Rev. Mod. Phys.*, 87:347, 2015.
- [92] D. E. Chang, J. S. Douglas, A. González-Tudela, C.-L. Hung, and H. J. Kimble. Colloquium: Quantum matter built from nanoscopic lattices of atoms and photons. *Rev. Mod. Phys.*, 90:031002, Aug 2018.
- [93] Kevin M. Birnbaum, Andreea Boca, Russell Miller, Allen D. Boozer, Tracy E. Northup, and H. Jeff Kimble. Photon blockade in an optical cavity with one trapped atom. *Nature*, 436(7047):87, 2005.
- [94] Andrei Faraon, Ilya Fushman, Dirk Englund, Nick Stoltz, Pierre Petroff, and Jelena Vučkovic. Coherent generation of non-classical light on a chip via photon-induced tunnelling and blockade. *Nat. Phys.*, 4:859, 2008.

- [95] A. Reinhard, T. Volz, M. Winger, A. Badolato, K. J. Hennessy, and E. L. Hu and A. Imamoglu. Strongly correlated photons on a chip. *Nat. Photonics*, 6:93, 2012.
- [96] Andreas Reiserer, Norbert Kalb, Gerhard Rempe, and Stephan Ritter. A quantum gate between a flying optical photon and a single trapped atom. *Nature*, 508:237, 2014.
- [97] Christoph Hamsen, Karl Nicolas Tolazzi, Tatjana Wilk, and Gerhard Rempe. Two-photon blockade in an atom-driven cavity qed system. *Phys. Rev. Lett.*, 118:133604, Mar 2017.
- [98] Y. O. Dudin and A. Kuzmich. Strongly interacting rydberg excitations of a cold atomic gas. *Science*, 336(6083):887–889, 2012.
- [99] Valentina Parigi, Erwan Bimbard, Jovica Stanojevic, Andrew J. Hilliard, Florence Nogrette, Rosa Tualle-Brouri, Alexei Ourjoumtsev, and Philippe Grangier. Observation and measurement of interaction-induced dispersive optical nonlinearities in an ensemble of cold rydberg atoms. *Phys. Rev. Lett.*, 109:233602, Dec 2012.
- [100] D. Maxwell, D. J. Szwer, D. Paredes-Barato, H. Busche, J. D. Pritchard, A. Gauguier, K. J. Weatherill, M. P. A. Jones, and C. S. Adams. Storage and control of optical photons using rydberg polaritons. *Phys. Rev. Lett.*, 110:103001, Mar 2013.
- [101] Jeff D. Thompson, Travis L. Nicholson, Qi-Yu Liang, Sergio H. Cantu, Aditya V. Venkatramani, Soonwon Choi, Ilya A. Fedorov, Daniel Viscor, Thomas Pohl, Mikhail D. Lukin, and Vladan Vuletić. Symmetry-protected collisions between strongly interacting photons. *Nature*, 542(7640):206, 2017.
- [102] Ofer Firstenberg, Thibault Peyronel, Qi-Yu Liang, Alexey V. Gorshkov, Mikhail D. Lukin, and Vladan Vuletić. Attractive photons in a quantum nonlinear medium. *Nature*, 502:71, 2013.
- [103] Simon Baur, Daniel Tiarks, Gerhard Rempe, and Stephan Dürr. Single-photon switch based on rydberg blockade. *Phys. Rev. Lett.*, 112:073901, Feb 2014.
- [104] Nina Stiesdal, Jan Kumlin, Kevin Kleinbeck, Philipp Lunt, Christoph Braun, Asaf Paris-Mandoki, Christoph Tresp, Hans Peter Büchler, and Sebastian Hofferberth. Observation of three-body correlations for photons coupled to a rydberg superatom. *Phys. Rev. Lett.*, 121:103601, Sep 2018.
- [105] Daniel Tiarks, Steffen Schmidt-Eberle, Thomas Stolz, Gerhard Rempe, and Stephan Dürr. A photon–photon quantum gate based on rydberg interactions. *Nature Physics*, 15(2):124, 2019.
- [106] A. Goban, C.-L. Hung, S.-P. Yu, J. D. Hood, J. A. Muniz, J. H. Lee, M. J. Martin, A. C. McClung, K. S. Choi, D. E. Chang, O. Painter, and H. J. Kimble. Atom–light interactions in photonic crystals. *Nat. Commun.*, 5:3808, 2014.

- [107] A. Javadi, I. Söllner, M. Arcari, S. Lindskov Hansen, L. Midolo, S. Mahmoodian, G. Kiršanskė, T. Pregonolato, E. H. Lee, J. D. Song, S. Stobbe, and P. Lodahl. Single-photon non-linear optics with a quantum dot in a waveguide. *Nat. Commun.*, 6:8655, 2015.
- [108] R. J. Coles, D. M. Price, J. E. Dixon, B. Royall, E. Clarke, P. Kok, M. S. Skolnick, A. M. Fox, and M. N. Makhonin. Chirality of nanophotonic waveguide with embedded quantum emitter for unidirectional spin transfer. *Nat. Commun.*, 7:11183, 2016.
- [109] Lea F Santos and E Jonathan Torres-Herrera. Nonequilibrium quantum dynamics of many-body systems. In *Chaotic, Fractional, and Complex Dynamics: New Insights and Perspectives*, pages 231–260. Springer, 2018.
- [110] R. Loudon. *The quantum theory of light*. Oxford University Press, 2000.
- [111] C Gerry and P Knight. *Introductory quantum optics*. 2005.
- [112] Prasad Adarsh Shankar. Complete temporal characterization of single photons. Master’s thesis, Institute for Quantum Science and Technology, University of Calgary, 2014.
- [113] Leonard Mandel. Sub-poissonian photon statistics in resonance fluorescence. *Optics Letters*, 4(7):205–207, 1979.
- [114] XT Zou and L Mandel. Photon-antibunching and sub-poissonian photon statistics. *Physical Review A*, 41(1):475, 1990.
- [115] Surendra Singh. Antibunching, sub-poissonian photon statistics and finite bandwidth effects in resonance fluorescence. *Optics Communications*, 44(4):254–258, 1983.
- [116] HJ Kimble and L Mandel. Theory of resonance fluorescence. *Physical Review A*, 13(6):2123, 1976.
- [117] HJ Kimble, M Dagenais, and L Mandel. Multiatom and transit-time effects on photon-correlation measurements in resonance fluorescence. *Physical Review A*, 18(1):201, 1978.
- [118] Z. Yuan, B. E. Kardyna, R. M. Stevenson, A. J. Shields, C. J. Lobo, K. Cooper, N. S. Beattie, D. A. Ritchie, and M. Pepper. Electrically driven single-photon source. *Science*, 295:102, 2002.
- [119] Frank Diedrich and Herbert Walther. Nonclassical radiation of a single stored ion. *Phys. Rev. Lett.*, 58:203–206, Jan 1987.
- [120] BL Morgan and L Mandel. Measurement of photon bunching in a thermal light beam. *Physical Review Letters*, 16(22):1012, 1966.
- [121] R Hanbury Brown, Richard Q Twiss, et al. Correlation between photons in two coherent beams of light. *Nature*, 177(4497):27–29, 1956.
- [122] Evan J Evans. The spectra of helium and hydrogen. *Nature*, 92(2288):5–5, 1913.

- [123] Paul Adrien Maurice Dirac. The fundamental equations of quantum mechanics. *Proceedings of the Royal Society of London. Series A, Containing Papers of a Mathematical and Physical Character*, 109(752):642–653, 1925.
- [124] B. R. Mollow. Power spectrum of light scattered by two-level systems. *Phys. Rev.*, 188:1969, 1969.
- [125] HJ Carmichael and DF Walls. Proposal for the measurement of the resonant stark effect by photon correlation techniques. *Journal of Physics B: Atomic and Molecular Physics*, 9(4):L43, 1976.
- [126] Julien Claudon, Joël Bleuse, Nitin Singh Malik, Maela Bazin, Périne Jaffrennou, Niels Gregersen, Christophe Sauvan, Philippe Lalanne, and Jean-Michel Gérard. A highly efficient single-photon source based on a quantum dot in a photonic nanowire. *Nature Photonics*, 4(3):174–177, 2010.
- [127] Jeremy L O’Brien, Akira Furusawa, and Jelena Vučković. Photonic quantum technologies. *Nature Photonics*, 3(12):687, 2009.
- [128] Dirk Englund, Brendan Shields, Kelley Rivoire, Fariba Hatami, Jelena Vuckovic, Hongkun Park, and Mikhail D Lukin. Deterministic coupling of a single nitrogen vacancy center to a photonic crystal cavity. *Nano letters*, 10(10):3922–3926, 2010.
- [129] Mohammad Mirhosseini, Eunjong Kim, Xueyue Zhang, Alp Sipahigil, Paul B. Dieterle, Andrew J. Keller, Ana Asenjo-Garcia, Darrick E. Chang, and Oskar Painter. Cavity quantum electrodynamics with atom-like mirrors. *Nature*, 569:692, 2019.
- [130] K. Srinivasan and O. Painter. Linear and nonlinear optical spectroscopy of a strongly coupled microdisk-quantum dot system. *Nature*, 450:862, 2007.
- [131] BR Mollow. Power spectrum of light scattered by two-level systems. *Physical Review*, 188(5), 1969.
- [132] J Dalibard and S Reynaud. Correlation signals in resonance fluorescence: interpretation via photon scattering amplitudes. *Journal de Physique*, 44(12):1337–1343, 1983.
- [133] J. T. Shen and Shanhui Fan. Coherent photon transport from spontaneous emission in one-dimensional waveguides. *Opt. Lett.*, 30:2001, 2005.
- [134] Jung-Tsung Shen, Shanhui Fan, et al. Theory of single-photon transport in a single-mode waveguide. i. coupling to a cavity containing a two-level atom. *Physical Review A*, 79(2):023837, 2009.
- [135] Jung-Tsung Shen and Shanhui Fan. Theory of single-photon transport in a single-mode waveguide. ii. coupling to a whispering-gallery resonator containing a two-level atom. *Phys. Rev. A*, 79:023838, Feb 2009.



- [136] Shanhui Fan, Şükrü Ekin Kocabaş, and Jung-Tsung Shen. Input-output formalism for few-photon transport in one-dimensional nanophotonic waveguides coupled to a qubit. *Physical Review A*, 82(6):063821, 2010.
- [137] Keyu Xia, Guowei Lu, Gongwei Lin, Yuqing Cheng, Yueping Niu, Shangqing Gong, Jason Twamley, et al. Reversible nonmagnetic single-photon isolation using unbalanced quantum coupling. *Physical Review A*, 90(4):043802, 2014.
- [138] Carlos Gonzalez-Ballester, Esteban Moreno, Francisco J Garcia-Vidal, and Alejandro Gonzalez-Tudela. Nonreciprocal few-photon routing schemes based on chiral waveguide-emitter couplings. *Physical Review A*, 94(6):063817, 2016.
- [139] Sahand Mahmoodian, Mantas Čepulkovskis, Sumanta Das, Peter Lodahl, Klemens Hammerer, and Anders S Sørensen. Chiral waveguide qed: Strongly correlated photon transport with weakly coupled emitters. *arXiv preprint arXiv:1803.02428*, 2018.
- [140] D Reitz, C Sayrin, B Albrecht, I Mazets, R Mitsch, P Schneeweiss, and A Rauschenbeutel. Backscattering properties of a waveguide-coupled array of atoms in the strongly nonparaxial regime. *Physical Review A*, 89(3):031804, 2014.
- [141] Mehran Kardar. *Statistical physics of fields*. Cambridge University Press, 2007.
- [142] Harold J. Metcalf and Peter van der Straten. *Laser Cooling and Trapping*. Springer New York, 1999.
- [143] Peter Young. Everything you wanted to know about data analysis and fitting but were afraid to ask. *arXiv preprint arXiv:1210.3781*, 2012.
- [144] William H Press, Saul A Teukolsky, William T Vetterling, and Brian P Flannery. *Numerical recipes 3rd edition: The art of scientific computing*. Cambridge university press, 2007.
- [145] Thomas Legero, Tatjana Wilk, Markus Hennrich, Gerhard Rempe, and Axel Kuhn. Quantum beat of two single photons. *Phys. Rev. Lett.*, 93:070503, Aug 2004.
- [146] Ole Aae Iversen and Thomas Pohl. Strongly correlated states of light in chiral chains of three-level quantum emitters. *arXiv preprint arXiv:2006.03408*, 2020.
- [147] Ryan Jones, Giuseppe Buonaiuto, Ben Lang, Igor Lesanovsky, and Beatriz Olmos. Collectively enhanced chiral photon emission from an atomic array near a nanofiber. *Phys. Rev. Lett.*, 124:093601, Mar 2020.
- [148] C. Sayrin, C. Clausen, B. Albrecht, P. Schneeweiss, and A. Rauschenbeutel. Storage of fiber-guided light in a nanofiber-trapped ensemble of cold atoms. *Optica*, 2(4):353–356, 2015.
- [149] A Asenjo-Garcia, M Moreno-Cardoner, A Albrecht, HJ Kimble, and DE Chang. Exponential improvement in photon storage fidelities using subradiance and “selective radiance” in atomic arrays. *Physical Review X*, 7(3):031024, 2017.

## BIBLIOGRAPHY

---

- [150] HL Sørensen, J-B Béguin, KW Kluge, I Iakoupov, AS Sørensen, JH Müller, ES Polzik, and J Appel. Coherent backscattering of light off one-dimensional atomic strings. *Physical Review Letters*, 117(13):133604, 2016.

# Acknowledgement

PhD was the toughest time of my life so far. Now that it has finally come to a conclusion, I would sincerely like to thank all the people who have helped me throughout this journey.

First and foremost, I would like to thank my supervisor for choosing me into his research group and for having the confidence in me as a physicist. His suggestions and ideas have always been very valuable. Another big thanks must go to Jürgen and Philipp who have been with me at every step of the journey, especially to help me with physics in and out of the lab and for having patience to read through my thesis and for generating ideas for the experiments. I ought to thank my lab partners, J. Hinney and S. Rind for helping me build the setup together. I would also like to thank Christoph, our postdoc in the starting few years, from who I learnt a lot of things, in particular, about lasers and electronics and programming. I would like to thank all the other group members as well for their awesome company. The group lunches and meetings will be missed ! I would also like to thank my collaborators - S. Mahmoodian, K. Hammerer, and A. Sørensen, for their initial idea on correlated photon transport through our system and their help in understanding the underlying theory and the experimental data better.

I would like to thank my friends at ATI who were always supportive and helped me at the difficult times during these years. I would also like to thank my PhD program - CoQuS, and the community therein, all the secretaries and administrative staff at ATI and in CoQuS, who helped me at several points during my PhD. Apart from work, I would like to thank my friends from my Argentine Tango group, who made my life interesting and enjoyable throughout these years. I would also like to thank my roommates and the neighbours from the adjacent WG at Leichtensteinstrasse, who were always fun to hang out with. I would like to end the acknowledgement by thanking the people who are closest to me. I would especially like to thank Elisa who has always been there for me throughout the PhD and beyond. And I would like to thank Papa, Shikha and Mummy, without who I would not have been at this position.



Die approbierte gedruckte Originalversion dieser Dissertation ist an der TU Wien Bibliothek verfügbar.  
The approved original version of this doctoral thesis is available in print at TU Wien Bibliothek.

# LEBENS LAUF

Adarsh Shankar Prasad  
Simon-Denk-Gasse 2/21  
1090 Wien  
Österreich

## Persönliche Daten

Geburtsdatum: 1. Mai 1988  
Geburtsort: Ranchi, Indien  
Staatsangehörigkeit: Indien

## Ausbildung

seit 09/2014	Technische Universität Wien, Doktorand in Technischer Physik
08/2012 – 08/2014	University of Calgary, Canada, Master of Science in Physics
08/2007 – 05/2011	Indian Institute of Technology Guwahati, India, Bachelor of Technology in Engineering Physics
2006	Higher secondary schooling (Grade 11-12), Ranchi, India
2004	Secondary school (Grade 1-10), Ranchi, India